OSCILLATORY COMPRESSIBLE FLOW AND HEAT TRANSFER IN POROUS MEDIA – APPLICATION TO CRYOCOOLER REGENERATORS

A Dissertation

Presented to

The Academic Faculty

by

Jeremy Paul Harvey

In Partial Fulfillment

of the Requirements for the Degree

Doctor of Philosophy in Mechanical Engineering

Georgia Institute of Technology

December 2003

OSCILLATORY COMPRESSIBLE FLOW AND HEAT TRANSFER IN POROUS MEDIA – APPLICATION TO CRYOCOOLER REGENERATORS

APPROVAL

Prateen V. Desai, Chairman, Mechanical Engineering

S. Mostafa Ghiaasiaan, Mechanical Engineering

Minami Yoda, Mechanical Engineering

Carl S. Kirkconnell, Raytheon Space and Airborne Systems

Jeffrey F. Morris, Chemical Engineering

Date Submitted: November 25, 2003

ACKNOWLEDGEMENTS

I have been blessed to have been involved in this research with so fine a group. And it is indeed the group of individuals whom have assisted me that have made this research so enjoyable and productive. Beginning with those most directly involved in the research, I would like to thank my committee. Dr. Prateen Desai, my thesis advisor, fortunately thought of me when Dr. Carl Kirkconnell was searching out an undergraduate student to perform this research for, at the time, Hughes Aircraft Company. The Woodruff School and the Georgia Tech community have been so fortunate to have Dr. Desai as a dedicated professor, and I as a friend and advisor. Dr. Mostafa Ghiaasiaan quickly took an interest in the research after conversing with me and he now will lead the cryocooler research at Georgia Tech. Drs. Minami Yoda and Jeffrey Morris completed my team of advisors by providing breadth of knowledge in their fields. Of these individuals, Dr. Kirkconnell deserves special thanks for being the catalyst for the research at Hughes Aircraft , and now Raytheon Space and Airborne Systems. I hope that I can provide the same enthusiasm and energy that you have provided me.

This research was performed due, in no small part, to the research grants provided by Hughes Aircraft Company and Raytheon Company to the Georgia Tech Foundation. Additional thanks must go to the Hughes and Raytheon Doctoral Fellowship Program and the Georgia Institute of Technology Presidential Scholarship for supporting me directly throughout this program.

At Raytheon, special thanks to Mr. Alberto Schroth, Mr. Kenneth Price, Mr. Thomas Pollack, Mr. William Croft, and Mr. David Mc Gorrin. At Georgia Tech, I have

been so fortunate to have several undergraduate and graduate students work with me in my lab; Mr. Matthieu Coutaudier, Mr. Robert Hon, and Mr. Jeesung “Jeff” Cha, the next torch bearer.

I thank my whole family for their support and love, especially my parents who are so far away, but so near my heart, my sister Janelle, who I am so thankful is close, and to my wife’s family who I wish were close. My wife Chrystine has been my rock during this undertaking. She has given me so much hope and now our new life begins.

TABLE OF CONTENTS

Approval ii

Acknowledgements iii

List of Figures x

List of Tables xiv

List of Tables xiv

Nomenclature xv

Summary xx

1. Introduction and Background 1

1.1 Introduction 1

1.2 Background 4

1.2.1 History of Pulse Tube Cryocoolers 4

1.2.2 Survey of Efforts to Improve the Regenerator 7

1.2.3 Development of the Volume Averaging Technique 15

1.2.4 Overview 16

2. Theoretical Development 19

2.1 Governing Equations and Constitutive Relations 19

2.1.1 Conservation of Mass Equation 20

2.1.2 Balance of Momentum Equations 20

2.1.3 α-Phase Conservation of Energy Equation 21

2.1.4 β-Phase Conservation of Energy Equation 22

2.1.5 Equations of State 22

2.1.6 α-Phase Entropy Generation Equation 23

2.1.7 β-Phase Entropy Generation Equation 23

2.1.8 Summary of Equations 24

2.2 Volume-Averaged Equations 25

2.2.1 Volume-Averaged Conservation of Mass Equation 25

2.2.2 Volume-Averaged Balance of Momentum Equation 26

2.2.3 Volume-Averaged α-Phase Conservation of Energy Equation 26

2.2.4 Volume-Averaged β-Phase Conservation of Energy Equation 27

2.2.5 Volume-Averaged α-Phase Entropy Generation Equation 28

2.2.6 Volume-Averaged β-Phase Entropy Generation Equation 28

2.3 Simplifying Assumptions 29

2.3.1 Density Spatial Deviation 29

2.3.2 Negligible Mechanical Dispersion 31

2.3.3 Thermal Dispersion 32

2.3.4 Entropy Generation Due to Thermal Dispersion 33

2.3.5 Negligible Brinkman Effect 34

2.3.6 One Dimensional Model on the Macroscopic Length Scale 34

2.4 Simplified Equations 35

2.4.1 Simplified Conservation of Mass Equation 35

2.4.2 Simplified Balance of Momentum Equation 36

2.4.3 Simplified α-Phase Conservation of Energy Equation 37

2.4.4 Simplified β-Phase Conservation of Energy Equation 37
2.4.5 Simplified α-Phase Entropy Generation Equation 39
2.4.6 Simplified β-Phase Entropy Generation Equation 39
2.4.7 Summary of Equations 44
2.5 Exact Solutions 46
2.6 Scale Analysis 49
2.6.1 Conservation of Mass Equation Scale Analysis 50
2.6.2 Balance of Momentum Equation Scale Analysis 50
2.6.3 α-Phase Conservation of Energy Equation Scale Analysis 52
2.6.4 β-Phase Conservation of Energy Equation Scale Analysis 54
2.6.5 Scaled Equation Summary 55
2.6.6 Limiting Cases 59
3. Computational Models 60
3.1 Problem Definition 60
3.2 Numerical Method 61
3.2.1 Time Integration 62
3.2.2 Spatial Discretization 62
3.3 Quasi-Steady Convergence via Cyclic Time Relaxation 63
3.4 Boundary and Initial Conditions 66
3.5 The Constant Temperature Model (CTM) 70
3.6 The Local Thermal Equilibrium Model (LTEM) 72
3.7 Dual Energy Equation Model (DEEM) 74

3.8 Model Verification 75
4. Experimental apparatus and measurements 84
4.1 Overview and Experimental Apparatus 84
4.2 Experimental Results 94
5. Results and Discussion 105
5.1 Sage System Level Modeling 106
5.2 Model Comparison 110
5.2.1 Net Enthalpy Flowrate - The Perfect Regenerator 110
5.2.2 The Mean Temperature Profile 113
5.2.3 Baseline Regenerator Solutions 114
5.2.4 First Law Results 118
5.2.5 Second Law Results 120
5.2.6 Sage and REGEN Comparisons 122
5.2.7 Permeability and Forchheimer Coefficient Predictions 125
6. Conclusions and Recommendations 129
6.1 Conclusions 129
6.2 Contributions 131
6.3 Future Work 132
Appendix 1 – Derivation of the Volume-Averaged Governing Equations 136
A1.1 Volume Averaging Theory 136
A1.1.1 Definitions 136
A1.1.2 Transport Theorem 138

A1.1.3 Spatial Averaging Theorem 138
A1.1.4 Modified Averaging Theorem.....139
A1.2 Application to the Governing Equations 140
A1.2.1 Volume-Averaged Conservation of Mass Equation.....140
A1.2.2 Volume-Averaged Balance of Momentum Equation.....142
A1.2.3 Volume-Averaged α-Phase Conservation of Energy Equation 145
A1.2.4 Volume-Averaged β-Phase Conservation of Energy Equation.....146
A1.2.5 Volume-Averaged α-Phase Entropy Generation Equation.....147
A1.2.6 Volume-Averaged β-Phase Entropy Generation Equation 148
Appendix 2 – Derivation of Differentiation Operators Using MatLab.....149
Appendix 3 – Compressor Electro-Mechanical Modeling 154
A3.1 The electromechanical system.....154
A3.2 The Mechanical System.....155
A3.3 The Electrical System.....158
Bibliography 162

LIST OF FIGURES

Figure 1 - Comparison Diagram of the PTC and Stirling Cryocooler 1

Figure 2 – A) Basic Pulse Tube Cryocooler and B) Orificed Pulse Tube Cryocooler 5

Figure 3 - Bypass Pulse Tube Cryocooler 6

Figure 4 - Thermohydraulic system of a typical porous media. The α-phase is a Newtonian fluid and the β-phase is a solid. 19

Figure 5 – Conceptual diagram illustrating the local velocity, velocity deviation, and the volume-averaged velocity. 30

Figure 6 – Regenerator computational domain diagram 60

Figure 7 – Test case solution results. 78

Figure 8 – The net enthalpy flux satisfies the test case to within visual accuracy (0.2 mW deviation) 79

Figure 9 – Maximum density error 8×10^{-6} kg/m^3 80

Figure 10 – Maximum mass flux error 1×10^{-5} kg/m^2-s 80

Figure 11 – Maximum energy error 2 kJ/m^3 81

Figure 12 – Maximum matrix temperature error 6×10^{-6} K 81

Figure 13 – Maximum gas temperature error 8×10^{-6} K 82

Figure 14 – Maximum pressure error 1.2 Pa 82

Figure 15 - Experimental Apparatus 85

Figure 16 – Regenerator/Pulse Tube expander module. Regenerator is the larger diameter section. 85
Figure 17 – Experimental apparatus with complete instrumentation. 86
Figure 18 – Close-up view of the compressor. 86
Figure 19 – Turbo vacuum pump station. 87
Figure 20 - Wire Mesh 90
Figure 21 - Perforated Disk 90
Figure 22 - Foam Metal 90
Figure 23 – Data acquisition system. 91
Figure 24 - Data acquisition and control program. Main panel view. 92
Figure 25 - Data acquisition and control program. Compressor panel view. 92
Figure 26 - Data acquisition and control program. Pressure panel view. 93
Figure 27 - Steady Flow Pressure Drop 95
Figure 28 - Load Curves 97
Figure 29 - Oscillatory Pressure Drop 99
Figure 30 - Pressure Wave Phase Angle 100
Figure 31 - Pressure Ratio Attenuation 101
Figure 32 – Sintered glass regenerator 104
Figure 33 – Sage diagram of the laboratory pulse tube apparatus. 107
Figure 34 - System level energy flow diagram; 400 mesh, 76 K, 0 W 108

Figure 35 – Comparison of regenerator loss calculated with limiting case models based on identical operating conditions (ideal gas assumes constant properties.) 112
Figure 36 – Comparison of mean temperature profiles calculated with the different models based on identical operating conditions. 114
Figure 37 – Solutions plotted versus time and position. The middle plots are max and min of density and velocity. Pressure and mass flow phase shifts are apparent. 115
Figure 38 – Boundary solutions for the gas and matrix temperatures and enthalpy flow rates. 116
Figure 39 – Cycle-averaged gas temperature (red) versus a linear profile (blue). 117
Figure 40 – Temperature difference versus position (multiple lines) and time. 118
Figure 41 – Mean Reynolds Number 118
Figure 42 – Cycle-averaged mass flow rate. 119
Figure 43 – Cycle-averaged energy flows. Regenerator total energy flow is constant along regenerator. 119
Figure 44 – Entropy generation due to viscous and inertial losses (top), and entropy generation due to conduction and dispersion in the gas (bottom). Multiple curves represent different locations in the regenerator, plotted versus cycle time. Results for 400 mesh baseline case. 120

Figure 45 – Entropy generation due to matrix conduction (top), and entropy generation due to interfacial convection (bottom). Results for 400 mesh baseline case. 121
Figure 46 – Cycle-averaged volumetric entropy generation rates plotted versus position in the regenerator. Results for 400 mesh baseline case. 121
Figure 47 – Comparison of Sage-predicted regenerator loss versus GT model. 123
Figure 48 – Friction factor comparison for 400 mesh screens....128
Figure 49 - Demonstration calculation for flow through wire mesh screens. Visualization of surface pressure....133
Figure 50 – Demonstration calculation for flow through wire mesh screens. Visualization of pathlines. 133
Figure 51 – Voice coil compressor schematic 155
Figure 52 – Compressor piston free-body diagram (FBD)....156
Figure 53 – Leach's lossy inductor voice coil model 158

LIST OF TABLES

Table 1-Summary of scale analysis 58

Table 2 - Descriptive Summary of the Regenerators under Study 88

Table 3 – Porous Media Parameter Summary (64).....96

Table 4 – 400 mesh baseline operating conditions 109

Table 5 – Sage Comparison Summary.....124

Table 6 – Permeability and Forchheimer Coefficient (compressible model).....126

Table 7 – Permeability and Forchheimer Coefficient (incompressible model).....126

Table 8 – Permeability and Forchheimer Coefficient (neglecting advective acceleration).....126

NOMENCLATURE

Notation:

α	Gas Phase
β	Solid Phase
$\langle a_\alpha \rangle$	Volume average of quantity a in the α phase
$\langle a_\alpha \rangle^\alpha$	Intrinsic volume average of quantity a in the α phase
$\hat{a}$	Spatial deviation of quantity a
$\vec{v}$	Vector of v

Variables:

$A_{\alpha\beta}$	Area of the $\alpha - \beta$ interface (within the averaging-volume, V) [m^2]
A_f	Flow area [m^2]
A	Total cross sectional area, gas and solid [m^2]
a_v	Surface area per unit volume [1/m]
$\tilde{b}_\alpha$	Thermal dispersion tensor closure variable
C_1, C_2	Integration constants
c_p	Gas constant pressure specific heat [J/kg-K]
c_v	Gas constant volume specific heat [J/kg-K]
c_{ps}, c_{vs}	Specific heat scales [J/kg-K]

c_f	Forchheimer inertia coefficient
$\widetilde{D}_\alpha$	Thermal dispersion tensor
$\widetilde{D}_2$	Mechanical dispersion tensor, rank 2
D_r	Regenerator diameter [m]
dS	Differential surface area of $A_{\alpha\beta}$ [m^2]
E	Gas total energy per unit volume [J/m^3]
$\widetilde{E}$	Gas total energy temporal scale [J/m^3]
$\widetilde{E}_3$	Mechanical dispersion tensor, rank 3
e_α, e	Specific internal energy [J/kg]
$\widetilde{F}$	Forchheimer tensor
F	Darcy-Forchheimer surface integral
F_1, F_2, F_3, F_4	Source terms for exact solution
f	Friction factor, frequency [Hz]
$\widetilde{G}_4$	Mechanical dispersion tensor, rank 4
H	Convective heat transfer coefficient [W/m^2-K]
h	Enthalpy [J/kg]
$\overline{h}$	Enthalpy spatial scale [J/kg]
$\widetilde{I}$	Identity tensor
$\widetilde{K}$	Permeability tensor [m^2]
K	Permeability, in axial direction [m^2]

k_α, k_β	Conductivity [W/m-K]
L_r	Regenerator length [m]
L_s	Macroscopic length scale [m]
m_α, m	Mass flux [kg/m^2-s]
$\overline{m}, \widetilde{m}$	Mass flux spatial and temporal scales [kg/m^2-s]
m_h, m_c	Hot and cold boundary mass flux amplitudes [kg/m^2-s]
$\dot{m}_h, \dot{m}_c$	Hot and cold boundary mass flow rates [kg/s]
N_k	Axial conductivity enhancement
Nu	Nusselt number
n_α, n_β	Normal vector
Pe	Reference Peclet number
p_α, p	Gas pressure [Pa]
$\overline{p}$	Pressure spatial scale [Pa]
p_b	System baseline pressure [Pa]
q_g, q_m	Gas and matrix heat flux [W/m^2]
R	Gas constant, or radius of averaging volume [Pa-m^3/kg-K]
Re_K	Reynolds number based on permeability length scale
St	Reference Stanton number
$s'''_{gen,\alpha}, s'''_{gen,\beta}$	Volumetric entropy generation [W/m^3-K]
s_α, s_β	Entropy [J/kg-K]

T_α, T_β	Temperature [K]
$\overline{T}$	Temperature spatial scale [K]
$\hat{T}$	Temperature difference scale [K]
T_h, T_c	Hot and cold boundary mean temperatures [K]
T_o	Reference temperature, for lost power [K]
t	Time [s]
t_s	Time scale [s]
$\vec{u}_\alpha$	Velocity vector [m/s]
u_α, u	Axial velocity [m/s]
V_α, V_β, V	Volume (of the averaging-volume) [m^3]
$\dot{W}_{lost}$	Lost power [W]
x	Axial location [m]

Greek:

ρ_α, ρ	Density [kg/m^3]
$\overline{\rho}, \widetilde{\rho}$	Density spatial and temporal scales [kg/m^3]
$(\rho c)_\beta$	Solid heat capacity [J/K]
ϕ_{mh}, ϕ_{mc}	Hot and cold boundary mass flux phase angles [rad]
ϕ_α	Viscous dissipation function
μ_α, μ	Gas viscosity [m-s]

$\varepsilon_\alpha, \varepsilon_\beta, \varepsilon$	Porosity
ω	Angular frequency [rad/s]
τ	Time period [s]
τ_β	Solid tortuosity
Γ_1, Γ_2	Leading order dimensionless parameters
$\varepsilon_1, \varepsilon_2$	Leading order dimensionless parameters
γ	Specific heat ratio

SUMMARY

In this study the phenomena of compressible flow and heat transfer in porous media are modeled based on fundamental principles. The conservation equations for the two phases are transformed by the method of volume averaging which is an analytical method used to unite the microscale and macroscale effects characteristic to porous media flows. Unique to this analysis is the fact that the model is valid for oscillatory, cryogenic flows such as that occurring in a regenerative cryogenic refrigerator such as a Pulse Tube Cryocooler (PTC.)

In a PTC the forced flow driven oscillations in the regenerator create Reynolds numbers high enough such that microscale inertial effects dominate the momentum equation. This phenomenon, known as the Forchheimer Effect, can be predicted and modeled based solely on fundamental principles and the method of volume averaging. The coefficients that characterize the Forchheimer momentum equation are determined experimentally.

Heat transfer within a porous medium occurs due to temperature gradients in the gas and solid phases. Conduction within the solid and fluid phases is made evident by volume averaging, but the determination of the conductivity coefficients requires numerical experiments and is unique to the geometry and conductivities of the two phases. Convection between the two phases is the dominant mode of heat transfer within the porous media. Determination of the convective heat transfer coefficient for a porous media requires physical experiments.

Heat transfer due to temperature gradients and flow friction in the regenerator are always competing effects leading to a model which requires coupling of the momentum and energy equations. These competing effects are united with the concept of entropy generation which relies on the second law of thermodynamics. All real processes generate entropy, and the most efficient processes which balance flow friction and heat transfer generate minimum entropy.

The theoretical model is presented with a numerical solution technique. These numerical solutions are compared with similar solutions existing in the literature. The uniqueness of this model is the completeness of the theoretical development and the flexibility of use for a variety of applications. Numerical solutions are compared with experimental data for an operating cryocooler.

CHAPTER 1

1. INTRODUCTION AND BACKGROUND

1.1 Introduction

Cryocoolers (refrigerators capable of cooling to temperatures below 120 K) have long been classified into two categories based on the type of heat exchange process: recuperative and regenerative (1). The Pulse Tube Cryocooler (PTC) and the Stirling Cryocooler are two examples of regenerative cryocoolers (Figure 1), both operating on a

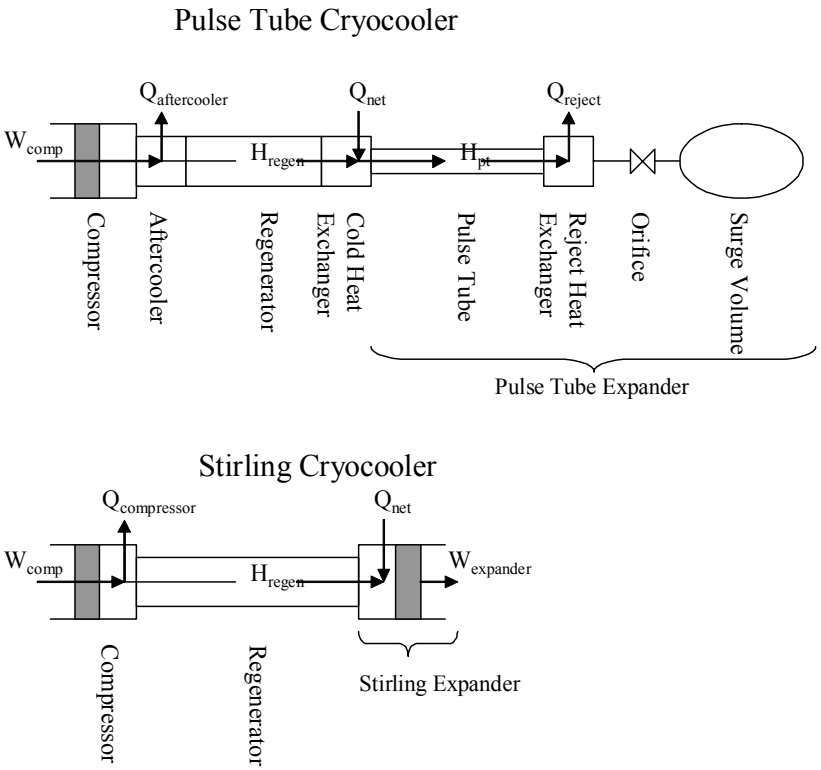

Figure 1 - Comparison Diagram of the PTC and Stirling Cryocooler

modified Stirling thermodynamic cycle using helium as the working substance. Unlike the Stirling thermodynamic cycle, the PTC and Stirling cryocooler cycles are not steady flow processes. Instead, the gas flow oscillates in a quasi-steady fashion due to the motion of a compressor piston (and an additional expander piston in the Stirling cryocooler).

In the Stirling cooler, refrigeration is produced by driving the expander piston such that it receives mechanical work from the working fluid. If this work is sufficiently large, the heat exchanger can absorb heat from the surrounding, thus producing refrigeration. In the case of the PTC, the active expander piston is replaced with a passive pulse tube, orifice, and surge volume. The pulse tube gas motion can be controlled such that there is a gas "piston" which acts like the Stirling piston. If the motion of the gas piston has the proper phase, it accepts work from the cold heat exchanger and delivers this work to the reject heat exchanger where it is converted into heat. This heat is rejected from the system in the reject heat exchanger.

The PTC is a unique type of regenerative cryocooler in that it does not have any moving parts in the cold region. This is distinctly different from the Stirling cryocooler that operates by an oscillating displacer directly in the cold region, resulting in the potential for mechanical wear that increases mechanical complexity and can limit the life of the cooler. Vibration in the Stirling cooler caused by the displacer also presents problems for applications like sensitive infrared sensors, which cannot tolerate vibration. Due to the absence of an expander piston in the cold region and the additional volume

after the regenerator, the pulse tube experiences much higher mass flow rates through the regenerator. This results in a larger regenerator pressure drop.

The regenerator is a duct packed with some porous material. This porous material is selected such that it has sufficient thermal heat capacity, high heat transfer coefficient, and low flow friction. The designer of a cryocooler is chiefly concerned with achieving a specified net refrigeration at a given temperature with a minimum input power. In the design of a pulse tube cooler, the net refrigeration is the heat transfer rate from the cryogenic device being cooled, which is equal to the total gross refrigeration produced less internal parasitic losses in the cooler. Minimizing parasitic heat loads is critical to achieving the design goals. One main system loss is the regenerator loss, or the cycle-averaged enthalpy flow at the cold end plus conduction losses in the gas and matrix. These losses can be considerable, and may be quantified only via an accurate mathematical model. The enthalpy loss is the most difficult quantity to estimate, requiring an accurate prediction of the mass flow and temperature waveforms at the cold end. It is not unrealistic to have an enthalpy loss on the order of one Watt with a peak enthalpy flow rate of 1000 Watts, or 0.1%.

Regenerative cryocoolers are used in a variety of applications. The types of regenerators being studied in this work are typically found in Stirling and pulse tube cryocoolers, and other types of regenerative cryocooler applications. These devices are typically used in applications which demand small net refrigeration (on the order of a few watts) at temperatures below 100 K. Applications which require this type of refrigeration are superconducting electronics, magnetic resonance imaging, and infrared focal plane

arrays. Several other applications include gas liquefaction of nitrogen, magnetocardiography using Superconducting Quantum Interference Devices (SQUIDs), mine-sweeping magnets, nondestructive evaluation using SQUIDs, outer space experiments and instruments, and military weapon systems.

1.2 Background

The experimental apparatus used in this research is a Pulse Tube Cryocooler. For this reason, it is necessary to provide a brief history of the PTC including efforts to improve the performance of the PTC. The component being studied in the PTC is the regenerator. A review of the efforts to improve regenerator performance includes studies of materials and geometry. To understand the regenerator, investigators have used experimental measurements and numerical modeling. The following discussion is a review of these efforts.

1.2.1 History of Pulse Tube Cryocoolers

In 1966, Gifford and Longsworth first detailed the construction of a pulse tube refrigerator (2, 3). The design of their pulse tube was essentially a tube with one end closed and the other end open (in addition to a compressor and heat exchangers.) Both ends had heat exchangers, and the open end was subjected to an oscillating pressure through a regenerator, causing the open end to cool. This refrigerator is commonly known as the Basic Pulse Tube Cryocooler (BPTC) (Figure 2.A). Not until 1984 was the modern pulse tube cryocooler developed by Mikulin, Tarasov, and Shkrebyonock (4).

This cryocooler was equipped with an orifice and a surge volume on the warm end of the pulse tube. The effect of this enhancement was to create an advantageous phase difference between the oscillating pressure and velocity. This new design is commonly called the Orifice Pulse Tube Cryocooler (OPTC) (Figure 2.B). Other enhancements have been made such as porting the high-pressure gas from the outlet of the compressor to the warm end of the pulse tube which led to improved performance due to improved phase control. This type of cryocooler is called a Bypass Pulse Tube Cryocooler (Figure 3). The drawback of this design is that the flow bypass can create a DC flow circulation if the system is not designed properly. A very small flow circulation can lead to a huge reduction in performance.

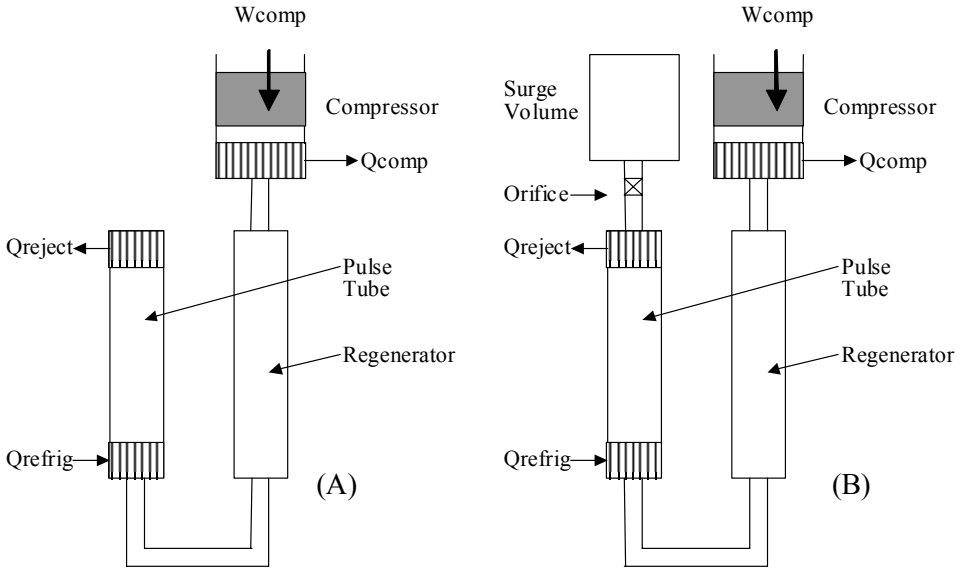

Figure 2 – A) Basic Pulse Tube Cryocooler and B) Orificed Pulse Tube Cryocooler

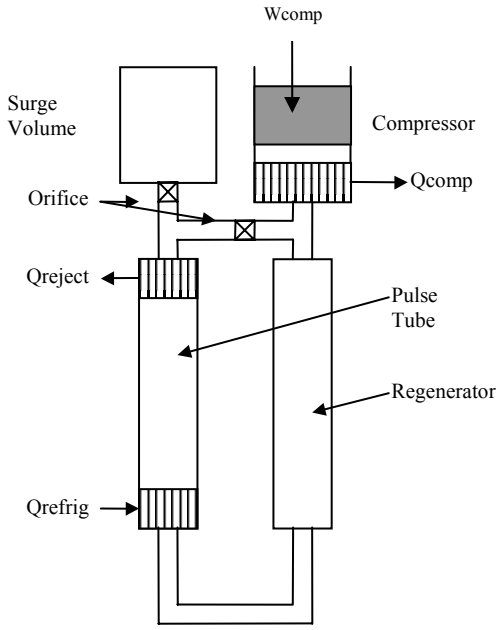

Figure 3 - Bypass Pulse Tube Cryocooler

Developments in pulse tube technology have been occurring continuously up to the present. Currently, three main areas of improvement are minimization of pulse tube flow losses, phase control, and improving regenerator effectiveness. Reducing pulse tube flow losses begins by being able to completely model the oscillating flow in the pulse tube. The flow oscillations result in mass streaming and radial heat transfer, both of which reduce the refrigeration possible with a pulse tube. Recently, several investigators discovered that a proper tapering of the pulse tube leads to a complete elimination of mass streaming (5).

As already mentioned in the preceding, the basic, orifice, and bypass pulse tube all seek to manipulate the phase angle between the pressure and mass flow to an optimum angle at which the maximum refrigeration is produced. One recent improvement is the

inertance tube (6). The inertance tube improves the orifice design by adding an inertance to the fluidic system. This improvement not only increases the phase angle, but also eliminates the possibility of flow circulations which can occur with the bypass design. Design of an optimum phase control device and reducing pulse tube losses will eventually make the pulse tube cryocooler more competitive than the Stirling cryocooler for most applications due to significantly lower cost and comparable efficiency.

1.2.2 Survey of Efforts to Improve the Regenerator

Extensive efforts have been focused on improvement in regenerator technology since the development of regenerative cryocoolers. These efforts have been categorized into areas of materials and geometry, modeling, and measurement.

The problems with designing the optimum regenerator have interesting complications as the temperature of the cold end decreases. These complications arise in factors such as variation of thermal properties over the huge temperature range of the regenerator. Orders of magnitude decrease in thermal capacity of the material from 300 K to the cold temperature make different materials attractive in different areas of the regenerator. The basic problem focuses on increasing the heat transfer effectiveness between the gas and solid in the regenerator. The heat transfer effectiveness is a function of fluid properties, solid properties, and the flow geometry. Any change in these parameters will affect the regenerator performance.

At temperatures below 20 K, the solid properties appear to be a major contributor to the overall regenerator performance. This has led to a development of exotic materials

and processes so that the regenerator has sufficient thermal capacity in the cold region. Several erbium alloys have been tested, but these magnetic alloys are brittle at cryogenic temperatures. Pecharsky, et al. at Ames Laboratory have investigated titanium alloying of a popular erbium alloy, Er_3Ni (7). This alloy has been investigated by many as a regenerator material for Gifford-McMahon (G-M) and Stirling coolers operating below 10 K. The significant result was that this particular alloying increased the ductility without significantly decreasing the specific heat of the alloy. Gshneidner, et al. also at Ames Laboratory have suggested Er_6Ni_2Sn alloy for the first stage of a G-M cooler (8). Their main effort was to develop a process to generate this alloy. The results showed that practical issues such as particle escape from the regenerator and settling will prevent this alloy from being used in the near future. Again, the brittle properties of this alloy have limited its use. Bradshaw, et al. have performed experiments using a variety of different materials in several combinations to study their effects in a two stage Stirling cooler operating in the 15 K range (9). The materials used were gold wire, lead wire, Er_3Ni and stainless steel mesh. At the lowest operating temperatures, they found that the lead and Er_3Ni performed the best, and these materials were also found to have the highest specific heat at that temperature. Takashi, et al. have used a slightly different erbium alloy ($ErNi_{0.9}Co_{0.1}$) along with Er_3Ni in a large 2.2 W cooling capacity, 4.2 K G-M cooler with 12 kW compressor input (10). Their conclusion was that the combination of $ErNi_{0.9}Co_{0.1}$ and Er_3Ni increased the cooling capacity by a factor of 1.2 from a regenerator with just Er_3Ni. The $ErNi_{0.9}Co_{0.1}$ has a dramatic increase in specific heat around 6 K of approximately 1 J/K-cm^3 in contrast to 0.4 J/K-cm^3 for Er_3Ni. Chafe, et al. have replaced

lead balls with Neodymium plates and balls in the second stage of a 10 K G-M cooler application to utilize the higher heat capacity at the low temperatures (11). They have also taken advantage of a perforated plate geometry that reduces pressure drop in comparison to spheres. As a result, they were able to progress from 8 K down to 4 K under similar operating conditions.

The geometry of the pores in the regenerator matrix determine the pressure drop within the regenerator. Since pressure drop and heat transfer are coupled, a certain amount of pressure drop is required to achieve effective regeneration. Efforts to minimize the pressure drop while still having adequate heat transfer have been reported in the literature. Measurements of steady pressure drop and correlating these measurements to friction factors have been investigated by many. However, many investigators put too much confidence in the importance of steady flow friction factors (12, 13, 14). The correlations given by Kays and London, for example, do not correlate well for oscillatory flow pressure drop and heat transfer due to additional effects such as enhanced dispersion due to the oscillations (15). Organ in *Thermodynamics and Gas Dynamics of the Stirling Cycle Machine* states this argument repeatedly (16).

> There is something less than satisfactory about the way in which Stirling machine analysis handles flow within the regenerator:
> (1) The flow case is treated by the method traditional for steady, two-dimensional (or axi-symmetric), incompressible viscous flow in pipes, i.e., in terms of a friction factor, C_f, correlated with geometry and Reynolds number, N_{re}. When analysis and computer simulation based on such correlations yield pressure distributions which do not tally with measurement from running machines, it is common practice to 'improve' matters by arbitrarily adjusting the correlations. The technique is part of a process which has become known as 'validation'. Exercises in validation have been reported[1-3] which called for C_f at given Nre to be multiplied by factors between 4 and 7.

(2) The discrepancy between experimental measurement and theoretical prediction has come to be attributed to the fact that steady-flow correlations do not take into account the unsteady effects which arise from the cyclic nature of the flow processes in the Stirling machine. An enquiry into the role of unsteadiness is certainly called for. At the same time, usage and interpretation of the steady-flow correlations has been parochial, having in most instances looked no further than the incompressible-flow cases documented by Kays and London.[4]

Some investigators have made the realization that steady flow friction factor correlations are not adequate, but there is still a gap between their measurements and the physical phenomena occurring within the regenerator (16, 17, 18, 19, 20, 21). Organ makes a clear argument that the 'steady' flow through the porous media is not a true description due to inherent oscillatory fluctuations at the natural frequency of the pore structure. This indicates that there are local accelerations within the fluid even for unidirectional, 'steady' flow. This type of argument shows that there are effects other than the inertial, $\frac{1}{2}\rho u^2$, effect which is the conventional basis for correlating friction factor with Reynolds number. Organ claims that the pressure drop is a result of independent viscous, inertial, and compressibility effects. In a separate reference, Organ develops the concept of the regenerator flow impedance, which is based on a linear wave model (22). This concept provides a method to better explain the physical phenomena in the regenerator. The research being conducted by Roberts and Desai (23) are motivated by the concerns voiced by Organ.

It will be seen in later Chapters that steady flow measurements can be used effectively to predict friction factors which are accurate for steady flow and oscillating flow. The compressible nature of the gas flowing through the regenerator matrix leads to a non-constant pressure gradient. This requires that experimental data be used as

boundary conditions for a differential model rather than a lumped model which is typically used.

Theoretical modeling of the regenerator and general porous media flows have been conducted by many, and can be found under a variety of headings. Watson used an exact solution for incompressible flow in a tube to show how diffusion can be enhanced (24). While Watson was not interested in the regenerator problem, his research illustrates the basic phenomenon which occurs in the regenerator and the pulse tube. For zero net flow, the flow oscillations produce a positive net energy transport from the cold end to the warm end of a channel. Two authors have made direct extensions of Watson's initial investigation. Siegel's analysis applied this directly to the problem of the regenerator (25, 26). Although the flow in the regenerator is not incompressible, the results are interesting since he has focused explicitly on porous media flows. Siegel attributes the axial transport to the transverse conduction which occurs between adjacent fluid layers. Kaviany has investigated the effect of oscillatory flows on heat exchangers composed of tube bundles (27, 28). In this analysis, Kaviany considers the case of enhanced heat diffusion between two reservoirs due to the oscillations. His analysis is an important extension of Watson's work since he considers the coupled problem of the gas and the wall energy. While Watson assumes zero wall heat flux, Kaviany solves for the wall temperature directly. The solutions obtained are exact solutions for the velocity and temperatures. Zhang, et al. have applied the method of characteristics to solve the 1-D pulse tube governing equations (29). Preliminary results indicate that their method over-predicts the performance based on experimental results.

The concept of a complex Nusselt number is developed by Kornhauser and Smith (30). In this study, the instantaneous heat flux in a compression cylinder is observed to be out of phase with the bulk temperature difference. This indicates that the traditional Newton's law of cooling does not hold for oscillating flow above a critical oscillation frequency, which is used to define an oscillating Peclet number. They find that a complex formulation of Newton's law of cooling is applicable. This requires measurement of the real and imaginary component of the Nusselt number. These studies were conducted in a compression cylinder, but the authors allude to the fact that this can be extended to the compression and flow process occurring in the regenerator. The critical oscillation frequency increases proportional to the inverse of the square of the hydraulic diameter. The hydraulic diameter of the regenerator can be 5 to 6 orders of magnitude below that of the compression space used. Thus, it is expected that the imaginary component of the regenerator Nusselt number would be quite small for typical frequencies used in Stirling and PTC cooler.

Bauwens has proposed a 2-D model for the pulse tube and regenerator that can be approximated only for small fluctuations using perturbation methods (31). While the approximate solution that he obtains is interesting, the model could yields invalid results for a pulse tube cooler due to relatively large pressure oscillations. At large pressure ratios, the linearity assumption is no longer valid, requiring a fully nonlinear model. The fully nonlinear model ultimately requires a numerical approximation rather than the analytical solution which he obtains.

Roach, et al. also propose a perturbation solution to the regenerator problem (32). Their results indicate that the velocity and pressure fluctuations do not depend on the thermal interaction between the gas and solid. Conversely, the thermal interaction does depend on the velocity and pressure fluctuation. This allows solving for the velocity and pressure and then using those solutions to solve for the temperature. It does not appear that they have provided any experimental comparison. This model has been described in a separate publication by Kashani and Roach (33). The method has been incorporated into a program called ARCOPTR.

A finite difference program called REGEN3.2 (34) has been developed by the National Institute of Standards and Technology, and has been used to study the effects of regenerator geometry by Kuriyama, et al. (35). This model assumes that the pressure in the regenerator is uniform and oscillates in time. The effect of the pressure gradient is included as a correction. The mathematical model proposed by REGEN involves solving a system of equations for the density, velocity, gas temperature, and matrix temperature. The velocity field is found using an explicit equation derived from the continuity equation assuming zero pressure gradient. As a result, the velocity and density are essentially determined from a single equation. This leads to a non-conservative model. While the negligible pressure gradient assumption may be accurate for some cases such as Stirling regenerators, the higher flow rates found in pulse tube regenerators lead to inaccuracies in the REGEN model. The pressure phase shift across an optimally designed Stirling regenerator is typically small compared to a pulse tube regenerator. This leads to a smaller pressure gradient in the Stirling regenerator.

Currently, the most comprehensive model for cryocooler systems is Sage (36). This model provides the user the ability to model the entire cryocooler and carry out optimization studies. Although this model appears complete, Harvey, et al. were concerned with the accuracy of assumptions and numerical methods in Sage (37). Apparently, the pulse tube correlations lack accuracy for small pulse tube. Additionally, the numerical scheme employed by Sage involves approximating the solutions using Fourier series. The solution is found such that the equations are satisfied at as few as 6 time nodes in the cycle. If the actual solution cannot be accurately described using 6 time nodes, then the Sage model will be limited in accuracy. Further inaccuracies can be attributed to a non conservative spatial discretization method based on first order control volumes. While this model may have some inaccuracies, it has been found to be a valuable tool for the cryocooler designer because of the built-in optimization tool.

Measurements within the regenerator matrix are inherently difficult due to the small geometry of the pores. High frequency response sensors must be used to accurately resolve the oscillating temperatures and velocities. Several individuals have made some interesting and important measurements on the regenerator and pulse tube. Yuan and Dybbs have developed a method to measure both the gas and solid temperature fluctuations in the regenerator of a Stirling engine (38). This method utilizes small thermocouples whose responses are compensated to correct for attenuation and lag. Their results are well matched to numerical predictions. Rawlins, et al. have used hot-wire anemometer probes in key locations in a pulse tube cooler (39, 40). Oscillatory velocities and temperatures have been measured at both the warm and cold ends of the

pulse tube and regenerator. These measurements allowed them to calculate from pressure, temperature, and mass flow rates, the instantaneous energy and entropy flows in the pulse tube. The efforts to make these measurements are remarkable since the conditions, especially in the cold region, are certainly not hospitable to making hot-wire measurements. In fact, these measurements are some of the most sophisticated measurements made with hot-wires. Typical measurements in wind tunnels have only small temperature fluctuations about the ambient. These measurements were performed at temperatures below 90 K with fluctuations of 5 K. Installing the probes in a high pressure leak free fitting was also a feat. Direct measurement of the flows in the cryocooler provides very valuable data for validating an numerical model.

1.2.3 Development of the Volume Averaging Technique

The volume averaging technique is an analytical tool for describing the flow and heat transfer in a porous media. This technique has found extensive uses in ground water and pollution transport science, petroleum reservoir modeling, catalytic reactors, and fluidized beds to mention a few.

Hassanizadeh and Gray point out that there are at least three methodologies for describing the flow and heat transfer in multiphase systems, some of which rely mainly on intuition and empirical observations (41). While these methodologies have led to some of the original models, such as the Darcy model, the volume averaging technique provides a formal framework for improving the science of porous media. All of the current regenerator models in the open literature, such as REGEN and Sage, rely on the

intuitive and empirical knowledge of the flow in the regenerator without any application of the volume averaging technique. As a result, these models fall short of describing in an exact fashion the flow and heat transfer in the regenerator.

Whitaker has been fundamental in the development of the volume averaging technique and it application to a variety of problems; diffusion and dispersion in a reactor, conduction in multi-phase systems, development of conditions for nonhomogeneous porous media, local numerical studies and experimental validations to investigate the validity of volume averaging closure conditions (42). Whitaker's studies have mainly focused on incompressible flow, but he has briefly talked about the case of slightly compressible flow (43). Use of the volume averaging in this dissertation is applied to a problem which is highly compressible due mainly to the large pressure oscillations and the large temperature gradient across the regenerator.

1.2.4 Overview

To this end, the abundance of assumptions and modeling techniques for regenerators creates the need for a systematic study of the phenomenon based on fundamental conservation principles. This dissertation describes the derivation of the macroscopic equations which govern the regenerator problem. These equations are derived from the local governing equations for a generalized, compressible, real fluid. These equations are referred to as local equations since they describe the flow of the fluid within the pores. Thus, they are also referred to as the microscale equations. The microscale equations are then transformed into a set of macroscale governing equations

using volume-averaging. In this form, the governing equations describe the macroscopic flow behavior in addition to the effect that the microscale flow has on the macroscopic flow. The theory and details of the generalized volume-averaging technique is included in Appendix 1. Chapter 2 begins by summarizing the microscopic and macroscopic governing equations as developed in Appendix 1. Assumptions are then developed and discussed which allow the governing equations to be simplified. Closure relationships for friction, heat transfer, and dispersion are then developed to reduce the equation set to a tractable problem definition. The chapter concludes with a presentation of a set of illustrative exact solutions and scale analysis.

Chapter 3 details the development of a series of computational models. Several models are developed which can be used to study several limiting assumptions such as constant temperature and local thermal equilibrium. The numerical method used to solve these models is the Method of Lines. Of significant importance is the development of the artificial convergence technique which allows the problem to be converged rapidly. The chapter concludes with the development and results of an exact solution verification.

Chapter 4 details the development of the experimental apparatus and data. Regenerator steady flow data and system level cryocooler performance data is summarized and discussed.

Results and discussion are included in Chapter 5. A system level model is discussed which allows the regenerator boundary conditions to be estimated. The numerical results of the detailed regenerator model are presented and compared with the system level model. The limiting models which were developed in Chapter 3 are

compared with the full regenerator model. A comparison of two regenerator models from the literature, including the system level model, is provided for the baseline regenerator. Steady flow pressure drop data is used to predict friction factors using a compressible flow exact solution to the governing equations. This friction factor is compared with friction factors measured in oscillating flow yielding excellent agreement.

Chapter 6 concludes this dissertation. The important results are summarized. Future research topics are motivated and discussed.

CHAPTER 2

2. THEORETICAL DEVELOPMENT

2.1 Governing Equations and Constitutive Relations

The development of a theoretical model for flow and heat transfer in a generalized porous medium begins with a set of governing equations and constitutive relations for the thermohydraulic system illustrated in Figure 4. In this system, there is a solid and a fluid phase. The solid phase is assumed to be stationary and rigid with known thermal properties which are functions of temperature. The fluid phase is assumed to behave as a linearly viscous fluid. The fluid flow is assumed to be compressible, and the fluid properties are known functions of temperature and pressure, or another combination of state properties. The governing equations are derived in any fluid mechanics text and are repeated here.

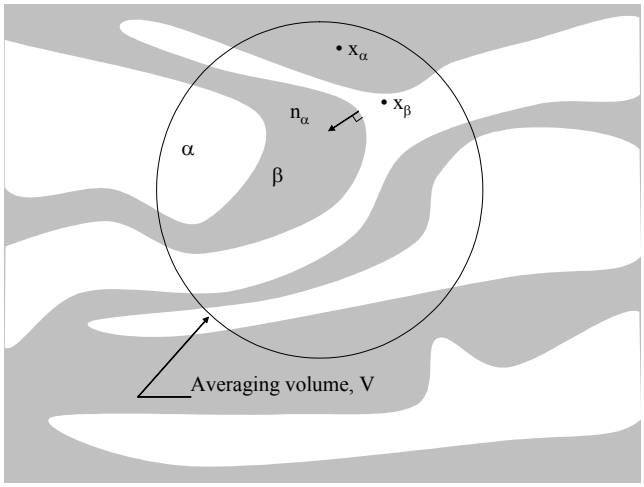

Figure 4 - Thermohydraulic system of a typical porous media. The α-phase is a Newtonian fluid and the β-phase is a solid.

2.1.1 Conservation of Mass Equation

The differential statement of mass conservation for the α-phase (in strong conservation form) is

$$\frac{\partial \rho_\alpha}{\partial t} + \nabla \cdot \left(\rho_\alpha \vec{u}_\alpha \right) = 0, \qquad \textbf{(2-1)}$$

where ρ_α is the *gas density* and $\vec{u}_\alpha$ is the *gas velocity vector*. This equation is a scalar equation with 4 unknowns; the fluid density and three components of the fluid velocity.

2.1.2 Balance of Momentum Equations

The differential statement of the balance of momentum for a Newtonian fluid with no body forces (in strong conservation form) is

$$\frac{\partial}{\partial t}\left(\rho_\alpha \vec{u}_\alpha \right) + \nabla \cdot \left(\rho_\alpha \vec{u}_\alpha \vec{u}_\alpha \right) + \nabla p_\alpha - \frac{1}{3} \nabla \left(\mu_\alpha \nabla \cdot \vec{u}_\alpha \right) - \nabla \cdot \left(\mu_\alpha \nabla \vec{u}_\alpha \right) = 0, \qquad \textbf{(2-2)}$$

where μ_α is the *gas viscosity coefficient*, and p_α is the *mechanical pressure*. This equation is a vector equation with three components corresponding to the three components of velocity. The balance of momentum equation produces 1 additional unknown, the fluid pressure. The viscosity is a material property and is thus known from experimental data.

2.1.3 α-Phase Conservation of Energy Equation

The differential statement of the conservation of energy for a Newtonian fluid in terms of the *gas specific internal energy*, e_α, is

$$\frac{\partial(\rho_\alpha e_\alpha)}{\partial t} + \nabla \cdot (\rho_\alpha \vec{u}_\alpha h_\alpha - k_\alpha \nabla T_\alpha) = 0, \tag{2-3}$$

where h_α is the *gas enthalpy* defined as

$$h_\alpha = e_\alpha + \frac{p_\alpha}{\rho_\alpha}. \tag{2-4}$$

It should be noted that Equation 2-3 is in strong conservation form. This is the preferred form for the conservation equations. In this form, the gradient of the enthalpy flow includes viscous dissipation, although it is not immediately obvious. Expanding this term gives

$$\begin{aligned} \nabla \cdot (\rho_\alpha \vec{u}_\alpha h_\alpha) &= \nabla \cdot (\rho_\alpha \vec{u}_\alpha e_\alpha + p_\alpha \vec{u}_\alpha) \\ &= \nabla \cdot (\rho_\alpha \vec{u}_\alpha e_\alpha) + p_\alpha \nabla \cdot \vec{u}_\alpha + \vec{u}_\alpha \cdot \nabla p_\alpha. \end{aligned} \tag{2-5}$$

Using Equation (2-2), the pressure gradient can be eliminated by solving in terms of the viscous and acceleration terms. It can then be shown that

$$\vec{u}_\alpha \cdot \nabla p_\alpha = -\mu_\alpha \phi_\alpha \tag{2-6}$$

where ϕ_α is the *viscous dissipation function* defined as

$$\phi_\alpha = -\frac{2}{3}(\nabla \cdot \vec{u}_\alpha)^2 + \frac{1}{2}\left(\nabla \vec{u}_\alpha : \nabla \vec{u}_\alpha + 2\nabla \vec{u}_\alpha : (\nabla \vec{u}_\alpha)^T + (\nabla \vec{u}_\alpha : \nabla \vec{u}_\alpha)^T\right). \tag{2-7}$$

The double dot notation represents the scalar product of two tensors, and the superscript "T" denoted the tensor transpose.

2.1.4 β-Phase Conservation of Energy Equation

For the β-phase, the conservation of energy equation is written as

$$(\rho c)_\beta \frac{\partial T_\beta}{\partial t} - \nabla \cdot \left(k_\beta \nabla T_\beta\right) = 0, \quad \textbf{(2-8)}$$

where $(\rho c)_\beta$ is the *solid heat capacity per unit volume*. Both energy equations are scalar equations introducing an additional 3 unknowns; the fluid and solid temperatures, and the fluid internal energy.

2.1.5 Equations of State

Thus far, the system of equations consists of six equations for eight unknowns, requiring two additional equations to close the problem. These equations are the gas and caloric equations of state which can be generally expressed as

$$p_\alpha = f_1(\rho_\alpha, e_\alpha) \quad \textbf{(2-9)}$$

and

$$T_\alpha = f_2(\rho_\alpha, e_\alpha). \quad \textbf{(2-10)}$$

The particular equations of state are arbitrary, and do not effect the form of the governing equations. Ideal gas equations or real gas equations can be used.

2.1.6 α-Phase Entropy Generation Equation

The differential statement of the second law of thermodynamics is given as

$$s'''_{gen,\alpha} = \frac{\partial(\rho_\alpha s_\alpha)}{\partial t} + \nabla \cdot (\rho_\alpha s_\alpha \vec{u}_\alpha) + \nabla \cdot \left(\frac{\vec{q}_\alpha}{T_\alpha} \right) \geq 0 \qquad \textbf{(2-11)}$$

where $s'''_{gen,\alpha}$ represents the *gas volumetric rate of entropy generation*. The entropy, s_α, is a thermodynamic property which is fundamental to optimizing any thermodynamic process. The inequality indicates that the entropy generation is always positive except for totally reversible processes, in which case, it is zero. It will be shown later that the entropy generation for the case of a porous media can be represented by three effects; local conduction due to molecular diffusion and dispersion, gas-to-matrix convective heat transfer through a finite film temperature difference, and flow losses due to viscous and inertial effects.

2.1.7 β-Phase Entropy Generation Equation

For the β-phase, the entropy generation equation is written as

$$s'''_{gen,\beta} = \frac{\partial(\rho_\beta s_\beta)}{\partial t} + \nabla \cdot \left(\frac{\vec{q}_\beta}{T_\beta} \right) \geq 0. \qquad \textbf{(2-12)}$$

The entropy generation in the solid phase is caused by local conduction due to molecular diffusion and gas-to-matrix convective heat transfer through a finite film temperature difference.

2.1.8 Summary of Equations

The system of equations represents 8 equations and 8 unknowns. Repeated here is this system of equations.

$$\frac{\partial \rho_\alpha}{\partial t} + \nabla \cdot \left(\rho_\alpha \vec{u}_\alpha\right) = 0 \tag{2-13}$$

$$\frac{\partial}{\partial t}\left(\rho_\alpha \vec{u}_\alpha\right) + \nabla \cdot \left(\rho_\alpha \vec{u}_\alpha \vec{u}_\alpha\right) + \nabla p_\alpha - \frac{1}{3}\nabla\left(\mu_\alpha \nabla \cdot \vec{u}_\alpha\right) - \nabla \cdot \left(\mu_\alpha \nabla \vec{u}_\alpha\right) = 0 \tag{2-14}$$

$$\frac{\partial\left(\rho_\alpha e_\alpha\right)}{\partial t} + \nabla \cdot \left(\rho_\alpha \vec{u}_\alpha h_\alpha - k_\alpha \nabla T_\alpha\right) = 0 \tag{2-15}$$

$$\left(\rho c\right)_\beta \frac{\partial T_\beta}{\partial t} - \nabla \cdot \left(k_\beta \nabla T_\beta\right) = 0 \tag{2-16}$$

$$s'''_{gen,\alpha} = \frac{\partial\left(\rho_\alpha s_\alpha\right)}{\partial t} + \nabla \cdot \left(\rho_\alpha s_\alpha \vec{u}_\alpha\right) + \nabla \cdot \left(\frac{\vec{q}_\alpha}{T_\alpha}\right) \geq 0 \tag{2-17}$$

$$s'''_{gen,\beta} = \frac{\partial\left(\rho_\beta s_\beta\right)}{\partial t} + \nabla \cdot \left(\frac{\vec{q}_\beta}{T_\beta}\right) \geq 0. \tag{2-18}$$

$$p_\alpha = f_1\left(\rho_\alpha, e_\alpha\right) \tag{2-19}$$

$$T_\alpha = f_2\left(\rho_\alpha, e_\alpha\right). \tag{2-20}$$

The unknowns are the local, instantaneous, non-volume averaged gas density, gas velocity, gas internal energy, gas temperature, matrix temperature, gas and matrix entropy generation, and gas pressure. These equations represent the microscale flow in the porous media. The flow geometry is far too complicated to allow for a direct application of these equations for any large scale porous system such as the regenerator.

The flow is best analyzed in terms of volume-averaged quantities. The derivation of the volume-averaged governing equations is the topic of Section 2.2.

2.2 Volume-Averaged Equations

The details of the volume averaging method are included as Appendix 1 in this document. The resulting equations are repeated here.

2.2.1 Volume-Averaged Conservation of Mass Equation

The volume average of Equation (2-13) is

$$\frac{\partial}{\partial t}\left\langle \rho_\alpha \right\rangle^\alpha + \nabla \cdot \left(\left\langle \rho_\alpha \right\rangle^\alpha \left\langle \vec{u}_\alpha \right\rangle^\alpha \right) + \frac{1}{\varepsilon_\alpha} \nabla \cdot \left\langle \hat{\rho}_\alpha \hat{\vec{u}}_\alpha \right\rangle = 0. \qquad \textbf{(2-21)}$$

where ε_α is the gas phase volume fraction, or porosity as defined in Appendix 1. The $\langle\ \rangle$ notation indicates a volume average which is also defined in Appendix 1. The "hat" notation indicates a spatial deviation quantity. The volume averaging results in an additional term to the standard continuity equation representing mass dispersion. This term will be addressed later.

2.2.2 Volume-Averaged Balance of Momentum Equation

The volume average of Equation (2-14) is

$$\begin{aligned}&\frac{\partial}{\partial t}\left(\langle\rho_\alpha\rangle^\alpha\langle\vec{u}_\alpha\rangle^\alpha\right)+\nabla\cdot\left(\langle\rho_\alpha\rangle^\alpha\langle\vec{u}_\alpha\rangle^\alpha\langle\vec{u}_\alpha\rangle^\alpha\right)+\nabla\langle p_\alpha\rangle^\alpha-\frac{1}{3}\nabla\left(\mu_\alpha\nabla\cdot\langle\vec{u}_\alpha\rangle^\alpha\right)-\nabla\cdot\left(\mu_\alpha\nabla\langle\vec{u}_\alpha\rangle^\alpha\right)\\&+\frac{1}{V_\alpha}\int_{A_{\alpha\beta}}n_\alpha\cdot\left[\tilde{I}\left(\hat{p}_\alpha-\frac{\mu_\alpha}{3}\nabla\cdot\hat{\vec{u}}_\alpha\right)-\mu_\alpha\nabla\hat{\vec{u}}_\alpha\right]dS\\&+\frac{1}{\varepsilon_\alpha}\frac{\partial}{\partial t}\left\langle\hat{\rho}_\alpha\hat{\vec{u}}_\alpha\right\rangle+\frac{1}{\varepsilon_\alpha}\nabla\cdot\left(\langle\rho_\alpha\rangle^\alpha\left\langle\hat{\vec{u}}_\alpha\hat{\vec{u}}_\alpha\right\rangle\right)+\frac{1}{\varepsilon_\alpha}\nabla\cdot\left(\langle\vec{u}_\alpha\rangle^\alpha\left\langle\hat{\rho}_\alpha\hat{\vec{u}}_\alpha\right\rangle\right)\\&+\frac{1}{\varepsilon_\alpha}\nabla\cdot\left(\left\langle\hat{\rho}_\alpha\hat{\vec{u}}_\alpha\right\rangle\langle\vec{u}_\alpha\rangle^\alpha\right)+\frac{1}{\varepsilon_\alpha}\nabla\cdot\left\langle\hat{\rho}_\alpha\hat{\vec{u}}_\alpha\hat{\vec{u}}_\alpha\right\rangle=0.\end{aligned}\qquad\textbf{(2-22)}$$

The volume averaging has produced multiple terms which need to be eventually represented as functions of the volume-averaged variables or eliminated justifiably.

2.2.3 Volume-Averaged α-Phase Conservation of Energy Equation

The volume average of Equation (2-15) is

$$\begin{aligned}&\frac{\partial\left(\langle\rho_\alpha\rangle^\alpha\langle e_\alpha\rangle^\alpha\right)}{\partial t}+\nabla\cdot\left(\langle\rho_\alpha\rangle^\alpha\langle\vec{u}_\alpha\rangle^\alpha\langle h_\alpha\rangle^\alpha\right)-\nabla\cdot\left[k_\alpha\left(\nabla\langle T_\alpha\rangle^\alpha+\frac{1}{V_\alpha}\int_{A_{\alpha\beta}}n_\alpha\hat{T}_\alpha dS\right)\right]\\&-\frac{1}{V_\alpha}\int_{A_{\alpha\beta}}n_\alpha\cdot k_\alpha\nabla T_\alpha dS+\frac{1}{\varepsilon_\alpha}\frac{\partial\left\langle\hat{\rho}_\alpha\hat{e}_\alpha\right\rangle}{\partial t}+\frac{1}{\varepsilon_\alpha}\nabla\cdot\left(\left\langle\hat{\rho}_\alpha\hat{\vec{u}}_\alpha\right\rangle\langle h_\alpha\rangle^\alpha\right)\\&+\frac{1}{\varepsilon_\alpha}\nabla\cdot\left(\langle\rho_\alpha\rangle^\alpha\left\langle\hat{\vec{u}}_\alpha\hat{h}_\alpha\right\rangle\right)+\frac{1}{\varepsilon_\alpha}\nabla\cdot\left(\left\langle\hat{\rho}_\alpha\hat{\vec{u}}_\alpha\right\rangle\langle h_\alpha\rangle^\alpha\right)+\frac{1}{\varepsilon_\alpha}\nabla\cdot\left\langle\hat{\rho}_\alpha\hat{\vec{u}}_\alpha\hat{h}_\alpha\right\rangle=0.\end{aligned}\qquad\textbf{(2-23)}$$

Again, the volume averaging has produced many additional terms which will be address in the following pages. The terms of the original energy equation have survived, except these terms are now in the form of volume-averaged quantities.

2.2.4 Volume-Averaged β-Phase Conservation of Energy Equation

The volume average of Equation (2-16) is

$$(\rho c)_\beta \frac{\partial \langle T_\beta \rangle^\beta}{\partial t} - \nabla \cdot \left[k_\beta \left(\nabla \langle T_\beta \rangle^\beta + \frac{1}{V_\beta} \int_{A_{\alpha\beta}} n_\beta \hat{T}_\beta dS \right) \right] - \frac{1}{V_\beta} \int_{A_{\alpha\beta}} n_\beta \cdot k_\beta \nabla T_\beta dS = 0. \quad \textbf{(2-24)}$$

Note that that the two energy equations, (2-23) and (2-24), are coupled via surface conduction heat transfer terms in the form of surface integrals over the α-β interface area. Later it will be shown that the surface integrals,

$$-\frac{1}{V_\alpha} \int_{A_{\alpha\beta}} n_\alpha \cdot k_\alpha \nabla T_\alpha dS \quad \textbf{(2-25)}$$

and

$$-\frac{1}{V_\beta} \int_{A_{\alpha\beta}} n_\beta \cdot k_\beta \nabla T_\beta dS, \quad \textbf{(2-26)}$$

represent the convection between the two phases.

2.2.5 Volume-Averaged α-Phase Entropy Generation Equation

The volume averaging of Equation (2-17) is

$$\begin{aligned}\left\langle s'''_{\alpha,gen}\right\rangle^{\alpha} &= \frac{\partial\left(\left\langle\rho_\alpha\right\rangle^{\alpha}\left\langle s_\alpha\right\rangle^{\alpha}\right)}{\partial t}+\frac{1}{\varepsilon_\alpha}\frac{\partial\left\langle\hat{\rho}_\alpha\hat{s}_\alpha\right\rangle}{\partial t}\\ &+\nabla\cdot\left(\left\langle\rho_\alpha\right\rangle^{\alpha}\left\langle s_\alpha\right\rangle^{\alpha}\left\langle\vec{u}_\alpha\right\rangle^{\alpha}\right)+\frac{1}{\varepsilon_\alpha}\nabla\cdot\left(\left\langle\hat{\rho}_\alpha\hat{s}_\alpha\right\rangle\left\langle\vec{u}_\alpha\right\rangle^{\alpha}\right)+\frac{1}{\varepsilon_\alpha}\nabla\cdot\left(\left\langle\rho_\alpha\right\rangle^{\alpha}\left\langle\hat{s}_\alpha\hat{\vec{u}}_\alpha\right\rangle\right)\\ &+\frac{1}{\varepsilon_\alpha}\nabla\cdot\left(\left\langle\hat{\rho}_\alpha\hat{\vec{u}}_\alpha\right\rangle\left\langle s_\alpha\right\rangle^{\alpha}\right)+\frac{1}{\varepsilon_\alpha}\nabla\cdot\left\langle\hat{\rho}_\alpha\hat{s}_\alpha\hat{\vec{u}}_\alpha\right\rangle\\ &-\frac{1}{\varepsilon_\alpha}\nabla\cdot\left[k_\alpha\left\langle\frac{\nabla T_\alpha}{T_\alpha}\right\rangle\right]-\frac{1}{V_\alpha}\int_{A_{\alpha\beta}}n_\alpha\cdot\frac{k_\alpha\nabla T_\alpha}{T_\alpha}dS\end{aligned} \tag{2-27}$$

2.2.6 Volume-Averaged β-Phase Entropy Generation Equation

The volume average of Equation (2-18) is

$$\left\langle s'''_{\beta,gen}\right\rangle^{\beta}=\rho_\beta\frac{\partial\left\langle s_\beta\right\rangle^{\beta}}{\partial t}-\frac{1}{\varepsilon_\beta}\nabla\cdot\left[k_\beta\left\langle\frac{\nabla T_\beta}{T_\beta}\right\rangle\right]-\frac{1}{V_\beta}\int_{A_{\alpha\beta}}n_\beta\cdot\frac{k_\beta\nabla T_\beta}{T_\beta}dS\,. \tag{2-28}$$

As with the energy equations, the entropy generation equations now contain terms which will be shown later to represent entropy generation due to solid-to-gas convection through a film temperature difference,

$$-\frac{1}{V_\alpha}\int_{A_{\alpha\beta}}n_\alpha\cdot\frac{k_\alpha\nabla T_\alpha}{T_\alpha}dS \tag{2-29}$$

and

$$-\frac{1}{V_\beta}\int_{A_{\alpha\beta}}n_\beta\cdot\frac{k_\beta\nabla T_\beta}{T_\beta}dS, \tag{2-30}$$

as well as entropy generation due to molecular diffusion,

$$-\frac{1}{\varepsilon_\alpha}\nabla\cdot\left[k_\alpha\left\langle\frac{\nabla T_\alpha}{T_\alpha}\right\rangle\right] \tag{2-31}$$

and

$$-\frac{1}{\varepsilon_\beta}\nabla\cdot\left[k_\beta\left\langle\frac{\nabla T_\beta}{T_\beta}\right\rangle\right]. \tag{2-32}$$

2.3 Simplifying Assumptions

At this point in the development of the volume-averaged equations, the assumptions are:

1) The solid phase is stationary and non-deforming.
2) The porosity is constant.
3) The fluid phase satisfies the no-slip condition on the fluid-solid interface.
4) Fluid and solid properties, such as conductivity and viscosity, can be treated as locally constant with respect to the averaging volume. Properties are assumed to vary with the intrinsic-averaged state variables.

To facilitate the equations to be in a tractable form, all terms containing deviation quantities must be expressed as functions of the averaged variables.

2.3.1 Density Spatial Deviation

The pore scale velocity varies across the cross section of a pore due to the no-slip Dirichlet boundary condition at the fluid-solid surface (see Figure 5.) This results in an order of magnitude estimate for the velocity deviation, $\hat{\vec{u}}_\alpha \sim \langle \vec{u}_\alpha \rangle^\alpha$.

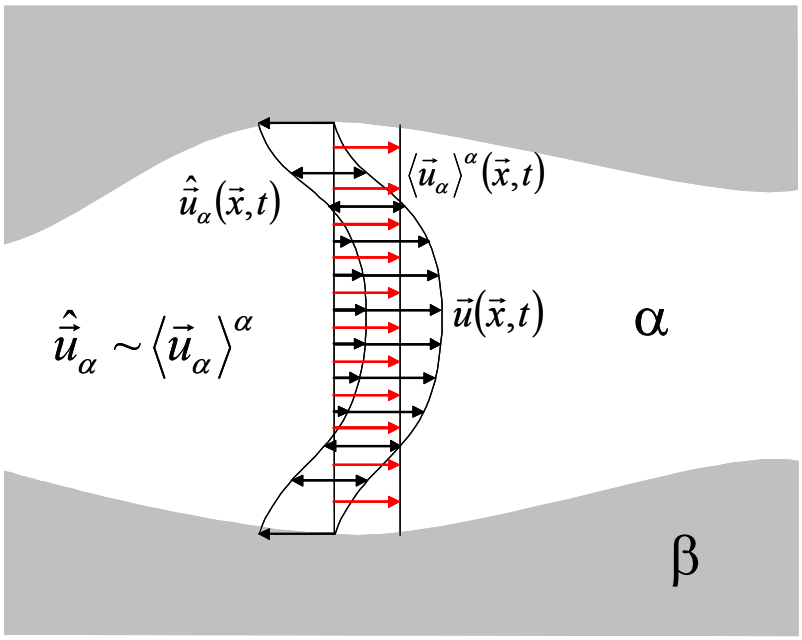

Figure 5 – Conceptual diagram illustrating the local velocity, velocity deviation, and the volume-averaged velocity.

Since density does not satisfy a Dirichlet boundary condition at the fluid-solid interface, the density deviation is small compared to the volume-averaged density (43). The consequence of this assumption is

$$\rho_\alpha = \langle \rho_\alpha \rangle^\alpha + \underbrace{\hat{\rho}_\alpha}_{negligible} \cong \langle \rho_\alpha \rangle^\alpha . \qquad \textbf{(2-33)}$$

The consequences of this assumption can be illustrated by considering the volume average of the ideal gas law which gives

$$\langle p_\alpha \rangle^\alpha = R\langle \rho_\alpha \rangle^\alpha \langle T_\alpha \rangle^\alpha + \frac{R}{\varepsilon_\alpha}\left\langle \hat{\rho}_\alpha \hat{T}_\alpha \right\rangle. \tag{2-34}$$

Neglecting the density deviation eliminates the last term in Equation (2-34), even though the temperature deviation is not negligible. This assumption will effectively eliminate a large number of terms in the volume-averaged equations. This conclusion is true for ideal or real gases.

2.3.2 Negligible Mechanical Dispersion

The mechanical dispersion term appearing in the momentum and energy equations is

$$\nabla \cdot \left(\langle \rho_\alpha \rangle^\alpha \left\langle \hat{\vec{u}}_\alpha \hat{\vec{u}}_\alpha \right\rangle \right). \tag{2-35}$$

Gray and O'Neill (44) identify the mechanical dispersion term appearing in the momentum equation. They propose that this term can be expressed as

$$\left\langle \hat{\vec{u}}_\alpha \hat{\vec{u}}_\alpha \right\rangle = \widetilde{D}_2 \langle \vec{u}_\alpha \rangle^\alpha = \widetilde{E}_3 \cdot \langle \vec{u}_\alpha \rangle^\alpha + \widetilde{G}_4 : \langle \vec{u}_\alpha \rangle^\alpha \langle \vec{u}_\alpha \rangle^\alpha \tag{2-36}$$

where the numerical subscripts represent the rank of the tensors. Whitaker (45) shows by scale analysis that the dispersion term for such flows is, in general, negligibly small in comparison to the surface integral which represents the Darcy and Forchheimer effects. Thus, this analysis will neglect the mechanical dispersion terms.

2.3.3 Thermal Dispersion

The thermal dispersion term in the fluid energy equation is

$$\nabla \cdot \left(\langle \rho_\alpha \rangle^\alpha \left\langle \hat{\vec{u}}_\alpha \hat{h}_\alpha \right\rangle \right). \tag{2-37}$$

This term can be at least an order of magnitude larger than the molecular diffusion term. Whitaker shows in an analogous fashion, that this dispersion is diffusive at the macroscopic scale and the dispersion coefficient is proportional to the Peclet number (42). Taking the molecular diffusion term and the dispersion term together, Whitaker suggests that these terms reduce to

$$-\nabla \cdot \left[\varepsilon_\alpha k_\alpha \left(\tilde{\mathrm{I}} + \frac{1}{V} \int_{A_{\alpha\beta}} n_\alpha \tilde{b}_\alpha dS \right) \nabla \langle T_\alpha \rangle^\alpha \right] - \nabla \cdot \left(\varepsilon_\alpha \langle \rho_\alpha \rangle^\alpha \tilde{D}_\alpha \cdot \nabla \langle h_\alpha \rangle^\alpha \right) \tag{2-38}$$

where the dispersion tensor is $\tilde{D}_\alpha$. The closure variable, $\tilde{b}_\alpha$, must be solved for numerically. The effective conductivity is then defined as

$$k_{\alpha,eff} = k_\alpha \left(\tilde{\mathrm{I}} + \frac{1}{V} \int_{A_{\alpha\beta}} n_\alpha \tilde{b}_\alpha dS \right). \tag{2-39}$$

Equation (2-38) can then be written as

$$-\nabla \cdot \left(\varepsilon_\alpha k_{\alpha,eff} \nabla \langle T_\alpha \rangle^\alpha + \varepsilon_\alpha \langle \rho_\alpha \rangle^\alpha \tilde{D}_\alpha \cdot \nabla \langle h_\alpha \rangle^\alpha \right) \tag{2-40}$$

which can be simplified assuming

$$\nabla \langle h_\alpha \rangle^\alpha = c_{p,\alpha} \nabla \langle T_\alpha \rangle^\alpha \tag{2-41}$$

to

$$-\nabla \cdot \left[\varepsilon_\alpha \left(k_{\alpha,eff} + \langle \rho_\alpha \rangle^\alpha c_{p,\alpha} \tilde{D}_\alpha \cdot \right) \nabla \langle T_\alpha \rangle^\alpha \right]. \tag{2-42}$$

Gedeon also recognizes this Peclet dependence (36). He calls this phenomenon axial-conductivity enhancement, which is an essential definition of thermal dispersion. He suggests that

$$k_{\alpha,eff} + \langle \rho_\alpha \rangle^\alpha c_{p,\alpha} D_{\alpha,xx} = k_\alpha \left(c_1 + c_2 \, \mathrm{Re}^m \, \mathrm{Pr}^n \right) = N_k k_\alpha \qquad \textbf{(2-43)}$$

and he reports coefficients for several matrices of interest for regenerators such as wire mesh screens and felts. This functional form for the dispersion agrees with other empirical predictions (42).

2.3.4 Entropy Generation Due to Thermal Dispersion

It was shown that the terms in the gas energy equation representing molecular diffusion and dispersion,

$$\frac{1}{\varepsilon_\alpha} \nabla \cdot \left(\langle \rho_\alpha \rangle^\alpha \left\langle \hat{\tilde{u}}_\alpha \hat{h}_\alpha \right\rangle \right) - \nabla \cdot \left[k_\alpha \left(\nabla \langle T_\alpha \rangle^\alpha + \frac{1}{V_\alpha} \int_{A_{\alpha\beta}} n_\alpha \hat{T}_\alpha dS \right) \right], \qquad \textbf{(2-44)}$$

reduce to

$$-\nabla \cdot \left(N_k k_\alpha \nabla \langle T_\alpha \rangle^\alpha \right).$$

The same terms in the gas entropy generation equation,

$$\frac{1}{\varepsilon_\alpha} \nabla \cdot \left(\langle \rho_\alpha \rangle^\alpha \left\langle \hat{s}_\alpha \hat{\tilde{u}}_\alpha \right\rangle \right) - \frac{1}{\varepsilon_\alpha} \nabla \cdot \left[k_\alpha \left\langle \frac{\nabla T_\alpha}{T_\alpha} \right\rangle \right], \qquad \textbf{(2-45)}$$

represent entropy generation due to dispersion and molecular diffusion, respectively. They reduce similarly to

$$-\nabla \cdot \left(\frac{N_k k_\alpha \nabla \langle T_\alpha \rangle^\alpha}{\langle T_\alpha \rangle^\alpha} \right).$$

2.3.5 Negligible Brinkman Effect

The Brinkman effect is represented by the term

$$\frac{1}{3}\nabla\left(\mu_\alpha \nabla\cdot\langle\vec{u}_\alpha\rangle^\alpha\right)+\nabla\cdot\left(\mu_\alpha\nabla\langle\vec{u}_\alpha\rangle^\alpha\right) \qquad \textbf{(2-46)}$$

and is generally negligible in comparison to the Darcy and Forchheimer effects (45). The Brinkman effect will be neglected in this analysis, yielding a spatially first order momentum equation.

2.3.6 One Dimensional Model on the Macroscopic Length Scale

It is improper to impose a no-slip boundary condition on the macroscopic problem of a porous medium bounded by a solid surface. The wall can only satisfy a no-slip boundary condition for the microscopic flow problem. The solid wall that contains the regenerator matrix has minimal effect on the macroscopic flow field. The microscale flow is affected by viscous shear and interfacial heat transfer. Both of these effects are related to surface area. For an averaging volume containing the wall, the ratio of the wall surface area to the matrix surface area will be quite small. It is reasonable to conclude that the wall will have minimal effect on the macroscopic flow in the axial direction. For a 2-D axisymmetric flow, the wall boundary condition is simply zero normal velocity, which reduces to zero radial velocity for a cylindrical regenerator.

Typically the flow passages at the ends of the regenerator are designed with a contraction in diameter in an effort to minimize dead volume. This will lead to flow jetting at the ends of the regenerator necessitating the need for a 2D model. It is not clear how this flow jetting will affect the regenerator performance, and this is an area of

ongoing research. For the current model, it is assumed that the flow approaches the regenerator with a uniform profile. In this situation, there is no driving force to create anything other than a one dimensional macroscopic flow field.

The regenerator is bounded on the ends by a homogeneous fluid in which the differential continuum equations are valid. The transitional region between the homogeneous fluid and homogeneous porous medium has been analyzed by Ochoa-Tapia and Whitaker (46, 47, 48). They find that the transition creates a jump condition in the momentum and energy equations. These conditions lead to additional parameters which need to be measured experimentally. Further analysis is needed to determine the magnitude of these effects.

2.4 Simplified Equations

The preceding assumptions lead to a large reduction in the equation complexity. Several additional terms remain which need to be represented in terms of volume averaged quantities. These relations are developed in the following discussion.

2.4.1 Simplified Conservation of Mass Equation

Under these assumptions, the volume-averaged conservation of mass equation (2-21) becomes

$$\frac{\partial \rho_\alpha}{\partial t} + \frac{\partial}{\partial x}\left(\rho_\alpha u_\alpha\right) = 0. \qquad \textbf{(2-47)}$$

where the volume averaging notation has been dropped where appropriate. This is the standard one dimensional continuity equation in terms of volume-averaged quantities.

2.4.2 Simplified Balance of Momentum Equation

The momentum equation (2-22) becomes

$$\frac{\partial}{\partial t}(\rho_\alpha u_\alpha)+\frac{\partial}{\partial x}(\rho_\alpha u_\alpha u_\alpha)+\frac{\partial p_\alpha}{\partial x}$$
$$+\underbrace{\frac{1}{V_\alpha}\int_{A_{\alpha\beta}} n_\alpha\cdot\left[\tilde{I}\left(\hat{p}_\alpha-\frac{\mu_\alpha}{3}\nabla\cdot\hat{\bar{u}}_\alpha\right)-\mu_\alpha\nabla\hat{\bar{u}}_\alpha\right]dS}_{\text{Darcy and Forchheimer effects}}=0 \qquad \textbf{(2-48)}$$

which still contains the surface integral of the deviation quantities. Following the analysis of Whitaker (45), the surface integral in Equation (2-48) can be written such that

$$\frac{\partial}{\partial t}(\rho_\alpha u_\alpha)+\frac{\partial}{\partial x}(\rho_\alpha u_\alpha u_\alpha)+\frac{\partial p_\alpha}{\partial x}+\mu_\alpha\varepsilon_\alpha\left\{\tilde{K}^{-1}\cdot\left[\tilde{I}+\tilde{F}\right]\right\}_{xx}u_\alpha=0. \qquad \textbf{(2-49)}$$

The permeability, K, and form drag coefficient, c_f, are defined as

$$\tilde{K}_{xx}=K$$
$$\tilde{F}_{xx}=\varepsilon_\alpha c_f\underbrace{\frac{\rho_\alpha u_\alpha K^{1/2}}{\mu_\alpha}}_{\mathrm{Re}_K}sign[u_\alpha]. \qquad \textbf{(2-50)}$$

Note that the Forchheimer correction is expressed in terms of a Reynolds number based on the permeability length scale. The permeability has units of length squared. The momentum equation is now written as

$$\frac{\partial}{\partial t}(\rho_\alpha u_\alpha)+\frac{\partial}{\partial x}(\rho_\alpha u_\alpha u_\alpha)+\frac{\partial p_\alpha}{\partial x}+\frac{\mu_\alpha\varepsilon_\alpha}{K}u_\alpha+\rho_\alpha u_\alpha{}^2\frac{\varepsilon_\alpha{}^2 c_f}{K^{1/2}}sign[u_\alpha]=0. \qquad \textbf{(2-51)}$$

2.4.3 Simplified α-Phase Conservation of Energy Equation

The volume-averaged conservation of energy equation for the α-phase (2-23) can be simplified to

$$\frac{\partial\left(\langle\rho_\alpha\rangle^\alpha\langle e_\alpha\rangle^\alpha\right)}{\partial t}+\frac{\partial}{\partial x}\left(\langle\rho_\alpha\rangle^\alpha\langle u_\alpha\rangle^\alpha\langle h_\alpha\rangle^\alpha-N_k k_\alpha\frac{\partial\langle T_\alpha\rangle^\alpha}{\partial x}\right)$$
$$-\frac{1}{V_\alpha}\int_{A_{\alpha\beta}} n_\alpha\cdot k_\alpha\nabla T_\alpha dS=0. \qquad \textbf{(2-52)}$$

2.4.4 Simplified β-Phase Conservation of Energy Equation

The β-phase conservation of energy equation (2-24) can be simplified to

$$(\rho c)_\beta\frac{\partial\langle T_\beta\rangle^\beta}{\partial t}-\frac{\partial}{\partial x}\left[k_\beta\left(\frac{\partial\langle T_\beta\rangle^\beta}{\partial x}+\frac{1}{V_\beta}\int_{A_{\alpha\beta}} n_\beta\hat{T}_\beta dS\right)\right]$$
$$-\frac{1}{V_\beta}\int_{A_{\alpha\beta}} n_\beta\cdot k_\beta\nabla T_\beta dS=0. \qquad \textbf{(2-53)}$$

The last term in Equation (2-53) is a surface integral representing the volumetric heat transfer between the two phases. The same integral appears in Equation (2-52). These two integrals are exactly of the same magnitude and are opposite in sign. Whitaker (42) has proposed that these integrals be represented as

$$-\frac{\varepsilon_\beta}{\varepsilon_\alpha}\frac{1}{V_\beta}\int_{A_{\alpha\beta}} n_\beta\cdot k_\beta\nabla T_\beta dS=\frac{1}{V_\alpha}\int_{A_{\alpha\beta}} n_\alpha\cdot k_\alpha\nabla T_\alpha dS=a_v H\left(\langle T_\beta\rangle^\beta-\langle T_\alpha\rangle^\alpha\right), \qquad \textbf{(2-54)}$$

where a_vH is the volumetric heat transfer coefficient. Substitution of Equation (2-54) into Equation (2-52) and Equation (2-53) results in a two-equation energy model

$$\frac{\partial\left(\langle\rho_\alpha\rangle^\alpha\langle e_\alpha\rangle^\alpha\right)}{\partial t}+\frac{\partial}{\partial x}\left(\langle\rho_\alpha\rangle^\alpha\langle u_\alpha\rangle^\alpha\langle h_\alpha\rangle^\alpha-N_k k_\alpha\frac{\partial\langle T_\alpha\rangle^\alpha}{\partial x}\right)$$
$$-a_v H\left(\langle T_\beta\rangle^\beta-\langle T_\alpha\rangle^\alpha\right)=0 \qquad \textbf{(2-55)}$$

and

$$(\rho c)_\beta\frac{\partial\langle T_\beta\rangle^\beta}{\partial t}-\frac{\partial}{\partial x}\left[k_\beta\left(\frac{\partial\langle T_\beta\rangle^\beta}{\partial x}+\frac{1}{V_\beta}\int_{A_{\alpha\beta}}n_\beta\hat{T}_\beta dS\right)\right]$$
$$+\frac{\varepsilon_\alpha}{\varepsilon_\beta}a_v H\left(\langle T_\beta\rangle^\beta-\langle T_\alpha\rangle^\alpha\right)=0. \qquad \textbf{(2-56)}$$

The conduction term in Equation (2-56) can be written as

$$-\frac{\partial}{\partial x}\left[k_\beta\left(\tilde{\mathrm{I}}+\frac{1}{V}\int_{A_{\alpha\beta}}n_\beta\tilde{b}_\beta dS\right)\frac{\partial\langle T_\beta\rangle^\beta}{\partial x}\right]=-\frac{\partial}{\partial x}\left[k_\beta\tau_\beta\frac{\partial\langle T_\beta\rangle^\beta}{\partial x}\right] \qquad \textbf{(2-57)}$$

where τ_β is referred to as the "tortuosity" by Gedeon (36). The terminology for tortuosity can be confusing since tortuosity is also used in the context of the fluid phase. The closure variable, $\tilde{b}_\beta$, must be solved for numerically. Experiments have suggested that the tortuosity is less than or equal to one. Tortuosity equal to one represents parallel path geometries such as tube bundles. Geometries such as wire mesh, felts, and sintered metals have tortuosities less than one. Unlike dispersion, the tortuosity is thought to be a function of geometry only, and not the flow field. Using this result, and dropping the volume averaging notation, the energy equations can be respectively written in final form as

$$\frac{\partial(\rho_\alpha e_\alpha)}{\partial t}+\frac{\partial}{\partial x}\left(\rho_\alpha u_\alpha h_\alpha - N_k k_\alpha \frac{\partial T_\alpha}{\partial x}\right)-a_v H\left(T_\beta - T_\alpha\right)=0 \tag{2-58}$$

and

$$(\rho c)_\beta \frac{\partial T_\beta}{\partial t}-\frac{\partial}{\partial x}\left[k_\beta \tau_\beta \frac{\partial T_\beta}{\partial x}\right]+\frac{\varepsilon_\alpha}{\varepsilon_\beta}a_v H\left(T_\beta - T_\alpha\right)=0. \tag{2-59}$$

2.4.5 Simplified α-Phase Entropy Generation Equation

The simplified gas entropy generation equation (2-27) is

$$\begin{aligned}\left\langle s'''_{\alpha,gen}\right\rangle^\alpha &= \frac{\partial\left(\left\langle\rho_\alpha\right\rangle^\alpha\left\langle s_\alpha\right\rangle^\alpha\right)}{\partial t}+\frac{\partial}{\partial x}\left(\left\langle\rho_\alpha\right\rangle^\alpha\left\langle s_\alpha\right\rangle^\alpha\left\langle\vec{u}_\alpha\right\rangle^\alpha\right)\\ &-\frac{\partial}{\partial x}\left[\frac{N_k k_\alpha}{\left\langle T_\alpha\right\rangle^\alpha}\frac{\partial}{\partial x}\left\langle T_\alpha\right\rangle^\alpha\right]-\frac{1}{V_\alpha}\int_{A_{\alpha\beta}} n_\alpha\cdot\frac{k_\alpha\nabla T_\alpha}{T_\alpha}dS\geq 0\end{aligned} \tag{2-60}$$

2.4.6 Simplified β-Phase Entropy Generation Equation

The simplified gas entropy generation equation (2-28) is

$$\left\langle s'''_{\beta,gen}\right\rangle^\beta=\rho_\beta\frac{\partial\left\langle s_\beta\right\rangle^\beta}{\partial t}-\frac{\partial}{\partial x}\left[\frac{k_\beta\tau_\beta}{\left\langle T_\beta\right\rangle^\beta}\frac{\partial}{\partial x}\left\langle T_\beta\right\rangle^\beta\right]-\frac{1}{V_\beta}\int_{A_{\alpha\beta}} n_\beta\cdot\frac{k_\beta\nabla T_\beta}{T_\beta}dS\geq 0 \tag{2-61}$$

The last term in Equation (2-60) is a surface integral representing the entropy generation due to volumetric heat transfer between the two phases. The same integral appears in Equation (2-61). By a similar method as that with the energy method, these terms can be expressed as

$$-\frac{1}{V_\beta}\int_{A_{\alpha\beta}} n_\beta \cdot \frac{k_\beta \nabla T_\beta}{T_\beta} dS = \frac{a_v H}{\langle T_\alpha \rangle^\alpha}\left(\langle T_\beta \rangle^\beta - \langle T_\alpha \rangle^\alpha\right) \quad \textbf{(2-62)}$$

and

$$\frac{1}{V_\alpha}\int_{A_{\alpha\beta}} n_\alpha \cdot \frac{k_\alpha \nabla T_\alpha}{T_\alpha} dS = \frac{a_v H}{\langle T_\beta \rangle^\beta}\left(\langle T_\beta \rangle^\beta - \langle T_\alpha \rangle^\alpha\right) \quad \textbf{(2-63)}$$

Substitution of Equation (2-62) and Equation (2-63) into the entropy generation model and dropping the volume averaging notation results in

$$s'''_{\alpha,gen} = \frac{\partial(\rho_\alpha s_\alpha)}{\partial t} + \frac{\partial}{\partial x}(\rho_\alpha u_\alpha s_\alpha) - \frac{\partial}{\partial x}\left[\frac{N_k k_\alpha}{T_\alpha}\frac{\partial T_\alpha}{\partial x}\right] - \frac{a_v H}{T_\beta}(T_\beta - T_\alpha) \quad \textbf{(2-64)}$$

and

$$s'''_{\beta,gen} = \rho_\beta \frac{\partial s_\beta}{\partial t} - \frac{\partial}{\partial x}\left[\frac{k_\beta \tau_\beta}{T_\beta}\frac{\partial T_\beta}{\partial x}\right] + \frac{a_v H}{T_\alpha}(T_\beta - T_\alpha). \quad \textbf{(2-65)}$$

At this point, it is possible to write the entropy generation rate equation for the gas-matrix system, which is

$$s'''_{gen,sys} = \varepsilon_\alpha s'''_{\alpha,gen} + \varepsilon_\beta s'''_{\beta,gen} \geq 0. \quad \textbf{(2-66)}$$

By using the Bridgman tables (49) the Maxwell relation for a pure substance can be written in a more convenient form as

$$ds = \frac{1}{\rho T}(dE - h d\rho), \quad \textbf{(2-67)}$$

which can then be used to simplify the entropy generation equations for the gas and the matrix. After considerable simplification, using the energy and momentum equations, the gas entropy generation equation reduces to

$$s'''_{\alpha,gen} = \frac{N_k k_\alpha}{T_\alpha^{\,2}}\left(\frac{\partial T_\alpha}{\partial x}\right)^2 + \frac{a_v H}{T_\alpha T_\beta}\left|T_\beta - T_\alpha\right|^2 - \frac{u_\alpha}{T_\alpha}\frac{\partial p_\alpha}{\partial x}. \qquad \textbf{(2-68)}$$

For an incompressible substance, the Maxwell Relation reduces to

$$ds = \frac{c}{T}dT, \qquad \textbf{(2-69)}$$

which, together with the matrix energy equation, and the matrix entropy generation equation reduces to

$$s'''_{\beta,gen} = \frac{k_\beta \tau_\beta}{T_\beta^{\,2}}\left(\frac{\partial T_\beta}{\partial x}\right)^2 + \frac{a_v H}{T_\alpha T_\beta}\left|T_\beta - T_\alpha\right|^2. \qquad \textbf{(2-70)}$$

Now the system entropy generation equation can be written

$$s'''_{gen,sys} = \underbrace{\varepsilon_\alpha \frac{N_k k_\alpha}{T_\alpha^{\,2}}\left(\frac{\partial T_\alpha}{\partial x}\right)^2}_{\text{Gas conduction}} + \underbrace{\varepsilon_\beta \frac{k_\beta \tau_\beta}{T_\beta^{\,2}}\left(\frac{\partial T_\beta}{\partial x}\right)^2}_{\text{Matrix conduction}} + \underbrace{\frac{a_v H}{T_\alpha T_\beta}\left|T_\beta - T_\alpha\right|^2}_{\text{Film heat transfer}} \underbrace{- \varepsilon_\alpha \frac{u_\alpha}{T_\alpha}\frac{\partial p_\alpha}{\partial x}}_{\text{viscous and inertial losses}} \geq 0. \qquad \textbf{(2-71)}$$

It should be noted that all terms are positive definite, including the last term representing entropy generation due to viscous and inertial losses. This requires that the sign of the pressure gradient always be opposite to the sign of the velocity. This is an interesting result, but not one that is immediately obvious. Using the momentum equation, this term can be written as

$$-\frac{u_\alpha}{T_\alpha}\frac{\partial p_\alpha}{\partial x} = \frac{u_\alpha}{T_\alpha}\left(\frac{\partial \rho_\alpha u_\alpha}{\partial t} + \frac{\partial \rho_\alpha u_\alpha u_\alpha}{\partial x} + F\right) \geq 0 \qquad \textbf{(2-72)}$$

where F is the Darcy-Forchheimer surface integral,

$$F = \frac{1}{V_\alpha}\int_{A_{\alpha\beta}} n_\alpha \cdot \left[\tilde{I}\left(\hat{p}_\alpha - \frac{\mu_\alpha}{3}\nabla\cdot\hat{\vec{u}}_\alpha \right) - \mu_\alpha \nabla \hat{\vec{u}}_\alpha \right] dS. \qquad \textbf{(2-73)}$$

This indicates that if F IS NOT a strict function of velocity as proposed then it must combine with the acceleration terms such that the entropy generation is positive definite. For positive velocity

$$F \geq -\frac{\partial \rho_\alpha u_\alpha}{\partial t} - \frac{\partial \rho_\alpha u_\alpha u_\alpha}{\partial x} \qquad \textbf{(2-74)}$$

and for negative velocity

$$F \leq -\frac{\partial \rho_\alpha u_\alpha}{\partial t} - \frac{\partial \rho_\alpha u_\alpha u_\alpha}{\partial x}. \qquad \textbf{(2-75)}$$

The other implication which is possible to extract from this result is that if F IS a strict function of velocity, as proposed, then the acceleration terms should be eliminated from the momentum equation. This produces the positive definite result

$$-\frac{u_\alpha}{T_\alpha}\frac{\partial p_\alpha}{\partial x} = \frac{u_\alpha}{T_\alpha}F = \frac{1}{T_\alpha}\left\{ \frac{\mu\varepsilon}{K}\left|u_\alpha\right|^2 + \rho_\alpha \left|u_\alpha\right|^3 \frac{\varepsilon^2 c_f}{K^{1/2}} \right\} \geq 0 \ . \qquad \textbf{(2-76)}$$

There is an additional requirement on the functionality of the interfacial convection terms. The assumptions imposed by Equation (2-54) must satisfy the additional requirement that

$$\frac{a_v H}{\langle T_\alpha \rangle^\alpha \langle T_\beta \rangle^\beta} \left| \langle T_\beta \rangle^\beta - \langle T_\alpha \rangle^\alpha \right|^2$$
$$= \int_{A_{\alpha\beta}} \left(\frac{1}{V_\alpha} \frac{\hat{T}_\alpha}{\langle T_\alpha \rangle^\alpha T_\alpha} - \frac{1}{V_\beta} \frac{\hat{T}_\beta}{\langle T_\beta \rangle^\beta T_\beta} \right) n_\alpha \cdot k_\alpha \nabla T_\alpha dS \geq 0. \quad \textbf{(2-77)}$$

where the volume averaging notation is reapplied for clarity. This statement is produced by retaining the surface integrals representing the interfacial heat transfer through the simplification process for the gas and matrix entropy generation equations. In this form, it is clear that the entropy generation due to this effect is directly dependent on the temperature deviation quantities, $\hat{T}_\alpha$ and $\hat{T}_\beta$, which are defined in the Appendix 1. These quantities are proportional to the volume-averaged temperature difference.

The entropy generation can be used to calculate lost available power by integrating the volumetric entropy generation rate over the entire regenerator. The lost power is then the total entropy generation rate times the reference temperature giving

$$\dot{W}_{lost} = T_o \int_0^L s'''_{gen,sys} A dx$$
$$= T_o \int_0^{L_r} \left[\varepsilon_\alpha \frac{N_k k_\alpha}{T_\alpha^{\,2}} \left(\frac{\partial T_\alpha}{\partial x} \right)^2 + \varepsilon_\beta \frac{k_\beta \tau_\beta}{T_\beta^{\,2}} \left(\frac{\partial T_\beta}{\partial x} \right)^2 + \frac{a_v H}{T_\alpha T_\beta} \left| T_\beta - T_\alpha \right|^2 - \varepsilon_\alpha \frac{u_\alpha}{T_\alpha} \frac{\partial p_\alpha}{\partial x} \right] A dx. \quad \textbf{(2-78)}$$

The reference temperature is the lowest naturally occurring temperature in the system. The lost power represents the additional input power that is required to perform the same thermodynamic function as compared to an internally reversible refrigerator. The lost power is a scalar value which can then be used as an optimization parameter. This idea is not investigated beyond this level in the dissertation other than calculating this value in Chapter 5. This form of the lost power represents an internal method of calculation. An

alternative method can be considered based on an external control volume. The lost power for a quasi-steady system with only mass flow interactions with the external environment can be found by cyclical integration of the entropy flux at the boundaries. These two methods of calculating the lost power will give identical results for an analytical system, but differences will be notices for a numerical approximation. This provides a good method for evaluating the accuracy of a numerical scheme. Values of this lost power discrepancy are reported in Chapter 5 for the numerical model presented in Chapter 3.

2.4.7 Summary of Equations

The system of equations representing the one dimensional regenerator is repeated here with the volume average notations removed. The mass flux is defined as m, and the volumetric gas internal energy is defined as E. The α-subscripts are dropped for simplicity. The porosity of the solid phase is defined to be one minus the gas porosity, ε.

$$\frac{\partial \rho}{\partial t} + \frac{\partial m}{\partial x} = 0 \qquad \textbf{(2-79)}$$

$$\frac{\partial m}{\partial t} + \frac{\partial}{\partial x}\left(\frac{m^2}{\rho} + p\right) + \frac{\mu\varepsilon}{K}\frac{m}{\rho} + \frac{m^2}{\rho}\frac{\varepsilon^2 c_f}{K^{1/2}}\,sign[m] = 0 \qquad \textbf{(2-80)}$$

$$\frac{\partial E}{\partial t} + \frac{\partial}{\partial x}\left(mh - N_k k\frac{\partial T}{\partial x}\right) - a_v H\left(T_\beta - T\right) = 0 \qquad \textbf{(2-81)}$$

$$\left(\rho c\right)_\beta \frac{\partial T_\beta}{\partial t} - \frac{\partial}{\partial x}\left[k_\beta \tau_\beta \frac{\partial T_\beta}{\partial x}\right] + \frac{\varepsilon}{1-\varepsilon} a_v H\left(T_\beta - T\right) = 0 \qquad \textbf{(2-82)}$$

$$s'''_{gen} = \frac{N_k k}{T^2}\left(\frac{\partial T}{\partial x}\right)^2 + \frac{a_v H}{T T_\beta}\left|T_\beta - T\right|^2 - \frac{m}{\rho T}\frac{\partial p}{\partial x} \tag{2-83}$$

$$s'''_{\beta,gen} = \frac{k_\beta \tau_\beta}{T_\beta{}^2}\left(\frac{\partial T_\beta}{\partial x}\right)^2 + \frac{\varepsilon}{1-\varepsilon}\frac{a_v H}{T T_\beta}\left|T_\beta - T\right|^2 \tag{2-84}$$

$$s'''_{gen,sys} = \varepsilon\frac{N_k k}{T^2}\left(\frac{\partial T}{\partial x}\right)^2 + (1-\varepsilon)\frac{k_\beta \tau_\beta}{T_\beta{}^2}\left(\frac{\partial T_\beta}{\partial x}\right)^2 + \frac{a_v H}{T T_\beta}\left|T_\beta - T\right|^2 - \varepsilon\frac{m}{\rho T}\frac{\partial p}{\partial x} \geq 0. \tag{2-85}$$

$$T = f_1(\rho, E) \tag{2-86}$$

$$p = f_2(\rho, E) \tag{2-87}$$

This system of PDEs represents 9 equations to be solved for

ρ Gas density

m Gas mass flux

E Gas total energy per unit volume

T Gas temperature

p Gas pressure

T_β Matrix temperature

s'''_{gen} Gas volumetric entropy generation rate

$s'''_{\beta,gen}$ Matrix volumetric entropy generation rate

$s'''_{gen,sys}$ Total volumetric entropy generation rate

The volumetric total energy, E, is chosen as the conserved quantity in the gas energy equation. This is simply the product of the internal energy and density. These equations require appropriate boundary and initial conditions which will be discussed.

These equations represent a fully compressible model for flow and heat transfer in a porous medium. The porous medium is completely characterized by the specification of the porosity, friction factor, dispersion coefficient, solid tortuosity, and heat transfer coefficient in addition to fluid and solid thermal properties. At this point in the development, these equations apply to one-dimensional steady, unsteady, or oscillating flow. For limiting cases, important exact solutions exist, and these are discussed in section 2.5 that follows.

2.5 Exact Solutions

Experimental measurement of the permeability and inertia coefficient is conducted by measuring the steady mass flow rate and pressure drop through a one-dimensional channel. Under steady state conditions, the first term in Equation (2-51) is zero, and the momentum equation reduces to

$$\rho_\alpha u_\alpha \frac{du_\alpha}{dx} + \frac{dp_\alpha}{dx} + \frac{\mu_\alpha \varepsilon_\alpha}{K} u_\alpha + \rho_\alpha {u_\alpha}^2 \frac{{\varepsilon_\alpha}^2 c_f}{K^{1/2}} sign[u_\alpha] = 0. \tag{2-88}$$

The continuity equation reduces to

$$\rho_\alpha u_\alpha = C_1 \Rightarrow \rho_\alpha = \frac{C_1}{u_\alpha}, \tag{2-89}$$

and the momentum equation becomes (for positive velocity and ideal gas)

$$\left[\frac{{u_\alpha}^2 - RT}{{u_\alpha}^3}\right]\frac{du_\alpha}{dx} = -\left[\frac{\mu_\alpha \varepsilon_\alpha}{KC_1} + \frac{{\varepsilon_\alpha}^2 c_f}{K^{1/2}}\right], \tag{2-90}$$

which can be integrated to give

$$Ln(u_\alpha)+\frac{RT}{2u_\alpha{}^2}=-\left[\frac{\mu_\alpha\varepsilon_\alpha}{KC_1}+\frac{\varepsilon_\alpha{}^2 c_f}{K^{1/2}}\right]x+C_2. \tag{2-91}$$

The two constants can now be solved to give

$$C_1=\frac{\dot{m}}{A_f} \tag{2-92}$$

and

$$C_2=Ln\left(\frac{\dot{m}RT}{A_f p_0}\right)+\frac{A_f{}^2 p_0{}^2}{2\dot{m}^2 RT}, \tag{2-93}$$

where p_0 is the pressure at the inlet. The result is an implicit equation for velocity which apparently needs to be solved numerically,

$$\frac{1}{RT}Ln\left(\frac{u_\alpha A_f p_0}{\dot{m}RT}\right)+\frac{1}{2u_\alpha{}^2}=\frac{1}{2}\left(\frac{p_0 A_f}{RT\dot{m}}\right)^2-\left[\frac{A_f\mu_\alpha\varepsilon_\alpha}{RT\dot{m}K}+\frac{\varepsilon_\alpha{}^2 c_f}{RTK^{1/2}}\right]x. \tag{2-94}$$

Equation (2-94) represents a steady, compressible, isothermal Forchheimer momentum equation. This equation allows the selection of the mass flow rate and the inlet pressure. By solving for the velocity at the outlet allows for calculating the density at the outlet, and thus the pressure, as outlined in what follows. In such a manner, experimental data can be used to solve for the two Darcy and Forchheimer coefficients iteratively.

If the convective acceleration term is neglected in the momentum equation, an additional exact solution can be obtained for the case of steady, isothermal, compressible flow. The problem is defined by

$$\rho_\alpha = \frac{\dot{m}}{u_\alpha A_f} \Rightarrow \frac{d\rho_\alpha}{dx} = -\frac{\dot{m}}{A_f {u_\alpha}^2}\frac{du_\alpha}{dx} \tag{2-95}$$

$$\frac{1}{{u_\alpha}^3}\frac{du_\alpha}{dx} = \frac{A_f \mu_\alpha \varepsilon_\alpha}{RT\dot{m}K} + \frac{{\varepsilon_\alpha}^2 c_f}{RTK^{1/2}}\,, \tag{2-96}$$

which can be integrated to give

$$\frac{1}{2{u_\alpha}^2} = C - \left(\frac{A_f \mu_\alpha \varepsilon_\alpha}{RT\dot{m}K} + \frac{{\varepsilon_\alpha}^2 c_f}{RTK^{1/2}}\right)x\,. \tag{2-97}$$

The constant can be solved to give

$$C = \frac{1}{2}\left(\frac{p_0 A_f}{RT\dot{m}}\right)^2\,. \tag{2-98}$$

The result is an equation for velocity,

$$\frac{1}{2{u_\alpha}^2} = \frac{1}{2}\left(\frac{p_0 A_f}{RT\dot{m}}\right)^2 - \left(\frac{A_f \mu_\alpha \varepsilon_\alpha}{RT\dot{m}K} + \frac{{\varepsilon_\alpha}^2 c_f}{RTK^{1/2}}\right)x\,, \tag{2-99}$$

which is identical to Equation (2-94) after dropping the natural logarithm term. This equation can be solved directly for the velocity giving

$$u_\alpha = \sqrt{\left[\left(\frac{p_0 A_f}{RT\dot{m}}\right)^2 - 2\left(\frac{A_f \mu_\alpha \varepsilon_\alpha}{RT\dot{m}K} + \frac{{\varepsilon_\alpha}^2 c_f}{RTK^{1/2}}\right)x\right]^{-1}}\,. \tag{2-100}$$

If the flow is steady, isothermal, and incompressible, the continuity equation reduces to

$$\frac{du_\alpha}{dx} = 0 \tag{2-101}$$

and the Forchheimer Momentum Equation reduces to

$$\frac{dp_\alpha}{dx} + \frac{\mu_\alpha \varepsilon_\alpha}{K} u_\alpha + \rho_\alpha {u_\alpha}^2 \frac{{\varepsilon_\alpha}^2 c_f}{K^{1/2}} sign[u_\alpha] = 0 \,, \tag{2-102}$$

which is the standard "incompressible" Forchheimer Equation. This equation implies that the pressure gradient and density are known constants and not related through an equation of state. Thus, the pressure gradient must be constant giving

$$\frac{p_L - p_0}{L_r} + \frac{\mu_\alpha \varepsilon_\alpha}{K} u_\alpha + \rho_\alpha {u_\alpha}^2 \frac{{\varepsilon_\alpha}^2 c_f}{K^{1/2}} sign[u_\alpha] = 0 \tag{2-103}$$

The pressure at the outlet can be solved in terms of the inlet pressure and mass flow rate giving

$$p_L = \sqrt{{p_0}^2 - L_r 2RT\left(\frac{\mu_\alpha \varepsilon_\alpha \dot{m}}{K A_f} + \frac{\dot{m}^2 \varepsilon_\alpha c_f}{{A_f}^2 K^{1/2}}\right)}. \tag{2-104}$$

These three models are compared in Chapter 5. The compressible model and the incompressible model differ by 31% in predicting friction factor. The effect of the advective acceleration term is shown to be negligible in predicting friction factor.

2.6 Scale Analysis

A non-traditional scale analysis method is adopted for scaling the partial differential system of equations. Since a partial differential equation relates the change of a variable in more than one dimension, it is sensible to expect that there are separate scales for each dimension. Thus, separate temporal and spatial scales are used.

2.6.1 Conservation of Mass Equation Scale Analysis

The scale analysis begins by scaling the continuity equation. By choosing independent temporal and spatial scales for density and mass flux, the scaled continuity equation is written as

$$\frac{\partial \rho}{\partial t} + \left[\frac{\overline{m}}{L_s} \frac{t_s}{\widetilde{\rho}} \right] \frac{\partial m}{\partial x} = 0 \qquad \textbf{(2-105)}$$

where the tilde overbar represents the temporal scale and the dash overbar represents the spatial scale. Arbitrary length and time scales, L_s and t_s, have been used. The result of this scaling is the single balance

$$t_s \sim \frac{\widetilde{\rho} L_s}{\overline{m}} . \qquad \textbf{(2-106)}$$

The scaled continuity equation then reduces to the familiar form

$$\frac{\partial \rho}{\partial t} + \frac{\partial m}{\partial x} = 0 . \qquad \textbf{(2-107)}$$

2.6.2 Balance of Momentum Equation Scale Analysis

Next, the momentum equation is similarly scaled to give

$$\frac{\partial m}{\partial t} + \left[\frac{\widetilde{\rho}}{\overline{\rho}} \frac{\overline{m}}{\widetilde{m}} \right] \frac{\partial}{\partial x} \left(\frac{m^2}{\rho} \right) + \left[\frac{\widetilde{\rho p}}{\widetilde{m} \overline{m}} \right] \frac{\partial p}{\partial x} + \left[\frac{\widetilde{\rho}}{\overline{\rho}} \frac{\widetilde{m}}{\overline{m}} \frac{L_s}{\sqrt{K}} \right] \frac{m^2 sign[m]}{\rho} f = 0 . \qquad \textbf{(2-108)}$$

where the friction factor and the Reynolds number are, respectively

$$f = \frac{\varepsilon}{\mathrm{Re}_K} + \varepsilon^2 c_f \qquad \textbf{(2-109)}$$

and

$$\mathrm{Re}_K = \frac{\left|m^*\right|\sqrt{K}}{\mu^*}. \qquad \textbf{(2-110)}$$

where the asterisks denote dimensional quantities. The length scale in the Reynolds number is the square root of the permeability, not the macroscopic length scale, L_s. The macroscopic length scale represents the length scale of the macroscopic flow while the permeability length scale represents the length scale of the microscopic flow which is what drives the Darcy and Forchheimer effects. The fact that two length scales have been defined is evident since the volume averaging method requires such a result. The two length scales are necessary to model a porous media as a continuum where the macroscopic and microscopic effects are united. The basic assumption of the volume averaging method is that the macroscopic length scale is orders of magnitude larger than the microscopic length scale. Thus, it is necessary to define these two length scales, and it is expected that the model will eventually depend on two length scales.

This scaling leads to two balances. The first balance is proposed for the temporal and spatial acceleration terms, which gives

$$\frac{\overline{m}}{\widetilde{m}} \sim \frac{\overline{\rho}}{\widetilde{\rho}}. \qquad \textbf{(2-111)}$$

The remaining balance between the pressure gradient and the friction terms results in

$$\overline{p} \sim \frac{\widetilde{m}^2}{\overline{\rho}} \frac{L_s}{\sqrt{K}}. \qquad \textbf{(2-112)}$$

These two scales lead to the scaled momentum equation,

$$\frac{\partial m}{\partial t}+\frac{\partial}{\partial x}\left(\frac{m^2}{\rho}\right)+\Gamma_1\left[\frac{\partial p}{\partial x}+\frac{m^2 sign[m]}{\rho}f\right]=0\,, \tag{2-113}$$

which is characterized by a leading order dimensionless parameter,

$$\Gamma_1=\left(\frac{\tilde{\rho}}{\bar{\rho}}\right)^2\frac{L_s}{\sqrt{K}}\,. \tag{2-114}$$

Since this parameter is much larger than the remaining acceleration terms, which are O(1) in this form, it is tempting to consider dropping the acceleration terms. This results in an algebraic equation for the velocity given the pressure field.

2.6.3 α-Phase Conservation of Energy Equation Scale Analysis

Using an additional scale for the interfacial temperature difference, $\hat{T}$, the scaled gas energy equation is

$$\left[\frac{\tilde{E}\bar{m}}{\tilde{\rho}L_s}\right]\frac{\partial E}{\partial t}+\left[\frac{\bar{m}\bar{h}}{L_s}\right]\frac{\partial}{\partial x}(mh)-\left[\frac{k_s\bar{T}}{L_s^{\,2}}\right]\frac{\partial}{\partial x}\left(N_k k\frac{\partial T}{\partial x}\right)-\left[a_v H_s\hat{T}\right]H\left(T_\beta-T\right)=0 \tag{2-115}$$

which can be reduced to

$$\begin{aligned}&\frac{\partial E}{\partial t}+\left[\frac{c_{ps}\bar{T}}{c_{vs}\tilde{T}}\right]\frac{\partial}{\partial x}(mh)-\left[\frac{c_{ps}\bar{T}}{c_{vs}\tilde{T}}\frac{\sqrt{K}}{L_s}\frac{k_s}{\bar{m}c_{ps}\sqrt{K}}\right]\frac{\partial}{\partial x}\left(N_k k\frac{\partial T}{\partial x}\right)\\&-\left[\frac{c_{ps}\hat{T}}{c_{vs}\tilde{T}}4\frac{L_s}{\sqrt{K}}\frac{H_s}{\bar{m}c_{ps}}\right]H\left(T_\beta-T\right)=0\end{aligned} \tag{2-116}$$

if

$$\widetilde{E} = \widetilde{\rho} c_{vs} \widetilde{T}\,, \tag{2-117}$$

$$\overline{h} = c_{ps} \overline{T}\,, \tag{2-118}$$

and

$$\gamma = \frac{c_{ps}}{c_{vs}}. \tag{2-119}$$

By defining the reference Peclet number and the reference Stanton number respectively as

$$Pe = \frac{\overline{m} c_{ps} \sqrt{K}}{k_s} \tag{2-120}$$

and

$$St = \frac{H_s}{c_{ps} \overline{m}}, \tag{2-121}$$

and the surface area per unit volume as

$$a_v = \frac{4}{\sqrt{K}}, \tag{2-122}$$

the gas energy equation becomes

$$\frac{\partial E}{\partial t} + \left[\gamma \frac{\overline{T}}{\widetilde{T}} \right] \frac{\partial}{\partial x}(mh) - \left[\gamma \frac{\overline{T}}{\widetilde{T}} \frac{\sqrt{K}}{L_s} \frac{1}{Pe} \right] \frac{\partial}{\partial x}\left(N_k k \frac{\partial T}{\partial x} \right) - \left[\gamma \frac{\hat{T}}{\widetilde{T}} 4 \frac{L_s}{\sqrt{K}} St \right] H(T_\beta - T) = 0. \tag{2-123}$$

The proper balance is between the interfacial heat transfer term and the enthalpy advection term which gives

$$St \sim \frac{\overline{T}}{\hat{T}} \frac{1}{4} \frac{\sqrt{K}}{L_s}. \tag{2-124}$$

This leads to the final scaled gas energy equation,

$$\frac{\partial E}{\partial t}+\Gamma_2\left[\frac{\partial}{\partial x}\left(mh-\varepsilon_1 N_k k\frac{\partial T}{\partial x}\right)-H\left(T_\beta-T\right)\right]=0 \tag{2-125}$$

which is characterized by an additional leading order dimensionless parameter,

$$\Gamma_2=\gamma\frac{\overline{T}}{\widetilde{\overline{T}}} \tag{2-126}$$

and a second order dimensionless parameter

$$\varepsilon_1=\frac{\sqrt{K}}{L_s}\frac{1}{Pe}. \tag{2-127}$$

The last parameter, which characterizes the diffusive flux, is very small in comparison to the first parameter. This indicates that the gas energy equation is dominated be advection and interfacial heat transfer.

2.6.4 β-Phase Conservation of Energy Equation Scale Analysis

The matrix energy equation can be scaled to produce

$$\begin{aligned}&\left(\rho c\right)_\beta\frac{\partial T_\beta}{\partial t}-\left[\frac{\widetilde{\rho}c_{vs}}{\left(\rho c\right)_{\beta s}}\frac{\overline{T}}{\widetilde{\overline{T}}}\frac{k_{\beta s}}{k_s}\gamma\frac{\sqrt{K}}{L_s}\frac{1}{Pe}\right]\frac{\partial}{\partial x}\left[k_\beta\tau_\beta\frac{\partial T_\beta}{\partial x}\right]\\&+\left[\frac{\varepsilon}{1-\varepsilon}\frac{\widetilde{\rho}c_{vs}}{\left(\rho c\right)_{\beta s}}\gamma 4\frac{L_s}{\sqrt{K}}\frac{\hat{T}}{\widetilde{\overline{T}}}St\right]H\left(T_\beta-T\right)=0.\end{aligned} \tag{2-128}$$

There is only one relevant balance with this scaling, which is between the interfacial heat transfer term and the accumulation term. This is represented by the balance

$$\frac{\overline{T}}{\widetilde{\overline{T}}}\sim\frac{1}{\gamma}\frac{1-\varepsilon}{\varepsilon}\frac{\left(\rho c\right)_{\beta s}}{\widetilde{\rho}c_{vs}}. \tag{2-129}$$

Using this balance, the matrix energy equation can be written in its final form,

$$(\rho c)_\beta \frac{\partial T_\beta}{\partial t} - \varepsilon_2 \frac{\partial}{\partial x}\left[k_\beta \tau_\beta \frac{\partial T_\beta}{\partial x}\right] + H(T_\beta - T) = 0\,, \tag{2-130}$$

which is characterized by an additional second order dimensionless parameter,

$$\varepsilon_2 = \frac{1-\varepsilon}{\varepsilon}\frac{k_{\beta s}}{k_s}\frac{\sqrt{K}}{L_s}\frac{1}{Pe}. \tag{2-131}$$

Again, this parameter is much smaller than the other terms which are O(1) which illustrates that the interfacial heat transfer and accumulation dominate over the diffusive flux.

2.6.5 Scaled Equation Summary

The scaled equations are:

$$\frac{\partial \rho}{\partial t} + \frac{\partial m}{\partial x} = 0 \tag{2-132}$$

$$\frac{\partial m}{\partial t} + \frac{\partial}{\partial x}\left(\frac{m^2}{\rho}\right) + \Gamma_1\left[\frac{\partial p}{\partial x} + \frac{m^2 sign[m]}{\rho} f\right] = 0 \tag{2-133}$$

$$\frac{\partial E}{\partial t} + \Gamma_2\left[\frac{\partial}{\partial x}\left(mh - \varepsilon_1 N_k k \frac{\partial T}{\partial x}\right) - H(T_\beta - T)\right] = 0 \tag{2-134}$$

$$(\rho c)_\beta \frac{\partial T_\beta}{\partial t} - \varepsilon_2 \frac{\partial}{\partial x}\left[k_\beta \tau_\beta \frac{\partial T_\beta}{\partial x}\right] + H(T_\beta - T) = 0 \tag{2-135}$$

which are characterized by four dimensionless parameters resulting from the scaling balances. The boundary conditions provide the remaining information to complete the scale analysis. The time scale can be chosen as the angular frequency of the mass flow rate as

$$t_s = \frac{1}{\omega}. \tag{2-136}$$

The temporal mass flux scale can be chosen based on the boundary mass flux amplitudes as

$$\widetilde{m} = \frac{m_h + m_c}{2}. \tag{2-137}$$

The spatial mass flux scale can be expressed by assuming that the amplitude and phase varies linearly across the 1-D domain. Then, the RMS value of the gradient is

$$\overline{m} = \sqrt{\frac{m_h{}^2 + m_c{}^2 - 2m_h m_c \cos\left(\phi_{mc} - \phi_{mh}\right)}{2}}. \tag{2-138}$$

The spatial temperature scale can be expressed as

$$\overline{T} = T_h - T_c \tag{2-139}$$

which then leads to the spatial scale for density;

$$\overline{\rho} = \frac{p_b\left(T_h - T_c\right)}{RT_hT_c}. \tag{2-140}$$

The five scales can now be simplified to

$$L_s = \frac{1}{\omega\overline{\rho}}\frac{\overline{m}^2}{\widetilde{m}}, \tag{2-141}$$

$$\widetilde{\rho} = \overline{\rho}\frac{\widetilde{m}}{\overline{m}}, \tag{2-142}$$

$$\widetilde{T} = \frac{p_b\left(T_h - T_c\right)^2}{RT_hT_c}\frac{\widetilde{m}}{\overline{m}}\gamma\frac{\varepsilon}{1-\varepsilon}\frac{c_{vs}}{\left(\rho c\right)_{\beta s}}, \tag{2-143}$$

$$\overline{p} = \frac{\widetilde{m}^3}{\widetilde{\rho}^2} \frac{1}{\omega\sqrt{K}}, \tag{2-144}$$

and

$$\hat{T} = \frac{RT_h T_c}{p_b} \frac{\omega\sqrt{K}}{4St} \frac{\widetilde{m}}{\overline{m}^2}. \tag{2-145}$$

The importance of this scaling is that it has produced expressions which give insight into the amplitude of the temperature oscillation as well as the temperature difference between the matrix and gas. These amplitudes are seen to depend on the boundary conditions.

Finally, the dimensionless parameters can be written in terms of known quantities as

$$\Gamma_1 = \frac{\widetilde{m}}{\omega\sqrt{K}\overline{\rho}} \tag{2-146}$$

$$\Gamma_2 = \frac{1-\varepsilon}{\varepsilon} \frac{\overline{m}}{\widetilde{m}} \frac{(\rho c)_{\beta s}}{\overline{\rho} c_{vs}} \tag{2-147}$$

$$\varepsilon_1 = \sqrt{K}\omega \frac{\widetilde{\rho}}{\overline{m}} \frac{1}{Pe} \tag{2-148}$$

$$\varepsilon_2 = \frac{1-\varepsilon}{\varepsilon} \frac{k_{\beta s}}{k_s} \varepsilon_1 \tag{2-149}$$

Table 1 summarizes the numerical results of the scale analysis for a representative regenerator.

Table 1-Summary of scale analysis

F	40	[Hz]	A_f	5.969E-05	[m^2]
L_r	7.30E-02	[m]	w	251	[rad/s]
D_r	0.01048	[m]	R	2078	[Pa-m^3/kg-K]
E	0.6920	[-]	c_{ps}	5190	[J/kg-K]
K	1.005E-10	[m^2]	c_{vs}	3112	[J/kg-K]
m_h	19.58	[kg/s]	γ	1.67	[-]
m_c	29.62	[kg/s]	$(\rho c)_{ms}$	3.5E+06	[J/m^3-K]
φ_{mh}	0	[rad]	k_b	12.5605	[W/m-K]
φ_{mc}	-1.62	[rad]	k	0.1146	[W/m-K]
$\overline{T}_h$	300	[K]			
$\overline{T}_c$	70	[K]			
p_b	3.40E+06	[Pa]			
t_s	0.0040	[s]	H_s	35482	[W/m^2-K]
L_s	5.92E-03	[m]	St	2.67E-01	[-]
$\widetilde{\rho}$	17.21	[Kg/m^3]	Pe	12	[-]
$\overline{\rho}$	17.92	[Kg/m^3]	N_k	7.41	[-]
$\widetilde{m}$	24.60	[kg/s]			
$\overline{m}$	25.6	[kg/s]			
$\overline{p}$	2.00E+04	[Pa]			
$\widetilde{E}$	707388	[J/m^3]	Γ_1	545	[-]
$\widetilde{T}$	13.21	[K]	Γ_2	29.0	[-]
$\overline{T}$	230	[K]	ε_1	1.46E-04	[-]
$\hat{T}$	1.14E-03	[K]	ε_2	7.10E-03	[-]

2.6.6 Limiting Cases

For the parameters chosen, the dimensionless parameters satisfy the assumptions imposed on the problem, i.e.

$$\Gamma_1 >> 1 \quad \textbf{(2-150)}$$

$$\Gamma_2 >> \varepsilon_1 \quad \textbf{(2-151)}$$

$$\varepsilon_1 << 1 \quad \textbf{(2-152)}$$

$$\varepsilon_2 << 1 \quad \textbf{(2-153)}$$

There are several limiting cases of interest when these assumptions break down. For example, and the frequency approaches zero, it is expected that the upstream influence of the temperature will have an important effect.

CHAPTER 3

3. COMPUTATIONAL MODELS

3.1 Problem Definition

The problem to be solved, as defined in Chapter 2, is the unsteady, periodic, one-dimensional regenerator problem. The geometry is a cylindrical domain. Figure 6 illustrates the computational domain.

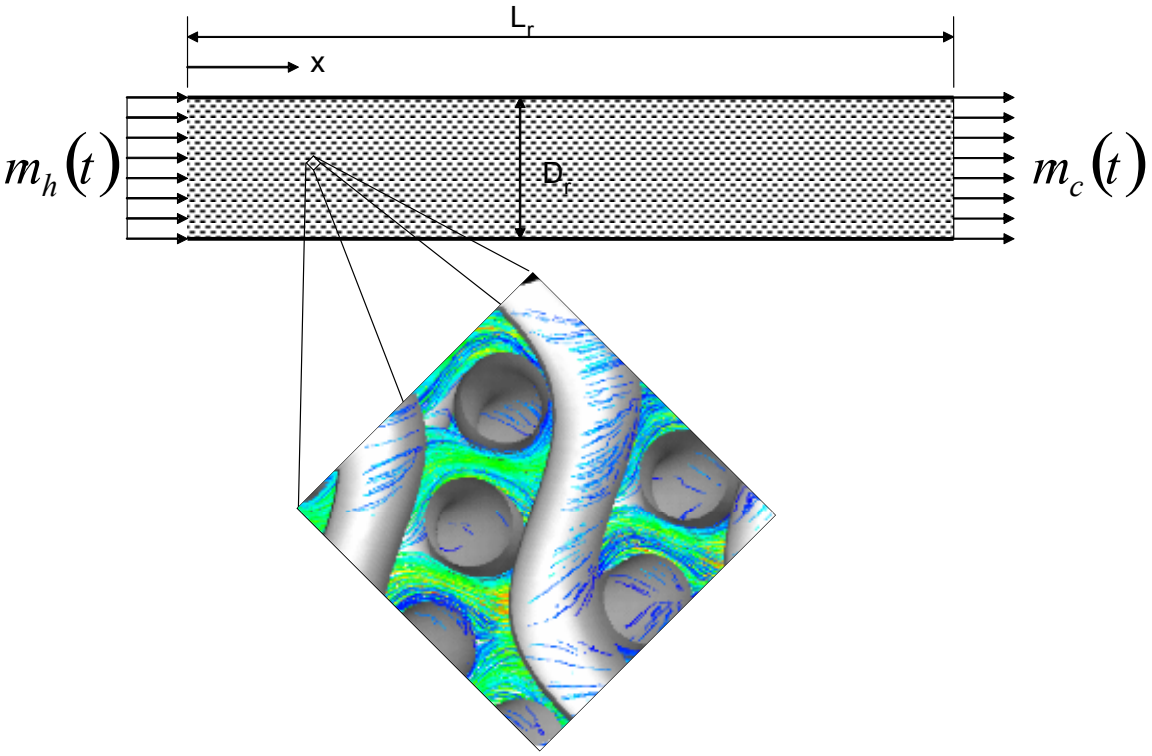

Figure 6 – Regenerator computational domain diagram

The solutions which are desired are the quasi-steady solutions, i.e. the solutions are identical from one cycle to the next. To accomplish this solution, a numerical method was employed to approximate the solutions. The details of the temporal and spatial representation are discussed in the following sections. This is followed by a discussion of a unique technique which was developed to artificially advance the solution in time to the quasi-steady solution. This technique relies on the proper specification of boundary conditions which is discussed below. Several asymptotic models are then developed which illustrate the mechanisms which contribute to a net energy transport in the regenerator.

3.2 Numerical Method

The numerical solution of partial differential equations (PDEs) is a broad field. Typical solution techniques in Computational Fluid Dynamics involve temporal and spatial discretization. A unique method of solving PDEs is a semi-analytical technique call the Method Of Lines (MOL.) MOL is a general technique in which all but one domain of a multi-domain system of PDEs is discretized (50, 51, 52, and 53). The remaining domain remains analytical, thus the meaning of semi-analytical. The result of this discretization is a system of ordinary differential equations (ODEs.) In physical systems, this usually involves discretizing the spatial domain, which can be multidimensional. At this level, all MOL approaches are identical. To proceed, the analyst must choose a unique method of time integration as well as spatial discretization.

3.2.1 Time Integration

Time integration can in general be an analytical technique or a numerical technique. Numerical techniques are generally classified as implicit and explicit. For hyperbolic systems, implicit time integration is necessary for stability. MatLab was used as the platform for solving the equations. The implicit ODE integrator, ODE15S, was found to be the most stable and efficient. ODE15S is a variable order solver which can use numerical differentiation formulas (NDFs) or backward differentiation formulas (BDFs.) The BDF formulas are commonly known as Gear's method and they suffer from lower efficiency. ODE15S is especially efficient in solving stiff systems (54).

3.2.2 Spatial Discretization

Several spatial discretization methods exist in the literature such as finite element, finite volume, finite difference, and collocation (55, 56, 57, 58, 59). Finite differences were used to solve the regenerator equations. Experimentation indicated that first order accurate central finite differences were the most stable and efficient if the equations were formulated in strong conservation form. Five point central differences yield fourth order accuracy, but this produces a larger banding in the Jacobian leading to reduced stability in the time integrator. Seven point differences were too unstable to use at all. Upwind differences did not appear to be as stable as central differences. As will be shown later in the discussion of boundary conditions, the continuity equation reduces to a second order equation in density in the limit of explicit velocity formulation. In this context, it would be understandable that central differences would yield the most stable scheme. To

calculate second derivatives, first order central differences using a three point stencil were used recursively. Appendix 2 contains a detailed discussion of the derivation of difference operators and their use with MatLab. For the equation set defined by Equations (2-79) – (2-82), the MOL discretized equations are

$$\frac{\partial \rho_{x_i}^t}{\partial t} = -D_{ij} m_{x_j}^t \ , \tag{3-1}$$

$$\frac{\partial m_{x_i}^t}{\partial t} = -D_{ij}\left(\frac{\left(m_{x_j}^t\right)^2}{\rho_{x_j}^t} + p_{x_j}^t \right) - \frac{\mu_{x_i}^t \varepsilon}{K} \frac{m_{x_i}^t}{\rho_{x_i}^t} - \frac{\left(m_{x_i}^t\right)^2}{\rho_{x_i}^t} \frac{\varepsilon^2 c_f}{K^{1/2}} sign\left[m_{x_i}^t\right], \tag{3-2}$$

$$\frac{\partial E_{x_i}^t}{\partial t} = -D_{ij}\left[m_{x_j}^t h_{x_j}^t - N_{k\,x_j}^{\ t} k_{x_j}^t \left(D_{jk} T_{x_k}^t\right)\right] + a_v H_{x_i}^t \left(T_{\beta\,x_i}^{\ t} - T_{x_i}^t\right), \tag{3-3}$$

and

$$\frac{\partial T_{\beta\,x_i}^{\ t}}{\partial t} = \frac{1}{\left(\rho c\right)_{\beta\,x_i}^{\ t}} \left\{ D_{ij}\left[k_{\beta\,x_j}^{\ t} \tau_\beta \left(D_{jk} T_{\beta\,x_k}^{\ t}\right)\right] - \frac{\varepsilon}{1-\varepsilon} a_v H_{x_i}^t \left(T_{\beta\,x_i}^{\ t} - T_{x_i}^t\right)\right\} \ . \tag{3-4}$$

for i=1..n where n is the number of spatial grid nodes. In these discretized equations, the central difference operator, D_{ij}, is an nxn square matrix. Equations (3-1) – (3-4) are now a coupled system of 4n ODEs which can be integrated in time from a set of 4n initial conditions.

3.3 Quasi-Steady Convergence via Cyclic Time Relaxation

Time integration begins with an initial condition for each of the solution variables. The equation set is integrated over a complete cycle. The solution at the final time step becomes the initial condition for the next period of integration. The integration

continues until the solution for two consecutive periods are equal. When this condition is met, the net change of internal energy of the system over a cycle is identically zero and the system is said to be in quasi-steady state. The regenerator system suffers from a long time constant with respect to the cycle period. As a result, the system of equations needs to be integrated for thousands of cycles until quasi-steady state is achieved unless the initial condition can be advanced artificially. Cyclic analysis of the governing equations provides an interesting and valuable technique called *cyclic time relaxation*. Cyclic averaging of the gas and matrix energy equations results in

$$\oint \left\{ \frac{\partial}{\partial z} \left[h_{ss} + q_{g,ss} + q_{m,ss} \right] \right\} dt = 0 \,, \tag{3-5}$$

where the "ss" subscript indicates steady state. Let

$$h_{ss} = \rho u c_p T_{ss},\; q_{g,ss} = -N_k k \frac{\partial T_{ss}}{\partial x},\; q_{m,ss} = -\frac{1-\varepsilon}{\varepsilon} k_\beta \tau_\beta \frac{\partial T_{\beta,ss}}{\partial x}. \tag{3-6}$$

A simplification in terms of temperature gives

$$\oint \left\{ \frac{\partial}{\partial x} \left[\rho u c_p T_{ss} - N_k k \frac{\partial T_{ss}}{\partial x} - \frac{1-\varepsilon}{\varepsilon} k_\beta \tau_\beta \frac{\partial T_{\beta,ss}}{\partial x} \right] \right\} dt = 0. \tag{3-7}$$

The temperature field at the end of a cycle may not satisfy this relationship. In this case, this relation provides a means of calculating a correction for the initial condition of the following cycle. By defining the quasi steady-state temperature fields which satisfy Equation (3-7) exactly as

$$T_{ss} = T'(x) + T(x,t),\ T_{\beta,ss} = T'(x) + T_\beta(x,t)\,, \tag{3-8}$$

where the primed temperature is an axial correction. T(x,t) and T_β(x,t) are the temperatures of the gas and matrix, respectively, from the current cycle. These quantities can be substituted into Equation (3-7) and T'(z) can be solved to obtain

$$f_1(z)\frac{\partial^2 T'}{\partial z^2} + f_2(z)\frac{\partial T'}{\partial z} + f_3(z) = 0\,, \tag{3-9}$$

where

$$\begin{aligned} f_1(x) &= -\oint\left\{N_k k + \frac{1-\varepsilon}{\varepsilon}k_\beta\tau_\beta\right\}dt \\ f_2(x) &= \oint\{\rho u c_p\}dt \\ f_3(x) &= \oint\left\{\frac{\partial}{\partial x}\left[\rho u c_p T - N_k k\frac{\partial T}{\partial x} - \frac{1-\varepsilon}{\varepsilon}k_\beta\tau_\beta\frac{\partial T_\beta}{\partial x}\right]\right\}dt \end{aligned} \tag{3-10}$$

For the case of constant specific heat,

$$f_2(x) = c_p\oint\{\rho u\}dt = 0 \tag{3-11}$$

which follows from a cyclic-average of the continuity equation. Equation (3-9) is a second order ODE which can be solved for the temperature correction function. The boundary conditions are appropriately chosen as

$$\begin{aligned} T'(0) &= 0 \\ T'(L_r) &= 0\,, \end{aligned} \tag{3-12}$$

since the temperature field at the ends does not need a correction due to the boundary conditions which fix those values. T' can then be solved numerically with a finite difference technique. Then the initial condition for the temperatures for the next period is

$$T(0,x) = T(\tau,x) + \lambda T'(x)$$
$$T_\beta(0,x) = T_\beta(\tau,x) + \lambda T'(x). \qquad \textbf{(3-13)}$$

A relaxation factor, λ, is used to aid stability. Experimentation has indicated an optimum value of 0.30-0.35.

3.4 Boundary and Initial Conditions

Equations (2-79) - (2-82), in their present form, are a mixed system of first and second order (spatially) partial differential equations. The continuity and momentum equations are both first order spatially while the energy equations are both second order. These equations in strict mathematical terms require six boundary conditions for the problem to be well-posed.

Two boundary conditions are required by the continuity and momentum equations. Stable solutions are found by imposing pressure at both ends or mass flux at both ends. Mass flux boundary conditions are chosen such that zero net mass flux can be achieved. Boundary conditions are needed at both ends for stability and this can be understood by considering the limiting case when the acceleration terms in the momentum equation are neglected. This results in the explicit equation for velocity,

$$\frac{\partial p}{\partial x} + \frac{\mu_\alpha \varepsilon_\alpha}{k} u + \rho u^2 \frac{\varepsilon_\alpha^{\,2} c_f}{k^{1/2}} sign[u] = 0. \qquad \textbf{(3-14)}$$

It is then clear that velocity is a function of the pressure gradient, which, in turn, is a function of the density gradient and temperature gradient. When the velocity in the continuity equation is eliminated in terms of temperature and density, the result is a spatially second order continuity equation,

$$\frac{\partial \rho}{\partial t} + \frac{\partial}{\partial x}\left(\rho f\left(\frac{\partial \rho}{\partial x}, \frac{\partial T}{\partial x} \right) \right) = 0. \qquad \textbf{(3-15)}$$

In this limiting case, the continuity equation is diffusive. Thus, it seems natural to impose mass flux boundary conditions at both ends of the domain.

In actuality, the momentum equation is a spatially first order equation. The advective acceleration term which makes it first order is quite small and can be neglected producing a zeroth order momentum equation. Together with the first order continuity, only one boundary condition is required. Since two mass flow boundary conditions have already been specified, the problem is over-specified by one boundary condition at this point. The boundary condition requirements of the energy equations will absorb this over-specification.

Referring back to the scaled energy equations, the diffusion terms are characterized by a small dimensionless parameter. This indicates that there is the possibility for a thermal boundary layer at the ends of the regenerator. Numerical experiments suggest that resolving such a boundary layer does not have a significant impact on the regenerator solution since the temperature fluctuation in the regenerator is largely a result of the compression process. Outside of this boundary layer, the regenerator is largely unaffected by the incoming gas temperature. This motivates a simplified application of boundary conditions based on a leading order simplification of the energy equations.

Scaling and numerical experiments suggest that these second order diffusion terms are essentially steady, spatial sources, i.e. the temporal fluctuations are orders of

magnitude smaller than the spatial variations. This suggests that the boundary conditions that are required mathematically can be neglected with little effect on the solution. The gas energy equation is still first order due to the enthalpy advection term, but the matrix energy equation is zeroth order. As a result, the gas energy equation requires a single boundary condition while the matrix energy equation requires no boundary conditions.

To summarize, the solutions of interest can be found by neglecting the strict mathematical requirement of six boundary conditions. For the limiting problem, the equations consist of a first order continuity and gas energy and zeroth order momentum and matrix energy. Thus two boundary conditions are needed which satisfy the important corollary condition of zero net mass flux. The most satisfactory method of achieving this is by imposing harmonic mass flux boundary conditions, i.e.

$$\left(\rho u\right)_h = \frac{\dot{m}_h}{A_f}\cos\left(\omega t + \phi_{mh}\right) \qquad \textbf{(3-16)}$$

and

$$\left(\rho u\right)_c = \frac{\dot{m}_c}{A_f}\cos\left(\omega t - \phi_{mc}\right). \qquad \textbf{(3-17)}$$

These mass flux boundary conditions are actually boundary conditions for the momentum equation, not the continuity equation. Imposing mass conserving boundary conditions for the continuity equation is difficult since simple sinusoidal densities at the ends will not in general lead to mass conservation. If the entire cryocooler is modeled as a closed system, then density boundary conditions could be used.

Since the solution of interest is the quasi-steady solution, the proper initial condition is one that produces a quasi-steady solution after one cycle of simulation. This

is essentially the purpose of the artificial convergence technique discussed above. Additionally, this technique is responsible for producing a solution which has the desired mean pressure and mean warm and cold end temperatures. Thus, the converged solution satisfied seven boundary parameters;

$\dot{m}_h$ Warm end mass flow amplitude

$\dot{m}_h$ Cold end mass flow amplitude

$\phi_{mh} - \phi_{mc}$ Mass flow phase shift

ω Angular frequency

T_h Warm end mean temperature

T_c Cold end mean temperature

p_b Mean pressure

These parameters are in addition to the seven geometric and empirical parameters which define the shape of the regenerator and the pores;

L_r Regenerator length

D_r Regenerator diameter

ε Porosity

f Friction factor

Nu Nusselt number

N_k Dispersion coefficient

τ_β Matrix tortuosity

3.5 The Constant Temperature Model (CTM)

A variety of asymptotic models can be considered. Each asymptotic model provides insight into the mechanism of net energy transport in the regenerator. Two asymptotic cases are presented, beginning with the most restrictive and an intermediate model. Each model can be considered with real or ideal gas, and constant or variable properties, which provide additional permutations. Results of numeric computations with these models are presented in Chapter 5. There it is revealed that the regenerator net energy transport increases with each additional relaxation.

The simplest idealized regenerator is represented by the Constant Temperature Model (CTM.) This model assumes 1) that the heat transfer between the gas and the matrix is perfect and 2) that the matrix heat capacity is very large. The consequence of the first assumption is that there is an infinitesimal temperature difference between the gas and matrix. The consequence of the second assumption is that the temperature field is steady, i.e. there is no temperature oscillation, only a spatial temperature field. Mathematically, this requires that the temperature field be specified *a priori*. The matrix gas energy equation can be rearranged to give

$$-\frac{\partial}{\partial x}\left[k_\beta \tau_\beta \frac{\partial T_\beta}{\partial x}\right] = a_v H\left(T_\beta - T\right). \qquad \textbf{(3-18)}$$

which can then be inserted into the gas energy equation to give

$$\frac{\partial E}{\partial t} + \frac{\partial}{\partial x}\left(\rho u h - N_k k \frac{\partial T}{\partial x} - k_\beta \tau_\beta \frac{\partial T_\beta}{\partial x}\right) = 0. \qquad \textbf{(3-19)}$$

The cycle average of this equation is

$$\oint \frac{\partial}{\partial x}\left(\rho u h - N_k k \frac{\partial T}{\partial x} - k_\beta \tau_\beta \frac{\partial T_\beta}{\partial x} \right) dt = 0. \qquad \textbf{(3-20)}$$

Note that the cycle average of the time rate of change of the volumetric internal energy is identically zero for steady, periodic operation. For ideal gas with constant properties, this becomes

$$c_p T \oint \frac{\partial}{\partial x}(\rho u) dt + \oint \frac{\partial}{\partial x}\left(- N_k k \frac{\partial T}{\partial x} - k_\beta \tau_\beta \frac{\partial T_\beta}{\partial x} \right) dt = 0. \qquad \textbf{(3-21)}$$

The first integral, which is the net enthalpy flow, can be shown to be zero by cyclic integration of the continuity equation. This is the only condition under which the net enthalpy flow is zero. The diffusion fields drive the steady state temperature field for this case. Beginning with a linear temperature field, the cyclic time relaxation procedure is applied to advance the solution to steady state. If a real gas equation of state is used, then the net enthalpy flow is positive. This is obvious since the enthalpy is a function of temperature and density. The steady temperature field is then affected by the diffusion and net enthalpy flow fields. The regenerator loss due solely to the density dependence of the enthalpy can now be assessed.

This model is thermally perfect, but the effects of pressure drop and viscous dissipation are still captured via a coupled solution of the continuity and momentum equation, which remain unchanged. Thus, the system of equations being solved is

$$\frac{\partial \rho}{\partial t}+\frac{\partial m}{\partial x}=0 \tag{3-22}$$

$$\frac{\partial m}{\partial t}+\frac{\partial}{\partial x}\left(\frac{m^2}{\rho}\right)+\frac{\partial p}{\partial x}+\frac{\mu_\alpha \varepsilon}{k}\frac{m}{\rho}+\frac{m^2}{\rho}\frac{\varepsilon^2 c_f}{K^{1/2}}sign[m]=0 \tag{3-23}$$

This system of PDEs requires two mass flux boundary conditions, as defined previously in addition to initial conditions for density and mass flux. Cyclic time relaxation is applied to find a temperature field which yields a steady solution.

3.6 The Local Thermal Equilibrium Model (LTEM)

Local thermal equilibrium should not be confused with local thermodynamic equilibrium. In this model, the assumption of very large matrix heat capacity is relaxed while retaining the assumption of perfect gas-to-matrix heat transfer. The result is a single energy equation with a single temperature. This energy equation is formed by combining Equations (2-81) and (2-82) such that

$$\frac{\partial E}{\partial t}+(\rho c)_\beta \frac{1-\varepsilon}{\varepsilon}\frac{\partial T_\beta}{\partial t}+\frac{\partial}{\partial x}\left(\rho u h - N_k k \frac{\partial T}{\partial x}-\frac{1-\varepsilon}{\varepsilon}k_\beta \tau_\beta \frac{\partial T_\beta}{\partial x}\right)=0. \tag{3-24}$$

For ideal gas, this combined energy equation can be re-written as

$$e\frac{\partial \rho}{\partial t}+\rho c_v \frac{\partial T}{\partial t}+(\rho c)_\beta \frac{1-\varepsilon}{\varepsilon}\frac{\partial T_\beta}{\partial t}+\frac{\partial}{\partial x}\left(\rho u e + P u - N_k k \frac{\partial T}{\partial x}-\frac{1-\varepsilon}{\varepsilon}k_\beta \tau_\beta \frac{\partial T_\beta}{\partial x}\right)=0. \tag{3-25}$$

Using the fact that the temperatures of the gas and matrix are identical, the combined energy equation is now written as

$$\left[\rho c_v + (\rho c)_\beta \frac{1-\varepsilon}{\varepsilon}\right]\frac{\partial T}{\partial t} + e\left[\frac{\partial \rho}{\partial t} + \frac{\partial}{\partial x}(\rho u)\right] + \rho u c_v \frac{\partial T}{\partial x} + \frac{\partial}{\partial x}\left(Pu - N_k k \frac{\partial T}{\partial x} - \frac{1-\varepsilon}{\varepsilon} k_\beta \tau_\beta \frac{\partial T_\beta}{\partial x}\right) = 0. \quad \textbf{(3-26)}$$

Continuity can be used to eliminate the second term, and the final form of the LTE energy equation is

$$\frac{\partial T}{\partial t} + \frac{\rho u c_v}{C_{LTE}} \frac{\partial T}{\partial x} + \frac{1}{C_{LTE}} \frac{\partial}{\partial x}\left(Pu - N_k k \frac{\partial T}{\partial x} - \frac{1-\varepsilon}{\varepsilon} k_\beta \tau_\beta \frac{\partial T_\beta}{\partial x}\right) = 0. \quad \textbf{(3-27)}$$

where the combined volumetric heat capacity is defined as

$$C_{LTE} = \rho c_v + (\rho c)_\beta \frac{1-\varepsilon}{\varepsilon}. \quad \textbf{(3-28)}$$

Implementing an equivalent combined energy equation for a real gas is more difficult due to the additional density dependence of the gas internal energy. Expanding Equation (3-24) for a real gas gives

$$e\frac{\partial \rho}{\partial t} + \rho\left(\frac{\partial e}{\partial T}\right)_\rho \frac{\partial T}{\partial t} + \rho\left(\frac{\partial e}{\partial \rho}\right)_T \frac{\partial \rho}{\partial t} + (\rho c)_\beta \frac{1-\varepsilon}{\varepsilon}\frac{\partial T_\beta}{\partial t} + \frac{\partial}{\partial x}\left(\rho u h - N_k k \frac{\partial T}{\partial x} - \frac{1-\varepsilon}{\varepsilon} k_\beta \tau_\beta \frac{\partial T_\beta}{\partial x}\right) = 0 \quad \textbf{(3-29)}$$

which can be simplified to

$$\left[\rho\left(\frac{\partial e}{\partial T}\right)_\rho + (\rho c)_\beta \frac{1-\varepsilon}{\varepsilon}\right]\frac{\partial T}{\partial t} - \left[e + \rho\left(\frac{\partial e}{\partial \rho}\right)_T\right]\frac{\partial (\rho u)}{\partial x} + \frac{\partial}{\partial x}\left(\rho u h - N_k k \frac{\partial T}{\partial x} - \frac{1-\varepsilon}{\varepsilon} k_\beta \tau_\beta \frac{\partial T_\beta}{\partial x}\right) = 0. \quad \textbf{(3-30)}$$

This is well-posed mathematically. The additional complexities include the calculation of the partial derivatives of the internal energy. The boundary conditions using either

energy equation are the same; two mass flux BCs. Again, cyclic time relaxation is applied to find a temperature field which produces a steady solution.

3.7 Dual Energy Equation Model (DEEM)

The Dual Energy Equation model solves the complete equation set, repeated here as

$$\frac{\partial \rho}{\partial t} + \frac{\partial m}{\partial x} = 0 \qquad \textbf{(3-31)}$$

$$\frac{\partial m}{\partial t} + \frac{\partial}{\partial x}\left(\frac{m^2}{\rho} + p\right) + \frac{\mu\varepsilon}{K}\frac{m}{\rho} + \frac{m^2}{\rho}\frac{\varepsilon^2 c_f}{K^{1/2}} sign[m] = 0 \qquad \textbf{(3-32)}$$

$$\frac{\partial E}{\partial t} + \frac{\partial}{\partial x}\left(mh - N_k k \frac{\partial T}{\partial x}\right) - a_v H\left(T_\beta - T\right) = 0 \qquad \textbf{(3-33)}$$

$$\left(\rho c\right)_\beta \frac{\partial T_\beta}{\partial t} - \frac{\partial}{\partial x}\left[k_\beta \tau_\beta \frac{\partial T_\beta}{\partial x}\right] + \frac{\varepsilon}{1-\varepsilon} a_v H\left(T_\beta - T\right) = 0 \qquad \textbf{(3-34)}$$

This model captures the effects of finite heat transfer and matrix heat capacity as well as flow friction. The characterization of this model depends on several parameters which can be categorized.

Boundary mean temperatures: T_h and T_c

Mass flowrates: $\dot{m}_h$, $\dot{m}_c$, w, and $\phi_{mh} - \phi_{mc}$

Mean pressure: p_b

Macroscopic geometry: L_r and D_r

Additionally, the model depends on several correlations which are functions of the microscopic geometry and/or the flow field: N_k, τ_β, Nu, f, and ε.

3.8 Model Verification

The accuracy of the Dual Energy Equation model was verified by using a test solution in a method similar to Kirkconnell (60). The particular solution was chosen such that it retained the important characteristics of the actual solution. An arbitrary solution can be made to satisfy the system of equations if appropriate source terms are added to each equation, i.e.

$$\frac{\partial \rho}{\partial t} + \frac{\partial m}{\partial x} = F_1(t,x) \tag{3-35}$$

$$\frac{\partial m}{\partial t} + \frac{\partial}{\partial x}\left(\frac{m^2}{\rho} + p\right) + \frac{\mu\varepsilon}{K}\frac{m}{\rho} + \frac{m^2}{\rho}\frac{\varepsilon^2 c_f}{K^{1/2}} sign[m] = F_2(t,x) \tag{3-36}$$

$$\frac{\partial E}{\partial t} + \frac{\partial}{\partial x}\left(mh - N_k k \frac{\partial T}{\partial x}\right) - a_v H(T_\beta - T) = F_3(t,x) \tag{3-37}$$

$$(\rho c)_\beta \frac{\partial T_\beta}{\partial t} - \frac{\partial}{\partial x}\left[k_\beta \tau_\beta \frac{\partial T_\beta}{\partial x}\right] + \frac{\varepsilon}{1-\varepsilon} a_v H(T_\beta - T) = F_4(t,x). \tag{3-38}$$

The test solution was chosen as follows:

$$m = M_2 \cos(\omega t - M_3) \tag{3-39}$$

$$T = T_1 + T_2 \cos(\omega t - T_3) \tag{3-40}$$

$$P = p_b + P_2 \cos(\omega t - P_3) \tag{3-41}$$

$$\rho = \frac{P}{RT} \tag{3-42}$$

$$u = \frac{m}{\rho} \tag{3-43}$$

$$E = \rho c_v T \tag{3-44}$$

$$T_\beta = T \tag{3-45}$$

$$M_2 = m_h + \left(m_c - m_h\right)\frac{x}{L_r} \tag{3-46}$$

$$M_3 = \phi_{mh} + \left(\phi_{mc} - \phi_{mh}\right)\frac{x}{L_r} \tag{3-47}$$

$$T_1 = T_h + \left(T_c - T_h\right)\frac{x}{L_r} \tag{3-48}$$

$$T_2 = \widetilde{T}_h + \left(\widetilde{T}_c - \widetilde{T}_h\right)\frac{x}{L_r} \tag{3-49}$$

$$T_3 = M_3 - \frac{\pi}{2} \tag{3-50}$$

$$P_2 = \widetilde{P}_h + \left(\widetilde{P}_c - \widetilde{P}_h\right)\frac{x}{L_r} \tag{3-51}$$

$$P_3 = \phi_{Ph} + \left(\phi_{Pc} - \phi_{Ph}\right)\frac{z}{L_r} \tag{3-52}$$

All of the parameters in the preceding equations come from the boundary conditions with the exception of the boundary temperature and pressure oscillation amplitudes, $\widetilde{T}_h, \widetilde{T}_c, \widetilde{P}_h, \widetilde{P}_c$, and the pressure phase angles, ϕ_{Ph} and ϕ_{Pc}. These parameters are chosen from a representative numerical solution. Equation (3-50) was chosen such that the net enthalpy flux would be identically zero. Alternatively, a condition could be constructed to produce a constant, non-zero net enthalpy flux. The zero enthalpy flux case was chosen for simplicity. Adding a non-zero enthalpy flux will produce a similar solution with a shift in the net enthalpy field. The source terms, F_i, were then analytically solved.

The numerical solution was then calculated using the exact numerical method detailed above. Since the initial condition can be set using the known exact solution, the model converges in one cycle.

The model numerically solves the test equations to very high accuracy as illustrated in Figure 8-Figure 14. The net enthalpy flux is visually identically zero. There is less that 0.2 mW deviation. The solution fields show very small errors. The normalized errors are:

Density	5×10^{-7}
Mass flux	3×10^{-7}
Energy	4×10^{-7}
Matrix temperature	3×10^{-8}
Gas temperature	4×10^{-8}
Pressure	4×10^{-7}

The small normalized errors indicate that the numerical scheme is not introducing unrealistic errors into the solution and that the solver can solve similar equations. The source terms should not dramatically affect the character of the equations. Additionally, the question of the proper set of boundary conditions is answered. This solution was obtained using just two mass flux boundary conditions even though the strict mathematical requirement is six boundary conditions.

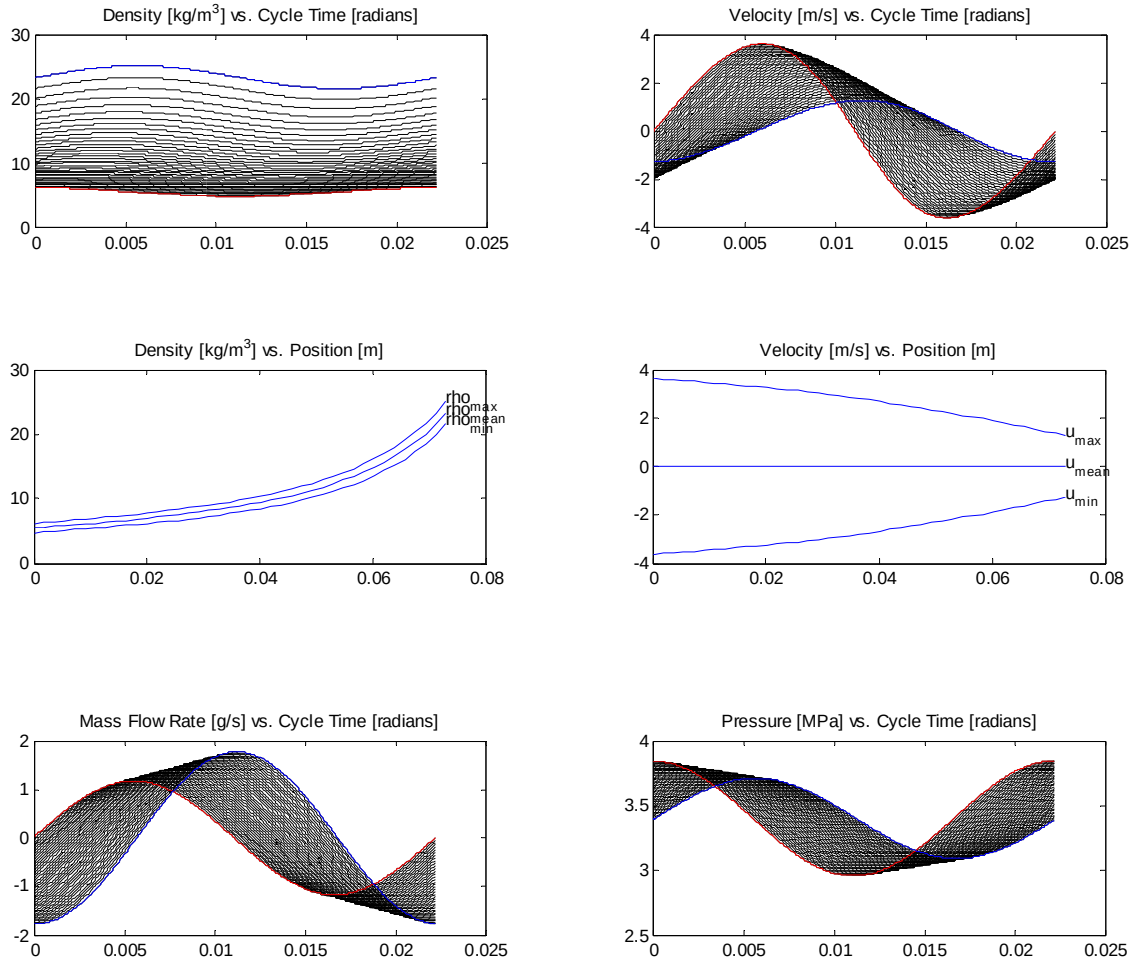

Figure 7 – Test case solution results.

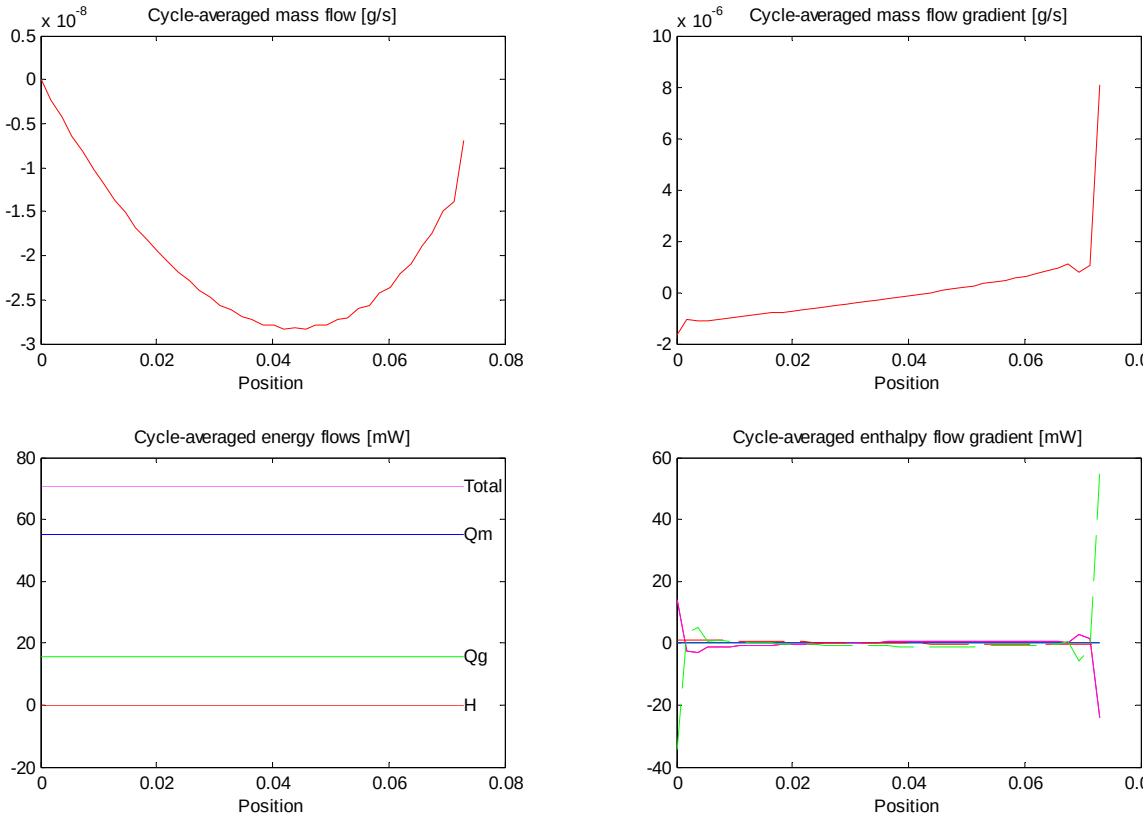

Figure 8 – The net enthalpy flux satisfies the test case to within visual accuracy (0.2 mW deviation)

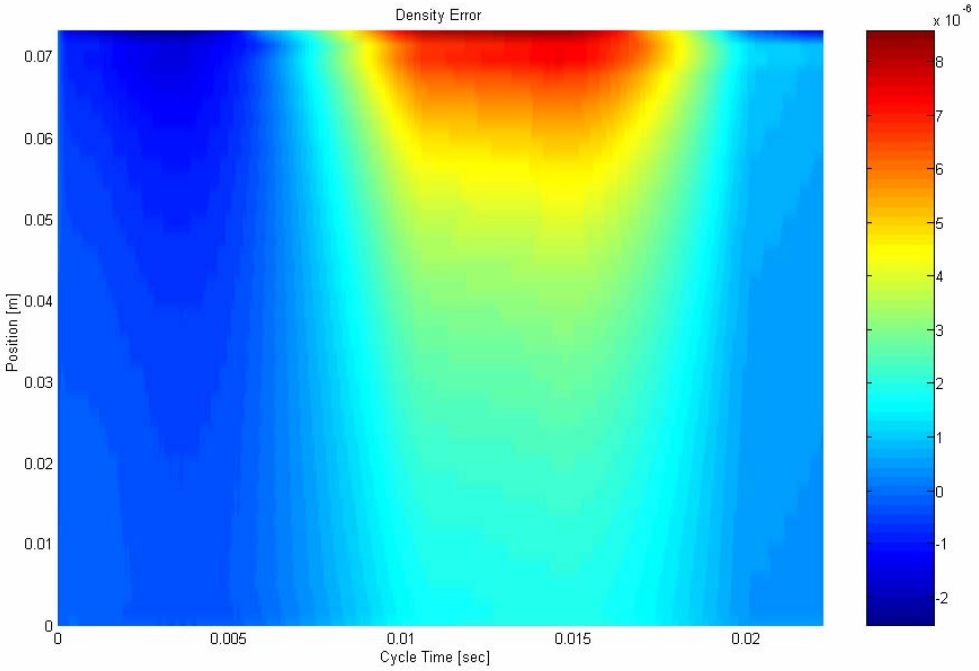

Figure 9 – Maximum density error $8x10^{-6}$ kg/m^3

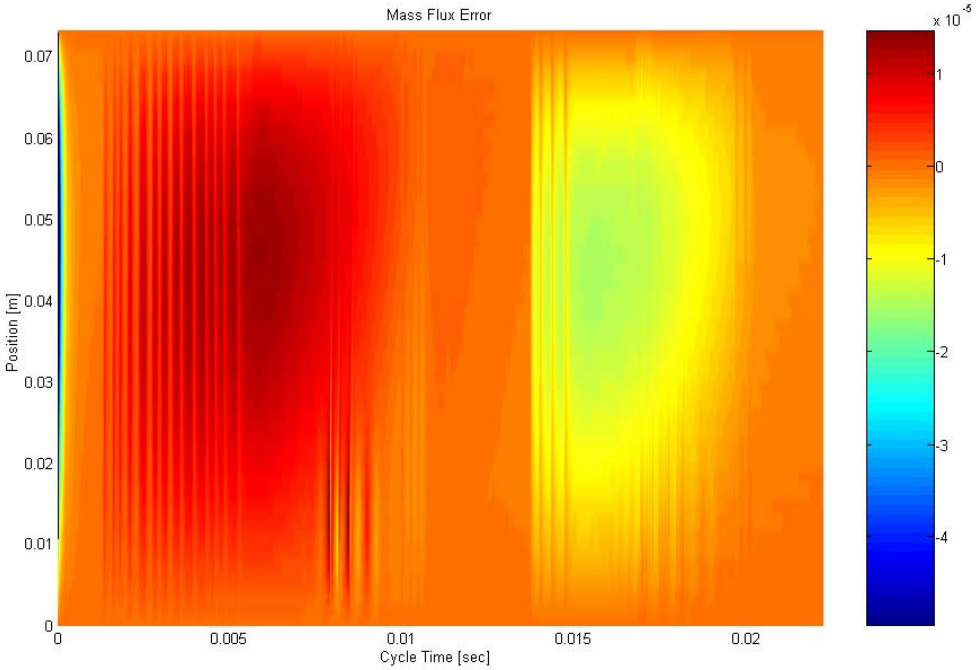

Figure 10 – Maximum mass flux error $1x10^{-5}$ kg/m^2-s

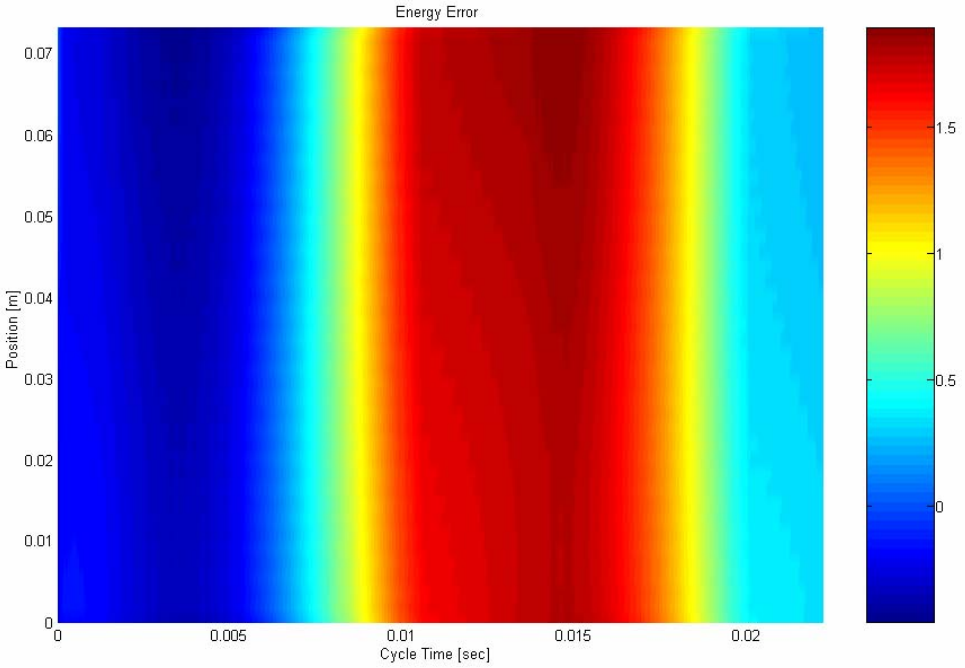

Figure 11 – Maximum energy error 2 kJ/m^3

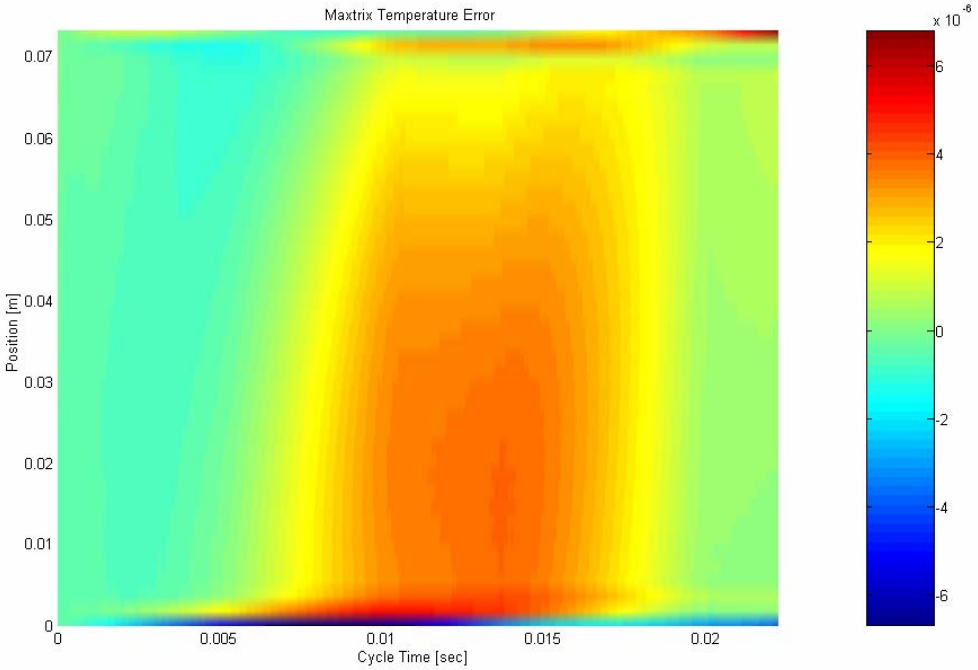

Figure 12 – Maximum matrix temperature error 6x10^{-6} K

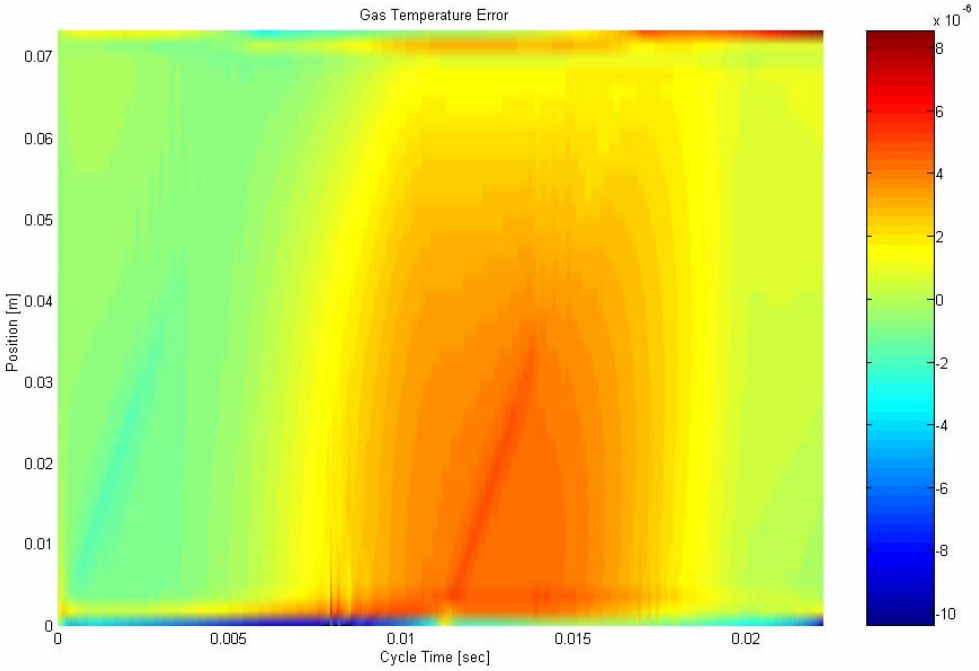

Figure 13 – Maximum gas temperature error $8x10^{-6}$ K

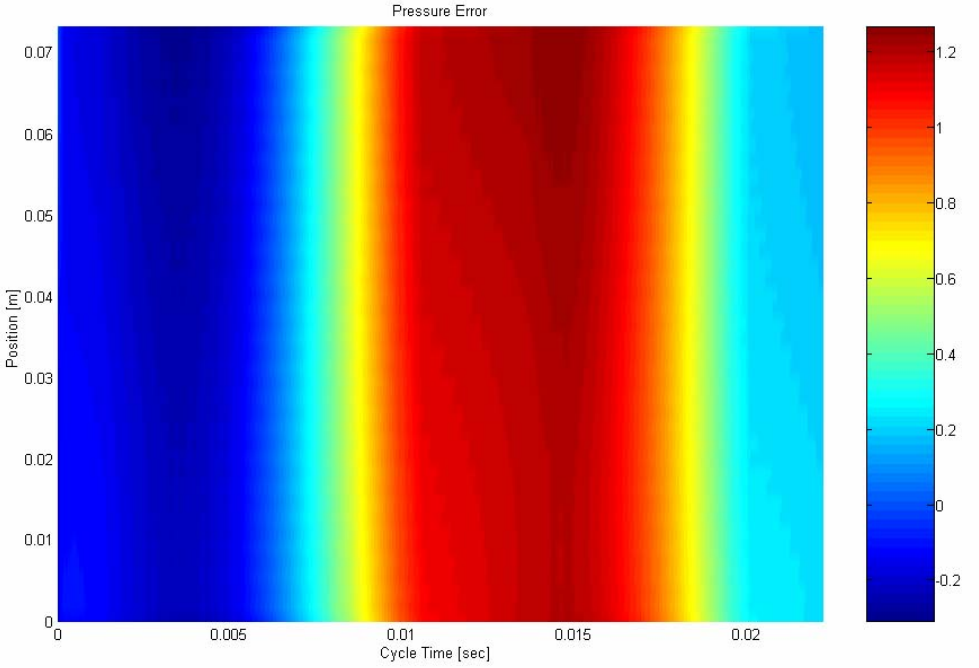

Figure 14 – Maximum pressure error 1.2 Pa

Before proceeding on to Chapters 4 and 5, it is worth reviewing what has been accomplished up to this point. A mathematical model for the regenerator was developed based on fundamental principles and guided by intuition. A numerical method was then developed using the Method of Lines with central finite differences. An artificial convergence technique was developed which dramatically improves convergence speed. To provide a comparison with the full model, two asymptotic models were developed. Chapter 4 describes the development of an experimental apparatus which was used to investigate this model. Chapter 5 presents the modeling results and compares these results to the experimental data from Chapter 4.

CHAPTER 4

4. EXPERIMENTAL APPARATUS AND MEASUREMENTS

4.1 Overview and Experimental Apparatus

The apparatus used is an Orifice Pulse Tube Cryocooler (OPTC) design and is illustrated in Figure 15. With the exception of the regenerator materials, the identical cooler assembly was used by Kirkconnell, et al. to characterize overall cryocooler performance as a function of pulse tube aspect ratio and volume (61). Towards that end, the apparatus was designed to accommodate five interchangeable regenerator/cold heat exchanger/pulse tube assemblies (Figure 16), hereafter referred to as "expanders." Using the numbering scheme of the previous paper, expanders 1 through 3 are of identical volume, and expanders 1, 4, and 5 are of constant length. The performance of the constant volume pulse tubes (1-3) were found to be virtually indistinguishable, hence the use of these three is ideal for the present effort in which the unique impact of regenerator design on performance is sought. An unfortunate oversight resulted in the testing of one of the regenerators in expander 5, which has a 17% larger pulse tube volume than the constant volume set and performed slightly better in the previous experiments (no load temperature of 76 K vs. 79 K). The differences between the performances of the various regenerators were much larger than this pulse tube volume effect, however, so the data from expander 5 are still considered relevant. The reader is referred to ref. 61 for additional details on the apparatus.

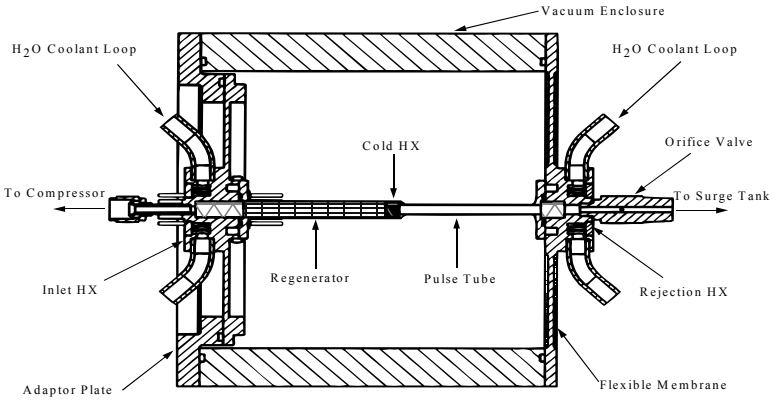

Figure 15 - Experimental Apparatus
Reproduced with authors' consent (61)

Figure 16 – Regenerator/Pulse Tube expander module. Regenerator is the larger diameter section.

Figure 17 shows the apparatus integrated with the vacuum system and data acquisition system. Figure 18 shows a close-up view of the compressor. The compressor used is a nominal 3 cc swept volume, dual opposed piston, Hughes Condor on loan from Night Vision & Electronic Sensors Directorate (NVESD).

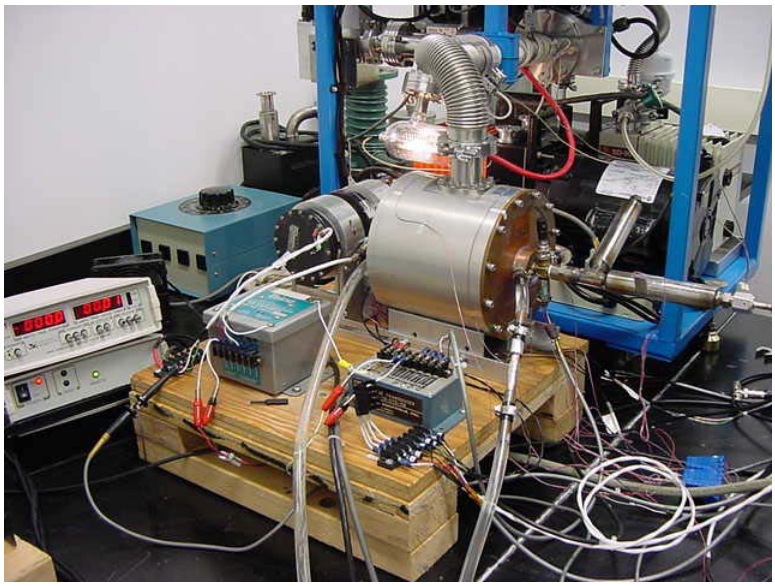

Figure 17 – Experimental apparatus with complete instrumentation.

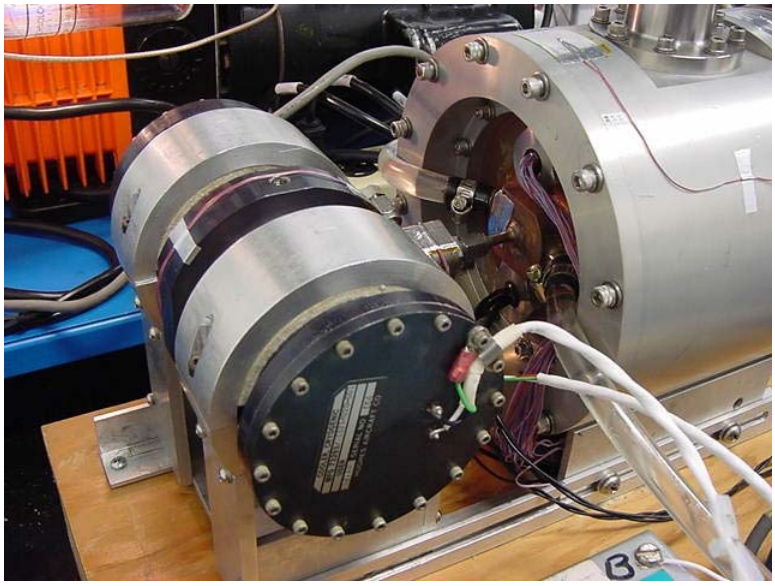

Figure 18 – Close-up view of the compressor.

The chamber surrounding the expander is evacuated using a turbomolecular vacuum pump, shown in Figure 19. This vacuum system is capable of achieving pressures as low as 2×10^{-6} torr. These pressures are necessary to eliminate convective and conductive heat

transfer through the surrounding gas. Typically, natural convection will occur at atmospheric pressures down a few torr. At these pressures, the heat carried by circulation currents is very small, but conduction will continue at levels comparable to atmospheric pressure. Around 10 torr, the conductivity of the low pressure gas will begin to decrease until it is essentially zero around 10^{-4} torr (62). At this pressure and lower, the only mode of heat transfer is radiation. Further reduction of the pressure is limited by slow moisture release from the chamber and MLI. MLI (multilayer insulation) is a material used as a radiation shield. It is composed of layers of aluminized mylar with woven Dacron spacer layers. Typically, it is recommended that a vacuum level of 10^{-6} torr be achieved and maintained before cooling a cryogenic system. At this pressure, the residual moisture is low enough that it will not form significant frost and alter the MLI performance.

Figure 19 – Turbo vacuum pump station.

Four regenerators were tested in a previous study (63, 64). They consisted of quite different geometry, but the same material. Since that report, an additional 45 micron regenerator and a diced foam metal regenerator were tested. All six regenerators are made of stainless steel fabricated into different forms of porous materials. The regenerators are summarized in Table 2 with their relevant data. The porosity of each regenerator was measured experimentally by measuring the total matrix mass. The density of the homogeneous material and the total regenerator volume can be used to calculate the matrix porosity.

Table 2 - Descriptive Summary of the Regenerators under Study

#	Name / Figure	Description
1	325 Mesh / Figure 20	Wire mesh screens - 325 wires per inch Wire diameter: 27.9 μm Measured Porosity: 0.696
2	400 Mesh / not shown	Wire mesh screens – 400 wires per inch Wire diameter: 25.4 μm Measured Porosity: 0.692
3	60 Micron / Figure 21 Alabama Cryogenic Engineering (65)	Perforated disks Pore size: 60 microns Measured Porosity: 0.717 (spacers)
4	45 Micron Alabama Cryogenic Engineering	Perforated disks Pore size: 45 microns Measured Porosity: 0.644 (no spacers)
5	Foam Metal / Figure 22	Sintered foam metal plug Measured Porosity: 0.614

In packing wire mesh screens, the actual porosity can vary by several percent based on the degree of nesting. For wire screens perfectly aligned, the porosity can approach 50%. For a sample of 30 400 mesh screens, the total thickness of the stack was measured at 1.536 mm. This gives an average screen thickness of 51.2 microns, or a half

thickness of 25.6 microns. The half thickness is very close to the nominal wire diameter suggesting that the screens were not nesting.

The 60 micron perforated disk thickness was measured at 211 microns. This results in a perforation aspect ratio of 3.5. The 45 micron disks have an aspect ratio of 4.7 and 7.1 for the 30 micron disks. As the aspect ratio increases, the flow begins to resemble that of a tube bundle.

The foam metal regenerator was fabricated from 100 micron particles which were sintered. The result is a rigid matrix with random pore geometry and variable pore size. The process is able to produce sintered matrices for a range of porosity. The process used to make the sintered foam metal is proprietary, but shrinkage of the matrix during sintering most likely requires beginning with a higher porosity. The target porosity of the foam metal regenerator was chosen such that it was in the same range as the wire mesh screens. The actual porosity was 8% less than the wire mesh regenerators. System level modeling suggests that the regenerator performance is sensitive to the matrix porosity. An 8% porosity difference may cause a significant performance change. The morphology of the pore and solid structure is not studied in this dissertation, but the other matrices have a much better understood geometry in terms of wire diameter and pitch or perforation diameter and aspect ratio. The performance test with the foam metal regenerator is the critical measure of the matrix performance. It is possible that sintered matrices can provide reasonable regenerator performance, especially for a low cost application where performance is not as critical.

The first three regenerators are composed of a stack of disks made from the particular material (Figure 20 and Figure 21). These disks are packed into the regenerator tube making sure that the disks are not bent. Each disk is then lightly tamped to assure that it is snugly packed into the tube. The fourth regenerator is drastically different from the others. This foam metal regenerator is a single plug of porous metal (Figure 22). This allows significant time savings in packing the regenerator. Whereas the single disk regenerators each take as much as eight hours to hand pack, the foam metal regenerator takes only a few minutes. The perforated disks take considerably less time to pack since they are about ten times as thick as 400 mesh screens. The disks, like the screens, have to be restrained in the regenerator tube due to the spring force of the stack. This makes the screens and the disks more difficult to pack at low porosities which are desirable. Additionally, the perforated disks were packed using spacer rings which create a 0.0015" gap between the disks to allow for flow redistribution between disks.

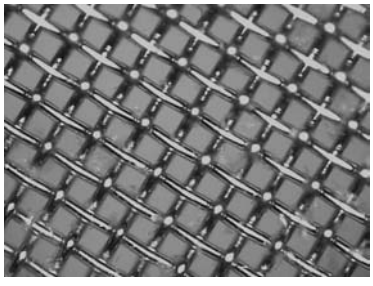

Figure 20 - Wire Mesh (200X magnification)

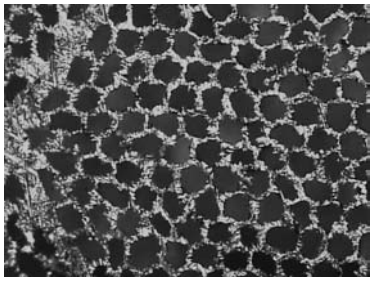

Figure 21 - Perforated Disk (200X magnification)

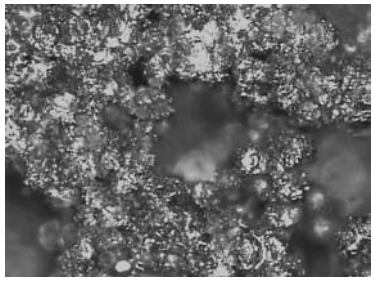

Figure 22 - Foam Metal (200X magnification)

An extensive data acquisition system was designed to provide test control and automated data collection. This system consists of a series of lab instruments which provide a variety of functions and a PC (Figure 23). The instruments and PC are connected using a GPIB 488 interface. GPIB is a laboratory instrumentation standard which provides communication and control via a PC. This provides a real-time data acquisition environment which provides for much more sophisticated measurements due to automation. Agilent VEE Pro software was used to create the data acquisition and control program. Several detail panels are shown in Figure 24, Figure 25, and Figure 26.

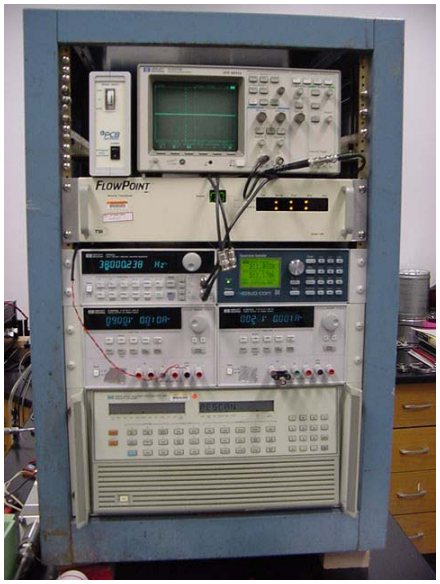

Figure 23 – Data acquisition system.

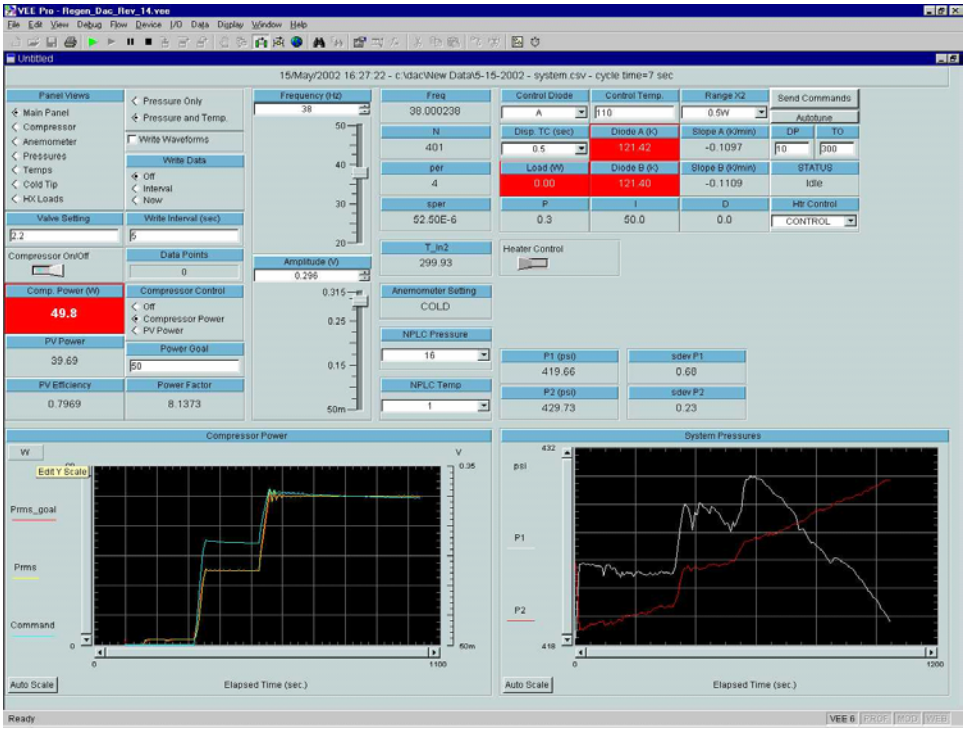

Figure 24 - Data acquisition and control program. Main panel view.

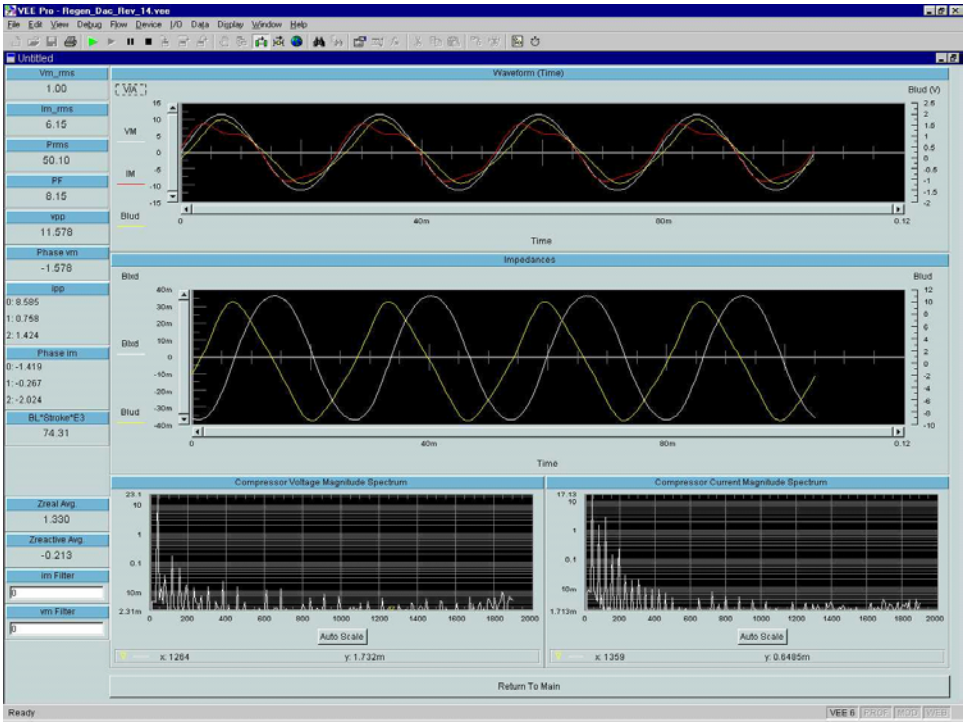

Figure 25 - Data acquisition and control program. Compressor panel view.

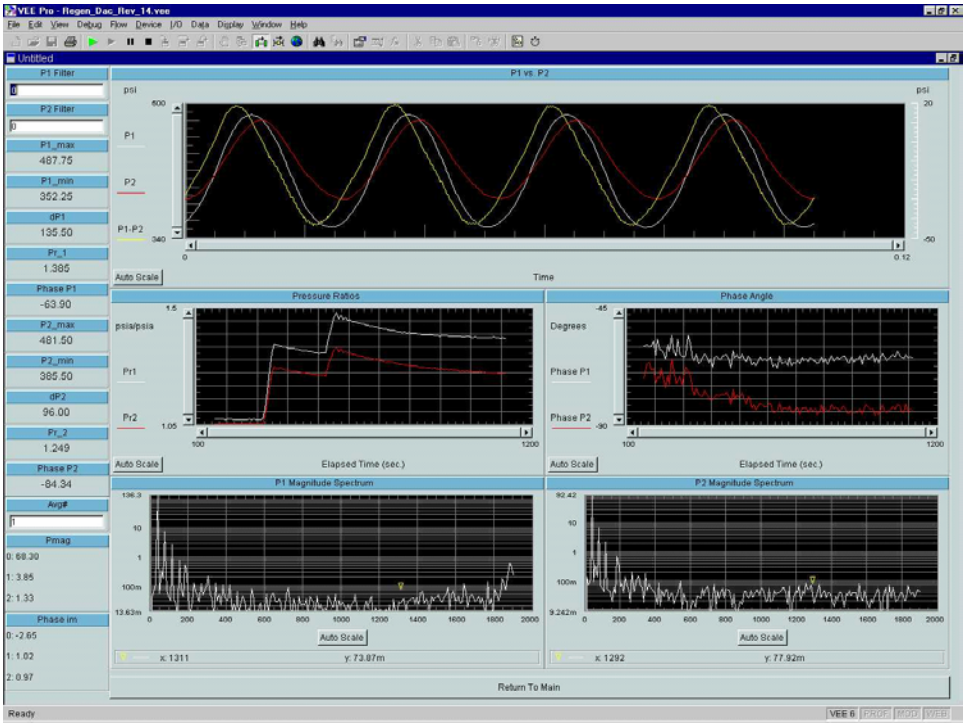

Figure 26 - Data acquisition and control program. Pressure panel view.

The data acquisition system has been in development for six years. Initially the objective was to measure a series of DC voltages such as thermocouples, diodes, pressure, etc. As the program developed, communication with most of the test instruments was incorporated allowing the program to monitor and display test data. Further developments included doing real time data analysis which can be used to automate and control the test. Pressure waveforms are acquired and stored for analysis. Discrete Fourier transform analysis is used to calculate phase angles and to analyze the frequency content of the various waveforms. The compressor electrical power input is measured with a wattmeter, and controlled digitally with a feedback control algorithm by the PC. The compressor voice coil voltage and current are measured as waveforms. Considerable effort has been invested to use these waveforms to infer the piston motion

from a kinematic model for the compressor pistons. This would allow calculation of the compressor PV power output, which would allow the compressor to be decoupled from the rest of the system from an efficiency viewpoint. However, the results are yet inconclusive. Tests need to be performed on a compressor which has piston position indicators. Appendix 3 has been included to summarize the development of the compressor model.

4.2 Experimental Results

Experimental data can be separated into two distinct categories. The first category consists of data measured under steady flow and essentially isothermal conditions for the purpose of determining friction factors. By varying the mass flow rate of gas through the regenerator and measuring the pressure drop, the two coefficients that characterize the momentum balance in the porous medium can be determined (ref. Figure 27 and Table 3). These are the Darcy permeability, K, and the Forchheimer inertia coefficient, c_f. The Darcy term, as discussed in previous chapters, is a measure of the viscous effects while the Forchheimer term is a measure of the inertial effects. Both of these terms are due to microscale, or pore scale, flow phenomenon which contributes to a macroscopic pressure gradient. The hypothesis of this research is that the Darcy and Forchheimer coefficients depend solely on the geometry of the porous media. Thus they can be measured by any convenient method, i.e. it is not necessary to conduct a series of mass flow versus pressure drop measurements at various temperatures. This hypothesis is tested in Chapter 5 by comparing the calculated pressure ratios with the experimentally

measured pressure ratios during actual cryogenic operation. This does not provide conclusive proof of the hypothesis. Direct pore scale simulations are required to test the hypothesis, and this work is suggested for future investigations. The volume averaging method produces a consistent model that can be tested via the pore scale simulations. The data in Table 3 was calculated using a control volume model rather than a differential model. As a result, the data is flawed and leads to artificially low friction factors. This data is revisited in Chapter 5.

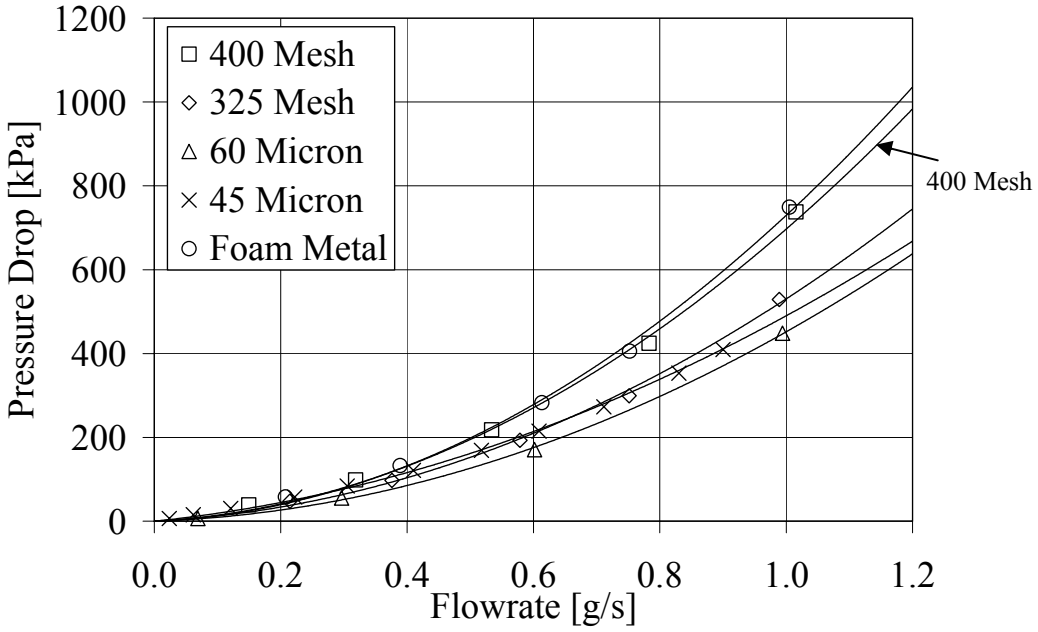

Figure 27 - Steady Flow Pressure Drop

Table 3 – Porous Media Parameter Summary (64)

	ε [%]	K [m^2]	c_f ---
Foam Metal	61.37	1.473E-10	0.5315
400 Mesh	69.20	1.005E-10	0.5163
325 Mesh	69.61	1.060E-10	0.3917
60 Micron	71.73	1.573E-10	0.4296

Some of the previously calculated pressure ratios using steady flow data did not correlate with experimentally observed pressure ratios (17, 17, 18, 19, 20, and 21). It is the opinion of this writer that either their model was incomplete (erroneous simplifying assumptions, presence of real gas effects, etc.) or that the Darcy and Forchheimer coefficients are not only dependent on geometry but possibly frequency and gas properties. Indeed, there are references in unrelated applications that address the issue of frequency dependent permeability (66). The authors assume that this frequency dependence is in fact a result of increasing inertial effects, which would indicate the Forchheimer effect.

A second set of data consists of measurements under actual operating conditions of the cryocooler. Of prime importance is the ability of the cryocooler to perform net refrigeration at varying temperatures. This is measured by constructing load curves (ref. Figure 28). These load curves provide an overall picture of the system performance. These curves are also used to estimate the total parasitic load on the cooler. From this data and the system level model, the pulse tube loss and the regenerator loss can be estimated. However, these estimates are only as accurate as the model. By comparing

two load curves for the same cryocooler with only the regenerator changed, and under the same operating conditions, the effect of the regenerator can be isolated in a sense.

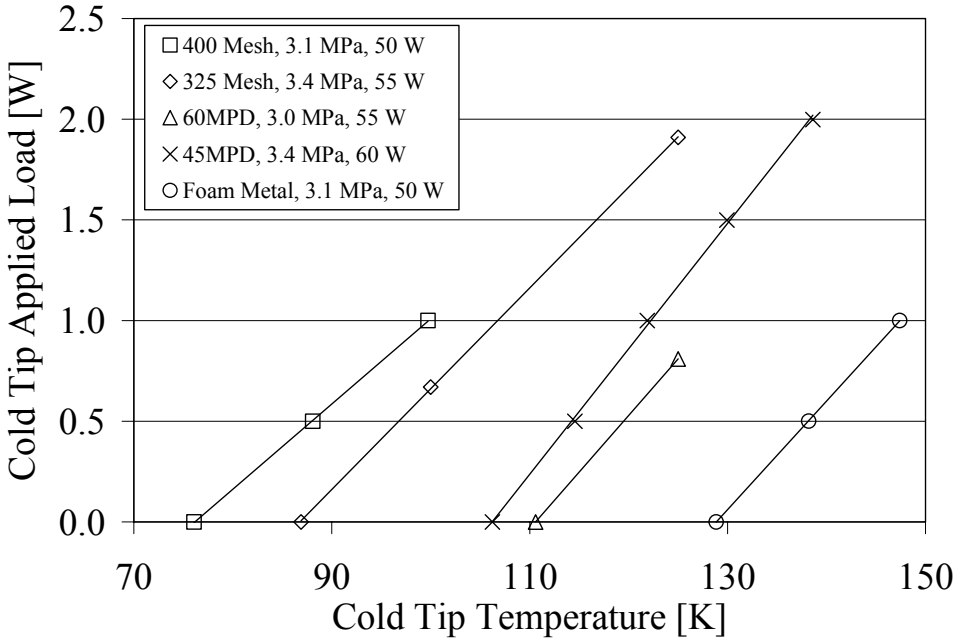

Figure 28 - Load Curves

As mentioned previously, the 400 mesh regenerator was tested with a larger volume pulse tube leading to a slightly more efficient expander. The temperature difference at no-load for the 400 mesh regenerator tested with the larger volume pulse tube was only 2-3 K (61) compared to the nominally 15 K differences. Therefore the comparison among the regenerators is still valid. The 400 mesh regenerator outperforms all of the other regenerators even if it is tested with the smaller volume pulse tube. In Chapter 5, the 400 mesh regenerator is modeled in Sage. This model accurately reflects the pulse tube geometry.

The performance tests provide a direct comparison between the regenerator matrices (63,64). The 400 mesh regenerator performed the best under the conditions of fixed input power, i.e. lowest no-load temperature. The fact that the 400 mesh regenerator out-performed the other matrices is not immediately obvious from the pressure drop data since the 400 mesh has one of the highest friction factors. This fact illustrates that the heat transfer efficiency is significantly better for 400 mesh than the other matrices.

The model will be shown to be driven by the pressures at the warm and cold end of the regenerator. Thus it is important to measure the effect that the regenerator has on the pressure wave. Figure 29, Figure 31, and Figure 30 illustrate that the pressure wave is attenuated and phase shifted by the regenerator and pulse tube expander. The oscillatory pressure drop is the magnitude of the instantaneous pressure difference across the regenerator/pulse tube which is measured experimentally. This parameter is influenced both by the difference in pressure amplitude as well as the pressure phase shift. The pressure phase shift as measured is primarily occurring in the regenerator even though the pulse tube is physically between the two points where the pressure is being measured. The pulse tube has minimal effect on the pressure because of its relatively short length and large diameter, i.e. it has a small friction factor. The ratio of the pressure ratios is a normalized measure of the frictional losses occurring in the regenerator.

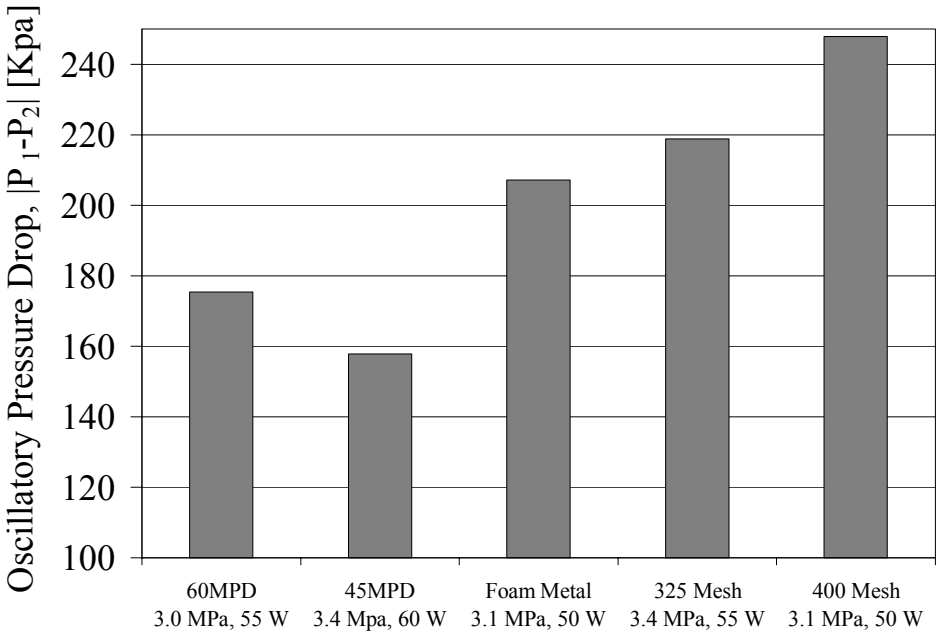

Figure 29 - Oscillatory Pressure Drop

The 400 mesh regenerator, which performed the best, has the largest oscillatory pressure drop and the largest pressure phase shift. The large phase shift is partly responsible for the magnitude of the oscillatory pressure drop. The 400 mesh and foam metal regenerators were similarly restrictive for steady flow. However, the oscillatory pressure drops are significantly different. The foam metal exhibited a smaller pressure phase shift which can partly explain this smaller pressure drop. It cannot be concluded from this data that the friction factor for the 400 mesh is higher for the oscillating flow.

The 400 mesh regenerator is modeled in Chapter 5. The pressure data for this regenerator is used to validate the system level model. The pressure amplitudes and phase shift are found to accurately characterize the model. The phase shift is found to be very sensitive to the porosity, increasing by up to 10 degrees with a 2% decrease in the

porosity. The packing density of wire mesh screens has a large influence on the regenerator performance.

The porosity of the 400 mesh and the 325 mesh were almost the same. The percent open area is higher for 325 mesh screens (36% for 400 mesh versus 41.3% for 325 mesh.) Percent open area is based on the wire diameter and spacing. This helps to explain why the 400 mesh has higher pressure drop.

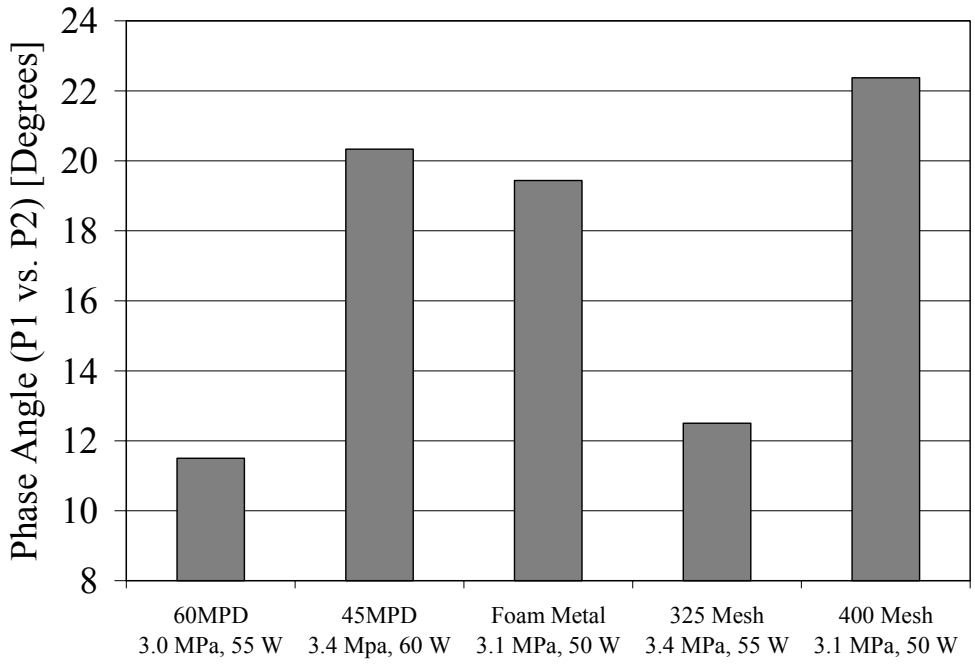

Figure 30 - Pressure Wave Phase Angle

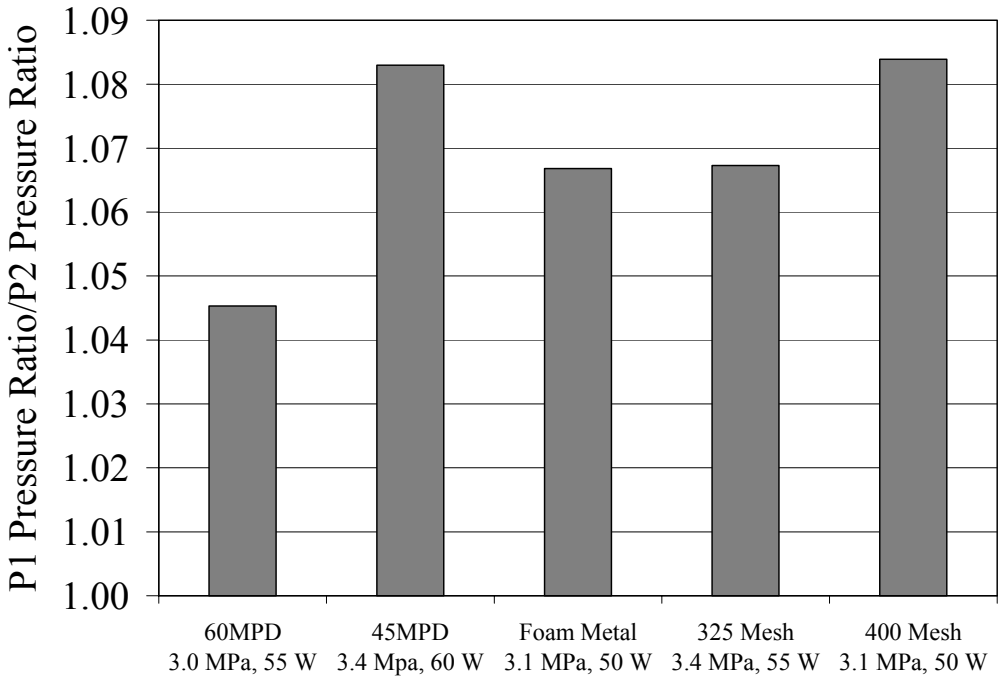

Figure 31 - Pressure Ratio Attenuation

The remaining 30 micron perforated disk regenerator remains to be tested. Testing is planned for the near future. Completion of this test will provide a complete set of data for this type of regenerator. It was a bit of a surprise to see the 60 micron and 45 micron regenerators perform almost the same. The expectation was that the smaller perforations would provide better heat transfer for similar pressure drop. The results show that the pressure drop was lower slightly higher than the 60 micron and significantly lower than 325 mesh. However, the 325 mesh provided better cooling performance.

The foam metal regenerator was retested by dicing it into 5 equal lengths using an electron discharge machining (EDM) saw. The EDM was found to be the only process which could cut the foam metal without closing the pores. Any abrasion or shearing

process produces a cut which completely closes the pores while EDM erodes the material away forming a clean cut. The diced sections were then precision-cleaned and installed into the regenerator using spacer rings made of laser cut 316 stainless steel shim stock. These rings were intended to create a gap between the foam metal plugs of approximately 0.0015" to further reduce conduction. The spacer rings were cut with an OD equal to the tube ID and a thickness of 0.013".

Testing of the diced foam metal regenerator produced no measurable difference in performance. This indicates that the poor performance was not due to the matrix conduction. In Chapter 5, the regenerator conduction is found to be the smallest loss in the regenerator, even smaller than the total conduction heat flux in the gas with the addition of dispersion heat flux. Reducing the solid conduction will only reduce the total regenerator loss by a few milliwatts. Dicing the foam metal should not affect any characteristic of the regenerator other than the solid tortuosity. Locally, the solid tortuosity approaches zero at the cut, but is quite high away from the cut.

The proposed Pyrex glass fiber regenerators did not turn out as expected. Fibers with an average diameter of 19 microns were procured. These fibers were then packed into glass sleeves in a variety of different manners. The best methodology was to chop the fibers to produce a fiber felt which could be packed uniformly and to desired porosity. This required pressing the glass felt to the desired porosity and then holding the felt into the tube. The tubes were then furnaced. The complex phenomenon of the sintering process made this a frustrating process. The furnace temperature needed to be high enough such that the fibers would soften and sinter but not flow or slump. The first

attempt produced a well sintered slug of glass fiber but the overall dimensions had shrunk by ~25% leaving an annular gap between the fibers and the tube. The second attempt was performed at a lower temperature, but still within the softening range of the fibers. Shrinkage was reduced to ~10% which is still too much. Any annular gap will destroy the regenerator performance. The third attempt was performed at the same temperature but with the fibers in compression using a dead weight and a piston. The piston length was chosen such that the final fiber column would produce the desired porosity. Since the fibers were in compression, they should expand radially to fill the tube during shrinkage. The piston did not compress completely on this attempt.

The sintered fiber samples from all three attempts were examined under a microscope to assess the sintering and fiber deformation (Figure 32.) It became quite obvious that the fibers would shed very easily from the sintered plug. At this point, there was no testable regenerator, and it was concluded that the fibers were not a viable alternative for a regenerator.

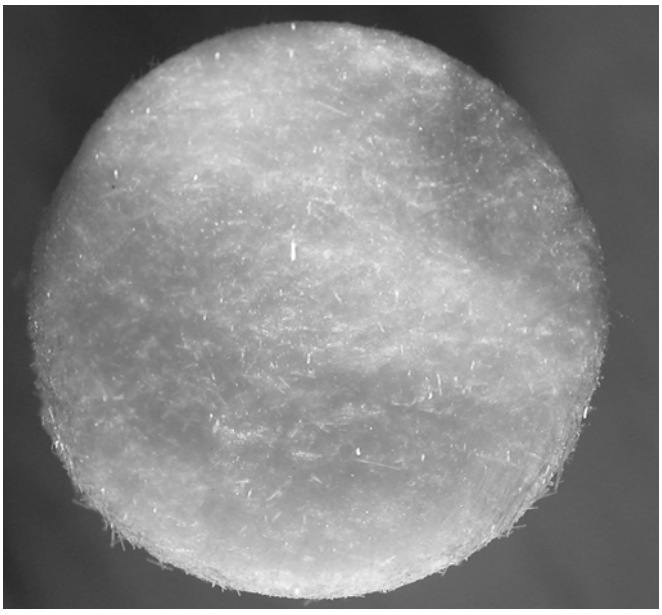

Figure 32 – Sintered glass regenerator.

CHAPTER 5

5. RESULTS AND DISCUSSION

In this chapter, the volume averaged model developed in Chapter 2 will be shown to be a flexible, accurate model. It is however a model of just the regenerator. A system level model is needed to estimate the boundary conditions for the regenerator model, and this model is developed in this chapter. The regenerator model is then used to obtain an accurate simulation of the flow and heat transfer in the regenerator. The solution is presented in terms of plots of important aspects of the solution, most importantly the regenerator loss. The regenerator loss is caused by several effects such as temperature oscillations due to finite matrix heat capacity, real gas properties, and temperature difference due to finite heat transfer coefficient. Asymptotic models developed in Chapter 3 are used to investigate the magnitude of these individual effects on the regenerator loss and the mean temperature profile. The accuracy of this model is considered by comparing it to other regenerator models and by calculating the entropy generation discrepancy as defined by the Sage model. A last comparison shows that a friction factor based on oscillating flow data is essentially identical to a friction factor based on steady flow data if a compressible flow model is used. The effect of compressibility is shown to account for a significant error in the measured friction factor.

5.1 Sage System Level Modeling

The regenerator model being developed is decoupled from the rest of the system via the particular boundary conditions. To evaluate the accuracy of the model, accurate boundary conditions for mass flow rate need to be applied. Ideally, these mass flow rates would be measured experimentally at both ends of the regenerator via hot wire anemometers or a similar method. With the apparatus used, these measurements were not possible at the cold end of the regenerator due to the integral design of the regenerator and pulse tube. The wall thickness of both tubes is only 0.007". If the mass flow boundary conditions are known, then the regenerator solution can be obtained with the additional knowledge of the regenerator geometry, friction factor, heat transfer coefficient, and dispersion coefficient.

The system performance is not completely known from just the regenerator solution though. The expander, whether a Stirling piston or pulse tube, will produce a net energy flow out of the cold volume which must carry the regenerator loss, other parasitic loads, and any net refrigeration. Thus, to compare the system level experimental data available from the laboratory pulse tube apparatus, there is a need for a system level model. To this end, a commercially available modeling tool called Sage was used.

Sage is a graphical programming package. The different components are represented by icons which are then connected to allow flow and energy transmission. Figure 33 illustrates the diagram of the lab cryocooler. After building the Sage model which contains all of the geometric aspects of the lab cooler, the model can be exercised over the range of experimental data. Pressure data at the transfer line and before the

orifice provide the primary method of correlating the Sage model. To drive the model, the compressor piston stroke needs to be specified. This data is unavailable experimentally with the current compressor. However, the Sage optimizer can be used to adjust the compressor stroke and orifice setting until the two pressure ratios match. The additional degree of freedom is the pressure phase difference. This phase shift in the pressure is due primarily to flow friction, most of which occurs in the regenerator. The Sage model initially gave incorrect pressure phase shift predictions. Experimentation indicated that the friction in the regenerator was too low, either due to an inaccurate friction factor or incorrect porosity. The porosity was adjusted until the exact phase shift, which was measured experimentally, was achieved. This porosity was then kept constant for the 0.5 and 1.0 W cases. The resulting porosity was found to be 0.663 for 400 mesh. The measured porosity was 0.692 calculated based on an assumed density and known mass. This difference was found to be attributable to a density difference for the stainless steel alloy used to make the screens which results in a 2% density difference. This is comparable to the differences in the porosity.

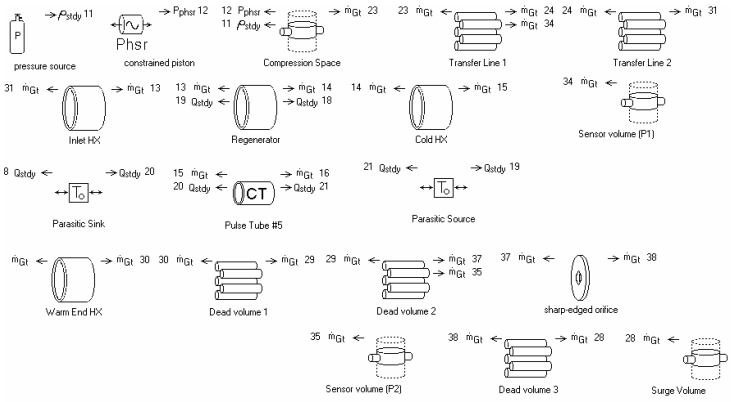

Figure 33 – Sage diagram of the laboratory pulse tube apparatus.

Sage provides useful system level details such as the energy flow map in Figure 34. The critical energy balance for any cryocooler is based on a control volume containing the cold heat exchanger. This map is based on the 400 mesh regenerator operating at its coldest temperature of 76 K. At this temperature, and with 50 W of electrical input power, the cooler produces zero net refrigeration. Considering the cold heat exchanger control volume, the pulse tube enthalpy flow is consumed totally by the regenerator loss and the regenerator wall conduction loss. The model illustrates that the gross refrigeration, in this case 2.09 W, is rejected at the warm end of the pulse tube. The surge volume accounts for a large portion of the total heat rejection which seems rather contrary. The critical aspect of the warm end heat transfer is that energy is conserved.

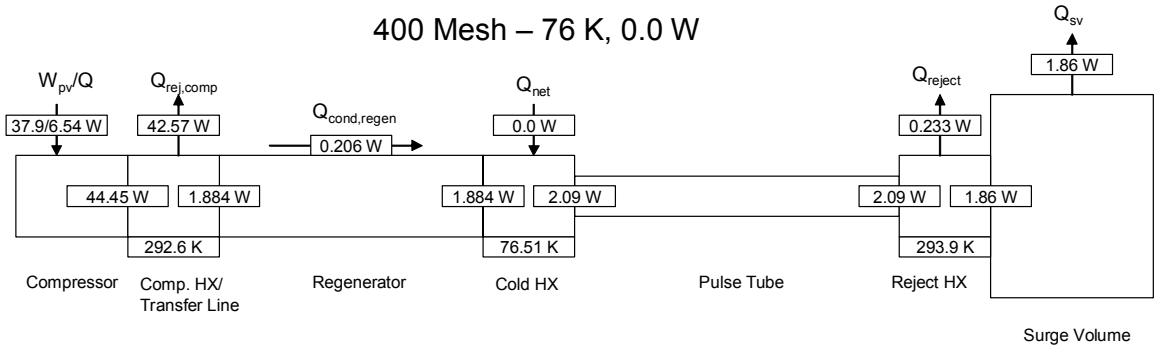

Figure 34 - System level energy flow diagram; 400 mesh, 76 K, 0 W

The additional experimental data which was used to correlate the Sage model was the measured net refrigeration. The 400 mesh regenerator was operated with three refrigeration loads; 0.0, 0.5, and 1.0 W. For each refrigeration load, the pressure ratios and phase shifts were measured. The Sage predicted refrigeration was not accurate

initially. This is probably due to inaccuracies in the empirical pulse tube correlations which Sage uses. Several phenomenons contribute to reduced pulse tube refrigeration such as mass streaming and boundary convection, according to the Sage model. These effects are modeled in Sage as enhanced diffusion effects based on some theoretical and experimental correlations. These correlations were constructed for larger capacity pulse tubes, so their accuracy in this size range is unknown. Sage provides a scale factor to adjust these pulse tube losses. This factor was adjusted at the no-load point and then it was used for the 0.5 W and 1.0 W cases. The correlation was reasonably good; 1.072 W predicted versus 1.0 W measured. This error is within experimental error and certainly within the range of unknown radiation load.

Table 4 – 400 mesh baseline operating conditions

	0.0 W	0.5 W	1.0 W
$\dot{m}_h$ [g/s]	0.949	0.913	0.904
$\dot{m}_c$ [g/s]	0.720	0.679	0.652
Frequency [Hz]	34	34	34
$\phi_{\dot{m}_h} - \phi_{\dot{m}_c}$ [deg.]	15.4	16.4	17.0
T_h [K]	292.6	292.6	292.7
T_c [K]	76.51	88.44	100
Charge Pressure [MPa]	3.1	3.1	3.1

The regenerator boundary parameters can then be extracted from the correlated model. Table 4 summarizes the 400 mesh regenerator operating conditions. These parameters were then used to perform comparison calculations with the model proposed in Chapter 3. In this table, the mass flow rates decrease with increasing cold tip temperature. This decrease in mass flow rate is accompanied by an increase in the mass

flow phase angle. This is a result of the decreasing regenerator loss which is proportional to the phase difference between the pressure and mass flow waves.

5.2 Model Comparison

In this section, the results of the limiting case models presented in Chapter 3 are illustrated in terms of the net regenerator enthalpy flow rate and the mean temperature profile. The full regenerator model is then discussed beginning with a presentation of the solution fields. Several post-processing results such as net energy flows and net entropy generation rates are then presented. The model is then compared with the Sage and REGEN model solutions. Finally, the results of the analytic method of determining the permeability and inertia coefficient from Chapter 2 are presented.

5.2.1 Net Enthalpy Flowrate - The Perfect Regenerator

The net energy flow rate in the regenerator represents a loss mechanism since this energy must be carried by the gross refrigeration effect of the expander whether it be a pulse tube or a Stirling displacer. The regenerator loss is a result of conduction and dispersion in the gas, conduction in the matrix, and net enthalpy flow due to the mass flux and enthalpy being partially in phase. Only in the limit of zero conduction or dispersion and zero net enthalpy flux is the regenerator loss zero.

Figure 35 is a comparison of the calculated regenerator loss for the three models (CTM, LTEM, and DEEM) with additional calculations to compare the effect of real gas properties. The ideal gas cases additionally assume constant properties evaluated at the

mean temperature. The operating conditions were kept constant for all models. The Constant Temperature model, as described in Chapter 3, is the most idealized model. The only non-idealities included in this model are pressure drop, gas conduction and dispersion, and matrix conduction. The resulting regenerator loss is only 0.33 W, due mainly to conduction and dispersion. The addition of real gas properties results in a 0.8 W increase. This increase in the regenerator loss is due to the fact that the enthalpy for a real gas depends on both temperature and pressure. For the ideal gas, enthalpy depends only on temperature, which is constant for this model. As a result, the real gas enthalpy oscillates partially in phase with the mass flux. For the case of ideal gas, constant properties evaluated at the average of the end point temperatures were used. This has a significant impact on the viscosity which is strongly dependent on temperature over the range of interest.

The Local Thermal Equilibrium model was written only for ideal gas. So a good comparison of the increase in the regenerator loss due to finite thermal capacity is the ideal gas CTM and the LTEM. In this case, there is a 0.86 W increase. This increase in regenerator loss is due to additional net enthalpy flow due to the local temperature oscillation which is allowed in this model. As a result, the enthalpy oscillates locally in phase with the temperature (and partially in phase with the mass flux.)

The Dual Energy Equation Model captures all of the non-idealities in the regenerator, specifically the addition of finite temperature difference between the gas and matrix. This temperature difference leads to an increase in net enthalpy flow of nearly a

watt (comparing the ideal gas LTEM and ideal gas DEEM.) This increase is due to a more adverse (smaller) phase angle between enthalpy and mass flux.

Being able to decompose the total regenerator loss provides insight into the relative importance of the competing design challenges with regenerators. Although there are no direct simulations provided in this report, as the cold temperature decreases below the 20 K point the problem of matrix heat capacity becomes a severely limiting factor. The reason is made evident by comparing the CTM and LTEM results. A factor that is present at any temperature is the inverse relationship between heat transfer effectiveness and pressure drop. This analysis does not explicitly illustrate the effect of pressure drop. Pressure drop represents a loss of available energy for the pulse tube or expander piston to convert to refrigeration.

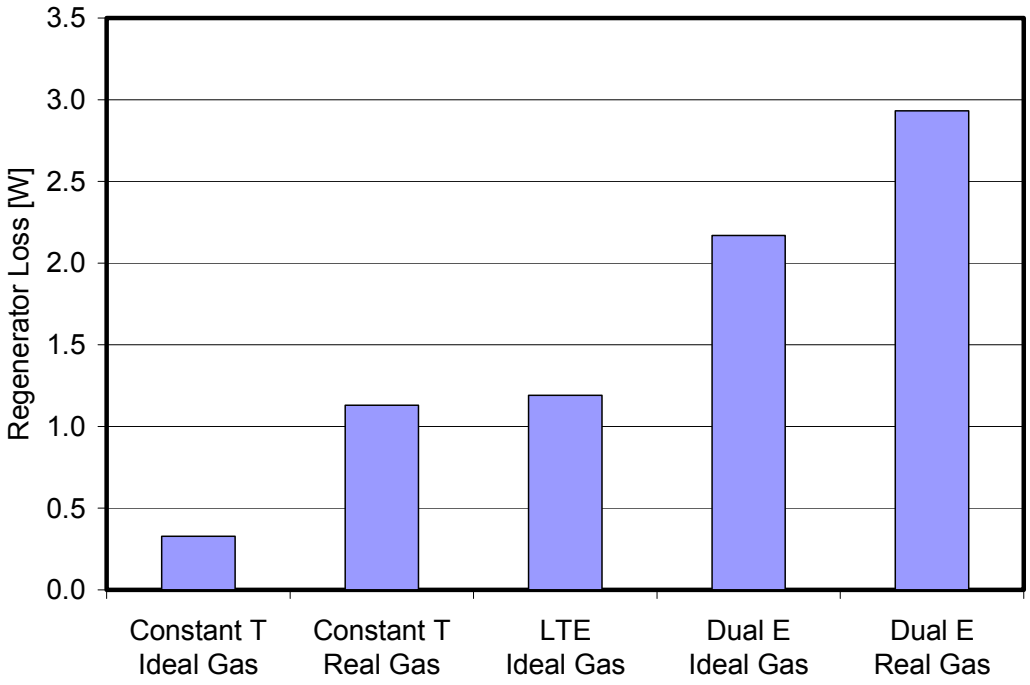

Figure 35 – Comparison of regenerator loss calculated with limiting case models based on identical operating conditions (ideal gas assumes constant properties.)

5.2.2 The Mean Temperature Profile

At quasi-steady state, the net diffusion and enthalpy fields are in a balance such that the total energy flow through the regenerator is constant. The shape of the net diffusion and enthalpy fields is strongly affected by the mean temperature profile. Model convergence is primarily limited by the convergence of the steady mean temperature profile. Figure 36 illustrates the effect of the different models on the mean temperature profile. The CTM profile is nearly linear, with a slight, -3 K, deviation at the midpoint. A dramatically different profile occurs with the addition of real gas properties, with the midpoint temperature 36 K higher. This difference between the ideal gas and real gas cases is partly due to the fact that the viscosity is temperature dependent has a significant variation over the range of temperatures. The ideal gas case uses a constant viscosity evaluated at the average temperature. The LTEM profile is higher at the midpoint by 9 K and the ideal gas DEEM profile higher by 17 K. The real gas DEEM also shows a dramatic deviation especially at the cold end, where the gradient is almost zero. An interesting comparison exists between the two real gas cases. The mean temperature profiles for the real gas CTM and DEEM represent the extremes of all the profiles. The likely cause of this deviation is the finite matrix heat capacity in the DEEM. The CTM assumes that the heat capacity is essentially infinite such that no temperature fluctuations occur.

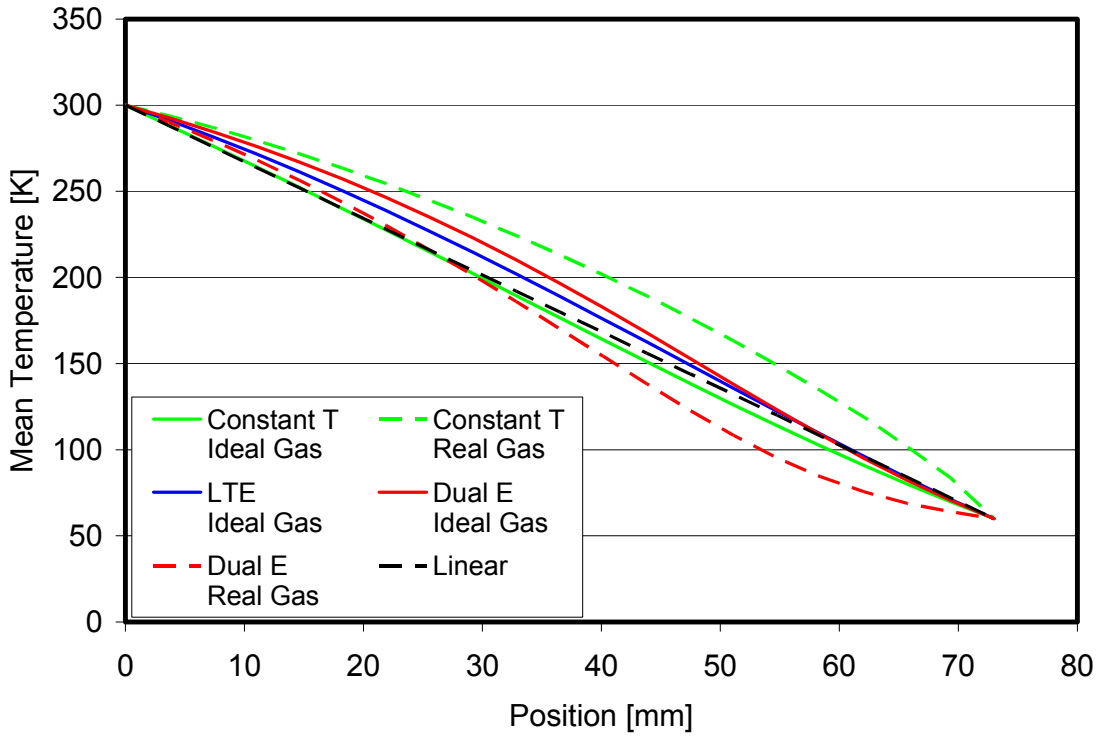

Figure 36 – Comparison of mean temperature profiles calculated with the different models based on identical operating conditions.

5.2.3 Baseline Regenerator Solutions

The regenerator model solves for density, mass flux, gas total energy, and matrix temperature at periodic quasi-steady state. From these solutions, pressure, velocity, enthalpy, and entropy can be calculated. The local, instantaneous solutions are shown in Figure 37. In the upper right, the density field is shown versus time (horizontal axis) and position (family of curves with red and blue corresponding to hot and cold ends respectively.) Below this figure, the density maximum and minimum profiles are plotted versus position in the regenerator. This illustrates the relative difference in the spatial and temporal scales for the density. The temporal scale (max versus min) is small

compares to the spatial scale (cold end versus warm end.) The velocity is given similar treatment. The velocity at the cold end is much smaller than the velocity at the warm end due to the large density difference. The mass flow rates (bottom left) are comparable in magnitude but with a noticeable phase shift. Pressure is totally driven by the mass flow boundary conditions (or vise versa with pressure boundary conditions.) The pressure wave is attenuated and shifted in phase as it passes through the regenerator. Both of these phenomenon are measured in the apparatus.

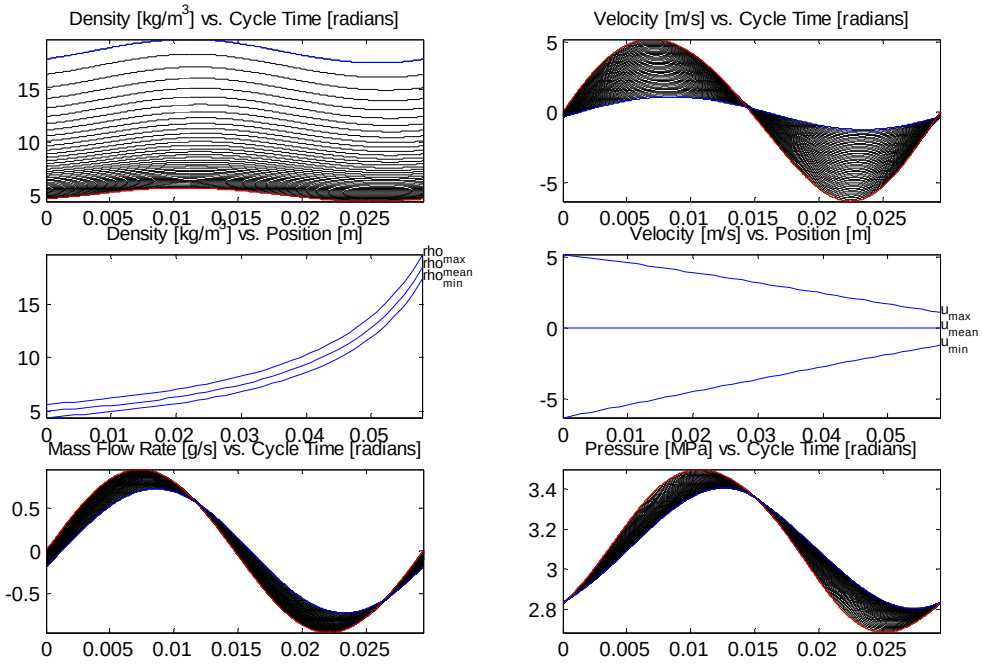

Figure 37 – Solutions plotted versus time and position. The middle plots are max and min of density and velocity. Pressure and mass flow phase shifts are apparent.

The temperature field is calculated from the density and total energy using the appropriate caloric equation of state (ideal or real gas.) In this problem, the temperature

is not specified on the boundaries. The predicted gas and matrix temperature waves at the warm and cold ends are shown in Figure 38. The gas temperature leads the matrix temperature, as would be expected. The gas temperature has a distortion which occurs at the flow reversal. This is due to the reduction in the heat transfer coefficient at low velocities. The flow reversal is also associated with the beginning of the expansion process which causes a reduction in the gas temperature.

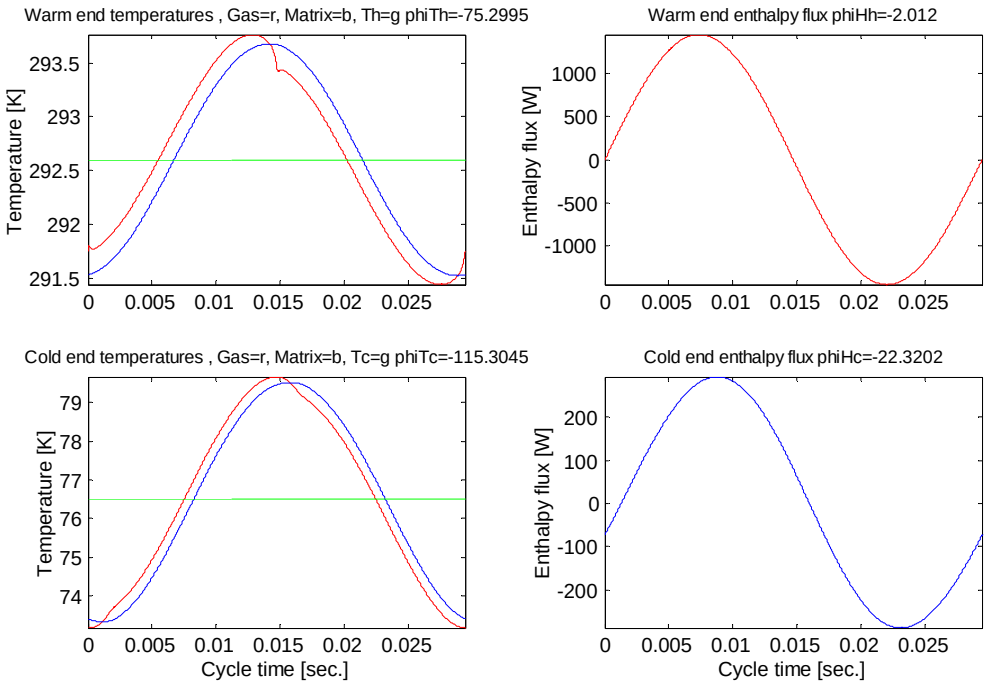

Figure 38 – Boundary solutions for the gas and matrix temperatures and enthalpy flow rates.

The enthalpy is also calculated from the total energy and density. In the figure, the enthalpy flux at the warm and cold end have extremely large amplitudes (1500 W and

300 W) compared to the DC component which is less than 2 W. It is this DC component which is critical to be able to predict accurately.

The mean temperature profile for this baseline case is shown in Figure 39 in comparison to a linear profile. It is this temperature profile which converges the solution to periodic quasi-steady state.

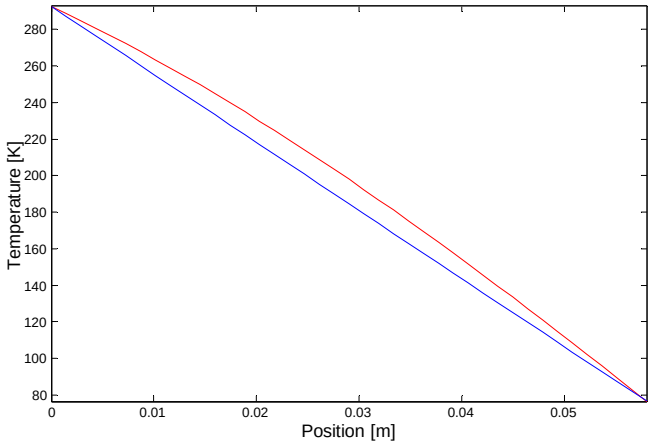

Figure 39 – Cycle-averaged gas temperature (red) versus a linear profile (blue).

The temperature difference (Figure 40) is a critical aspect to the regenerator problem. This temperature difference is responsible for a large percentage of the regenerator loss. The temperature difference is noticeably smaller at the cold end due to considerably larger mean Reynolds number at the cold end as shown in Figure 41.

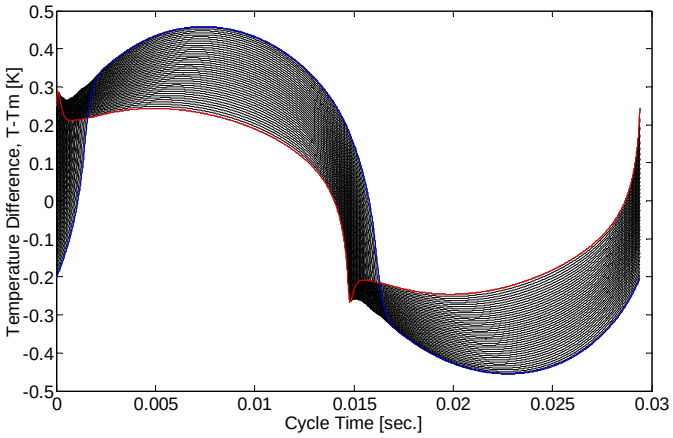

Figure 40 – Temperature difference versus position (multiple lines) and time.

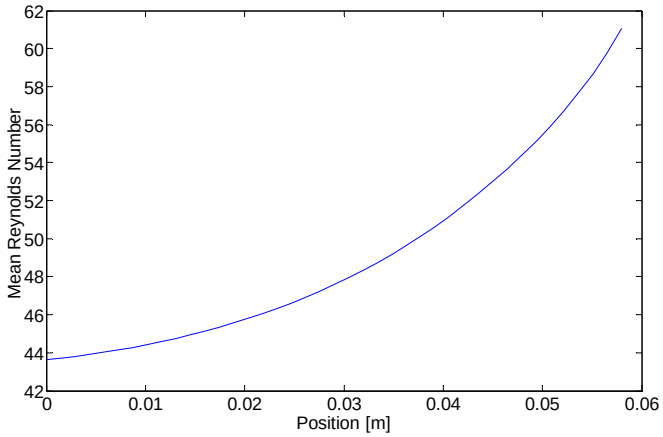

Figure 41 – Mean Reynolds Number

5.2.4 First Law Results

Cycle averaging of the solutions during postprocessing provides the most important aspects of the solution such as the net mass flow rate and enthalpy flow rate. Figure 42 illustrates that at steady state, the net mass flow rate is very small, essentially numerical noise. The net enthalpy and heat fluxes due to conduction and dispersion are

not zero and are shown in Figure 43. The critical point is that the total energy flux through the regenerator is constant.

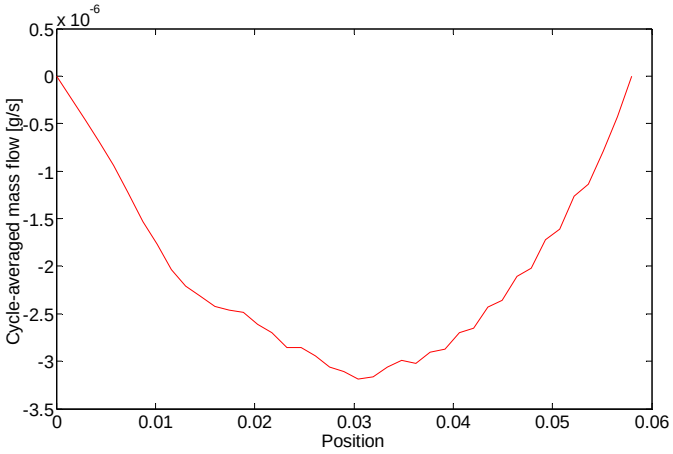

Figure 42 – Cycle-averaged mass flow rate.

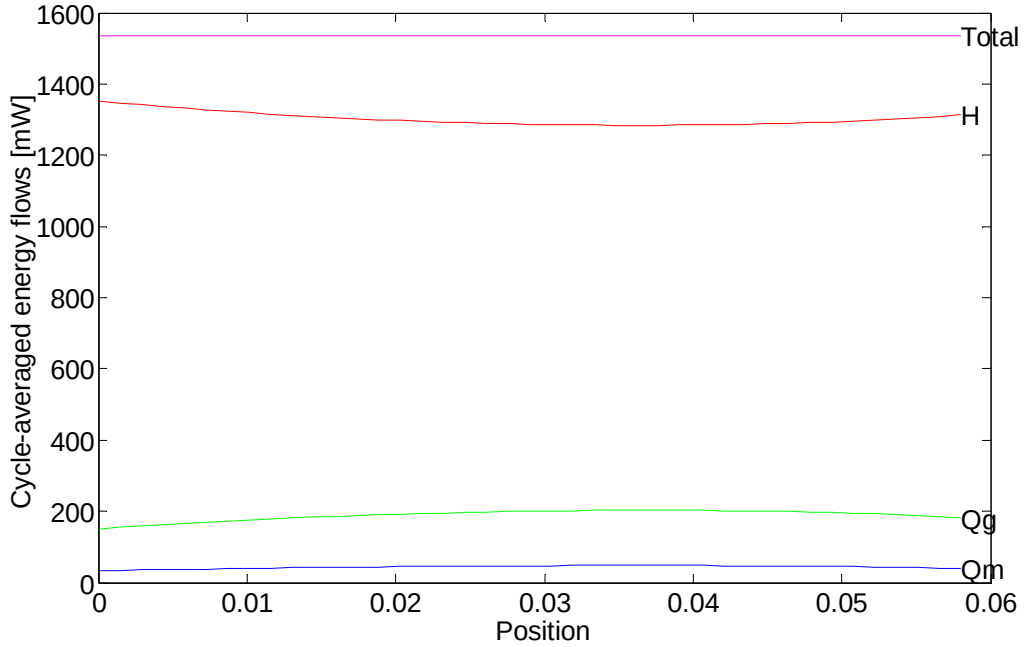

Figure 43 – Cycle-averaged energy flows. Regenerator total energy flow is constant along regenerator.

5.2.5 Second Law Results

Entropy generation is calculated in postprocessing as well. The individual sources of entropy generation are illustrated in Figure 44 and Figure 45 as functions of position and time. The entropy generation due to viscous and inertial losses is the dominant source, contributing almost 80% of the total available energy loss in this case. The entropy generation due to the gas conduction and dispersion is characteristically different than the entropy generation due to the matrix conduction. Since the dispersion is proportional to the Peclet number, it is oscillatory as can be seen. The matrix conduction only shows slight oscillation. The entropy generation due to interfacial heat transfer is the second largest contributor to available energy loss, but it is the dominant contributor to regenerator net enthalpy flow.

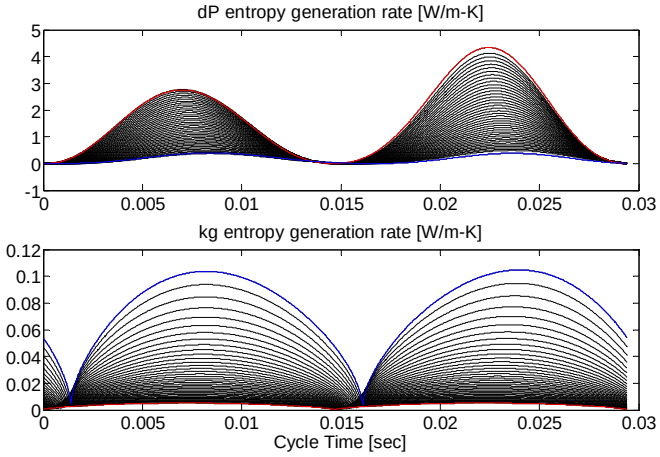

Figure 44 – Entropy generation due to viscous and inertial losses (top), and entropy generation due to conduction and dispersion in the gas (bottom). Multiple curves represent different locations in the regenerator, plotted versus cycle time. Results for 400 mesh baseline case.

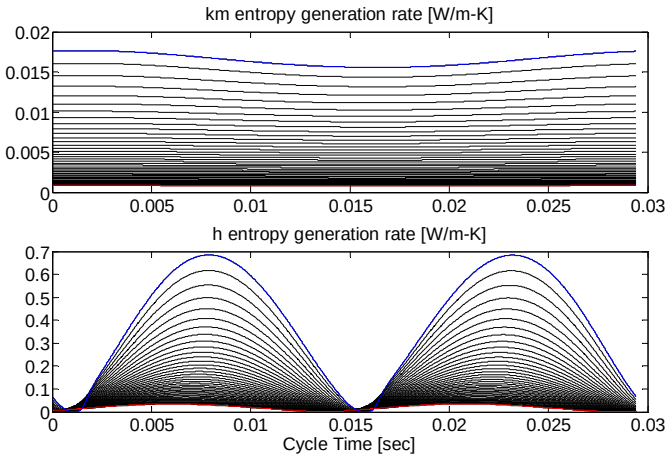

Figure 45 – Entropy generation due to matrix conduction (top), and entropy generation due to interfacial convection (bottom). Results for 400 mesh baseline case.

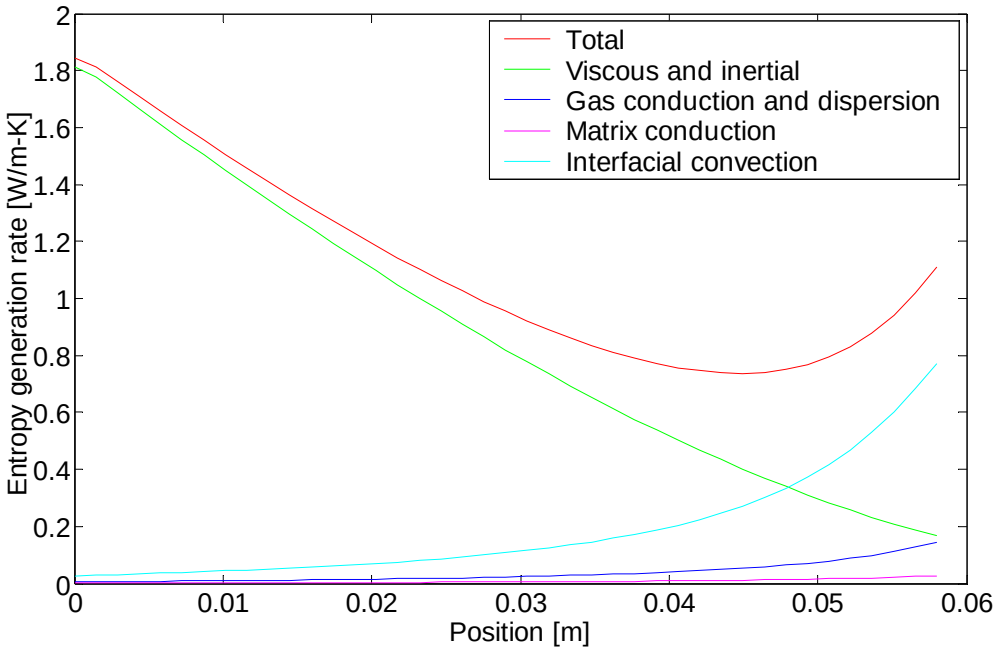

Figure 46 – Cycle-averaged volumetric entropy generation rates plotted versus position in the regenerator. Results for 400 mesh baseline case.

Figure 46 provides an interesting picture of the entropy generation mechanisms. The viscous ad inertial entropy generation decreases to almost nothing at the cold end, but the interfacial heat transfer component increases sharply at the cold end due to the 1/T nature. The total entropy generation has a surprising shape with a minimum in the interior of the regenerator. The area under these curves represents the net total entropy generation, with units W/K.

5.2.6 Sage and REGEN Comparisons

Sage provides the solution grid for the regenerator. From this, the net energy flow profiles can be constructed. Figure 47 is a comparison of Sage, the Georgia Tech model proposed in this thesis, and profiles from a third model known as REGEN3.2. REGEN3.2 was developed at the National Institute of Standards and Technologies (NIST.) It models only the regenerator, but with a simplified model. All three models were run with identical inputs. The profiles plotted for REGEN are after 100,000 cycles of simulation time which took several hours. The solution is still not satisfactorily converged as can be seen by the total energy flow profile which has a 10% variation along the regenerator. The Sage profiles correlate roughly with the Georgia Tech model which is the most visibly accurate. The Sage model apparently forces the matrix conduction flux to zero at the ends giving the profiles an abrupt transition at the ends. This produces a sharp corresponding increase in the enthalpy flux at the ends. The REGEN seems to grossly over predict the total conduction which is counterintuitive since the model wholly neglects dispersion.

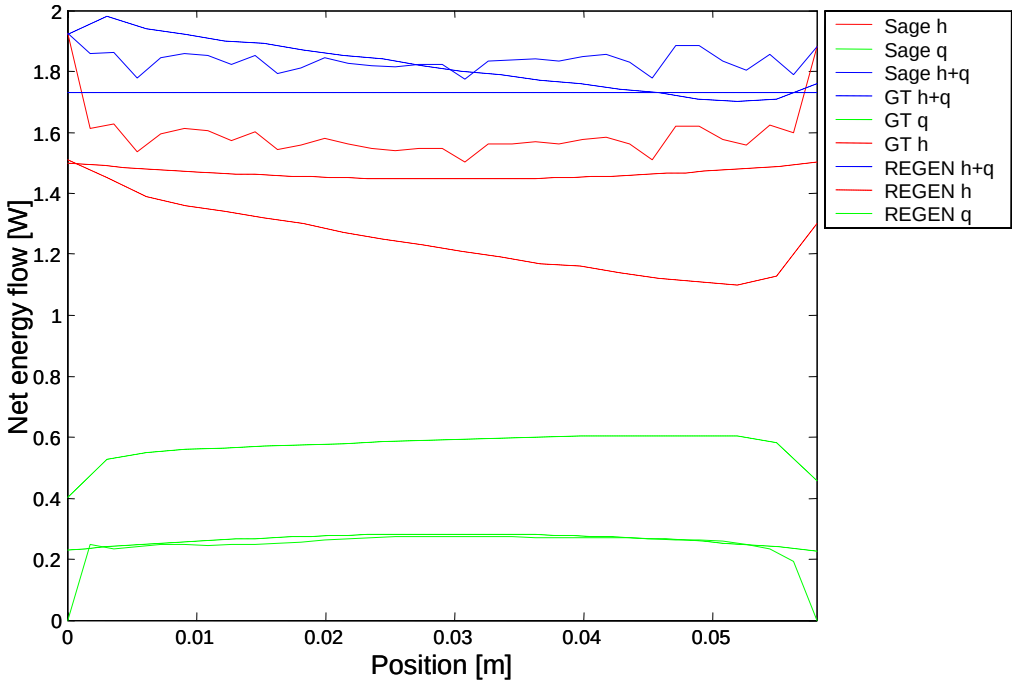

Figure 47 – Comparison of Sage-predicted regenerator loss versus GT model.

REGEN, as mentioned previously, assumes that the pressure gradient is negligible. The GT model does not make this assumption. The REGEN model as a result of this assumption produces a non-conservative scheme while the GT model solves a fully conservative set of equations. This may be the cause of the REGEN model not converging to a constant energy flow rate as seen in the figure.

Table 5 is a summary of the comparison calculations with Sage. Sage predicts a moderately higher regenerator loss. The regenerator loss is seen to decrease with increasing cold end temperature. This source of error is approximately 8%. The effect of this error directly translates into an error in the net refrigeration prediction. However, this error is small in comparison to the uncertainty in the pulse tube net enthalpy flow.

Table 5 – Sage Comparison Summary

	GT			SAGE		
Net refrigeration	0.0	0.5	1.0	0.0	0.5	1.0
Regenerator Loss	1.73	1.60	1.54	1.84	1.744	1.671
Viscous and inertial lost power	15.3	14.2	14.1	15	14.18	14.02
Interfacial heat transfer lost power	3.17	2.36	1.87	3.15	2.34	1.85
Gas conduction and dispersion lost power	0.618	0.477	0.381	-	-	-
Matrix conduction lost power	0.129	0.105	0.087	-	-	-
Total gas and matrix conduction and disp.	0.747	0.582	0.469	0.713	0.553	0.441
Total lost power	19.2	17.2	16.4	18.9	17.1	16.3
Lost power based on external calculation	19.2	17.2	16.4	19.0	17.2	16.4
Lost power discrepancy	-0.029%	-0.012%	-0.060%	-0.734%	-0.481%	-0.270%
Warm end pressure ratio	1.30	1.31	1.33	1.30	1.31	1.33
Cold end pressure ratio	1.22	1.22	1.24	1.21	1.22	1.24
Warm end pressure phase angle	-42.6	-43.1	-44.9	-42.7	-43.27	-45.11
Cold end pressure phase angle	-62.8	-62.2	-63.4	-63.1	-62.5	-63.6

The available energy predictions correlate very well between the two models. The Georgia Tech model demonstrates better available energy discrepancies (0.03% versus 0.5%.) This discrepancy is calculated, in both models, by summing the internal sources of entropy generation due to conduction, convection, dispersion, and flow friction. The sum of the internal entropy generation rates is then compared to the entropy generation rate determined by an external calculation, i.e. integrating the entropy flux at the boundaries. Ideally, these two methods of calculating the entropy generation rate are identical. However, due to numerical errors, these two methods will produce different results. This discrepancy is then a measure of the accuracy of the numerical scheme.

The GT model is an order of magnitude more accurate than the Sage model. The REGEN model does not provide this data, so a comparison cannot be made.

Pressure ratios and phase angles correlate well with each other as well as with experimental data. The GT model requires that the mass flux be specified at both ends. The pressure waves which develop are an output from the model. Ideally these pressure waves should match experimental data in both amplitude and phase. The mass flux at the ends are unknown experimentally, so the results of the Sage system level model are heavily relied upon for this information. The pressure waves are sensitive to accurate modeling of the friction factor in the regenerator. The following section provides a discussion of the friction factor prediction from experimental data. These predictions made using a compressible model and are shown to be comparable to friction factors measured in oscillatory flow.

5.2.7 Permeability and Forchheimer Coefficient Predictions

Chapter 2 introduced a method to predict the permeability and Forchheimer inertial coefficient using three analytical solutions to the continuity and momentum equations. The results of this methodology are presented in Table 6 - Table 8. The compressible model is the most realistic since this model predicts the increase in pore velocity as the pressure decreases in a steady flow test. The decrease in pressure, which occurs in incompressible flow as well, leads to a density decrease for a gas flow. The same predictions were made with the incompressible model. The compressible inertial term is consistently 30% higher for all of the matrices tested while the permeability is

almost identical. The permeabilities should be identical since this parameter characterizes the low Reynolds number regime of the flow where compressibility is much less important.

The final comparison assesses the importance of the advective acceleration term in the momentum equation. Both the permeability and inertial coefficient are identical for all of the matrices tested. This indicates that the inclusion of the advective acceleration term, at least for steady flow, is not necessary.

Table 6 – Permeability and Forchheimer Coefficient (compressible model)

	K	c_f
400 Mesh	2.69E-11	0.407
325 Mesh	3.53E-11	0.376
Foam Metal	2.80E-11	0.445
60 Micron	4.91E-11	0.372
45 Micron	2.21E-11	0.259

Table 7 – Permeability and Forchheimer Coefficient (incompressible model)

	K	c_f
400 Mesh	2.69E-11	0.282
325 Mesh	3.53E-11	0.260
Foam Metal	2.80E-11	0.308
60 Micron	4.91E-11	0.257
45 Micron	2.21E-11	0.179

Table 8 – Permeability and Forchheimer Coefficient (neglecting advective acceleration)

	K	c_f
400 Mesh	2.69E-11	0.407
325 Mesh	3.53E-11	0.376
Foam Metal	2.80E-11	0.445
60 Micron	4.91E-11	0.372
45 Micron	2.21E-11	0.259

A comparison of the friction factor predicted from measurements using 400 mesh yield close agreement with the friction factor used in Sage as shown in Figure 48. The friction factor and Reynolds number are defined using different length scales in Sage. The friction factor and Reynolds number, as defined in Chapter 3, use the permeability length scale which is measured experimentally. The length scale used in Sage is a hydraulic diameter based on an approximate geometrical definition which depends on the porosity and the wire diameter in the case of screens.

There is only a slight deviation in the two friction factors at high Reynolds number. This is interesting in light of the methodology in which the Sage friction factors were measured. The friction factor, heat transfer coefficient, and dispersion coefficient for screens and felts were measured using an oscillatory flow test rig, in hopes of gaining some improved predictions (19). It is obvious from this comparison that the flow oscillations may not be nearly as important as the compressibility. It is suspected that the friction factor depends only on the microscale geometry while the flow friction depends on the actual macroscopic flow field and fluid properties. The compressible model provides more motivation that this hypothesis is true.

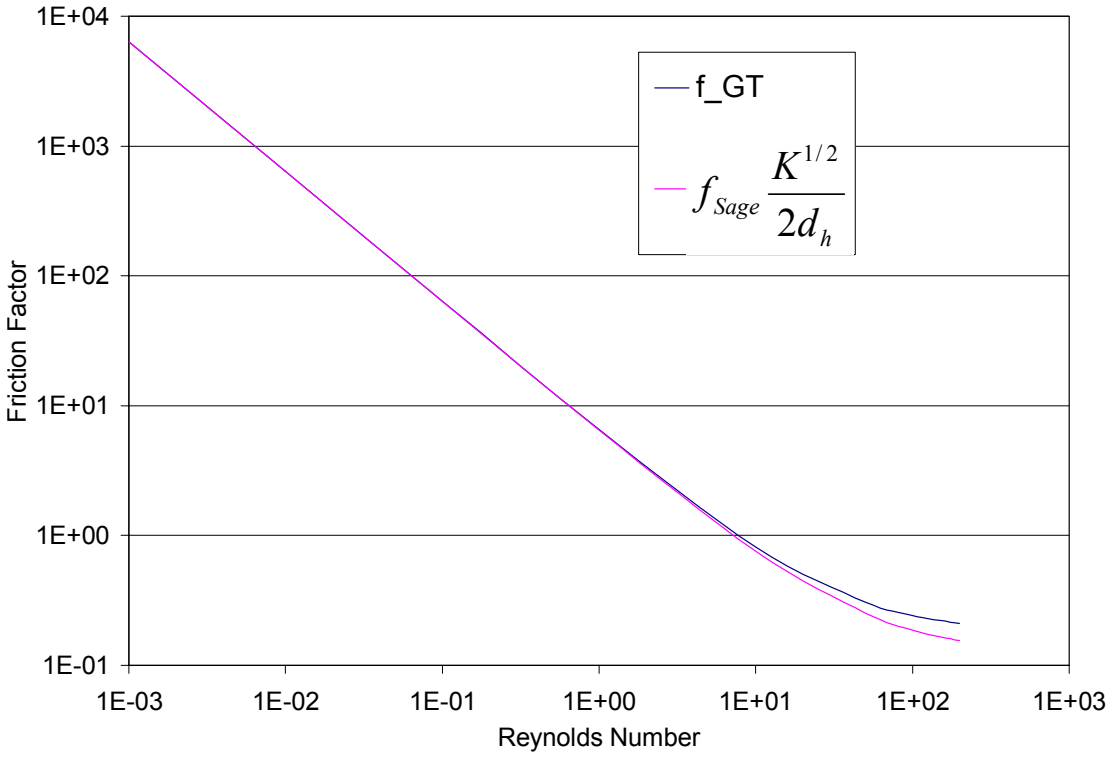

Figure 48 – Friction factor comparison for 400 mesh screens

CHAPTER 6

6. CONCLUSIONS AND RECOMMENDATIONS

6.1 Conclusions

The governing equations for the flow and heat transfer which hold for a point in space and time were volume-averaged, producing a set of continuum equations for the porous regenerator. These equations contained several source terms which represent the viscous and inertial friction, gas-to-matrix heat transfer, and thermal dispersion. Several additional terms were neglected based on scaling arguments. The simplified equations describe unsteady compressible flow and heat transfer in a porous medium.

The dimensionless regenerator model was found to depend on two leading order dimensionless parameters and two second order parameters. These parameters indicate that the second order diffusion terms are small and should not be used as justification for requiring additional boundary conditions. The resulting problem requires only two mass flow boundary conditions and an appropriate method for finding the quasi-steady initial condition.

The oscillatory regenerator flow solution was found to depend strongly on the mean temperature profile. Finding this mean profile with a semi-analytical technique allows the solution to be advanced in time much faster than with direct simulation. This provides a huge computational advantage.

To validate the numerical method, an exact solution was found which required additional source terms to be added to the governing equations. The numerical solution agreed with the exact solution within $O(10^{-6})$ normalized errors.

A method for experimentally testing a cryocooler regenerator has been developed. Pressure waves are measured at the warm ends of the regenerator/pulse tube. The net refrigeration is measured with an applied heat load over a range of refrigeration temperatures. A data acquisition system provides the ability to make high speed measurements and for test control. Six regenerators were tested with a near-identical apparatus: 400 mesh, 325 mesh, 60 and 45 micron perforated disks, foam metal, and diced foam metal. An additional 30 micron perforated disk regenerator is planned for testing. An optional glass fiber regenerator was investigated but abandoned due to manufacturability and reliability issues.

System level modeling gives detailed insight into the regenerator operation. Matching the measured pressure amplitudes and phases in addition to the measured net refrigeration with the system level model allows the regenerator boundary conditions to be extracted.

The steady, compressible flow friction factor measurement using an analytical solution matches with that measured in oscillating flow. The higher friction factor is apparently due to the velocity acceleration which occurs with a gas flowing through a porous media at high Reynolds number; it does not appear to depend on the flow unsteadiness which several investigators have claimed.

6.2 Contributions

Beginning with the most significant contributions first, the application of the volume averaging technique to the regenerator problem is the most noteworthy. This approach removes the ambiguity which has existed in the regenerator literature for decades. While the simplifications which were made reduce the problem to a similar formulation found in the literature, the framework for future refinements and investigations are solidly laid.

The numerical solution of the one dimensional model using a conservative scheme is a significant contribution. This method is more accurate and reliable than any existing method in the open literature due to the direct solution of a conservative system of equations with a conservative numerical scheme. The lack of assumptions make this model a test case for other models such as REGEN and Sage. Sage is a valuable system level model, but the regenerator poses the largest source of irreversibility in the entire cryocooler system. As a result, any inaccuracies in the regenerator can manifest themselves as large net refrigeration errors. Having an accurate prediction tool allows the Sage model to be verified.

The test apparatus and accompanying data acquisition system represents six years of effort. The diagnostic capability of the system allows for real time data analysis. Optimizing the cryocooler operation is assisted by data averaging, filtering, and trending. Troubleshooting is much improved. With the addition of the Sage system level modeling tool, experimentation and simulation can occur simultaneously giving the researcher the ability to immediately understand the effect of a change in the operating conditions.

6.3 Future Work

The volume-averaged equations were simplified in a manner which reduced the macroscopic equations to a form which could be solved. The form of the surface integrals representing the friction factor and heat transfer correlations reduced to familiar forms. The strict assumptions under which these simplifications are allowed may not be exactly true in the case of fully compressible flow with the large temperature and density variations which are observed in the regenerator. A possible discrepancy which the simplifications produce is due to the flow reversals which are occurring in the regenerator. Investigators have long supposed that the friction factor and heat transfer correlations from steady measurements deviate for oscillating flow. While it is more likely that the friction factor depends only on the microscale geometry, direct, pore-scale numerical simulations could be made to evaluate the surface integrals and assess the effect of the flow oscillations. These types of simulations have been made for steady flow, but none have been seen in the literature for oscillating, or even unsteady, flow. A demonstration calculation was performed using Fluent, which is a commercially available computational fluid dynamics software suite. The simulation consisted of constructing a solid model for a representative, periodic cell of the porous media, in this case wire mesh. A steady flow through the mesh was then simulated. Figure 49 and Figure 50 show some preliminary results of this type of simulation. These simulations were performed for steady flow only. Oscillating flow simulations are eventually a possibility.

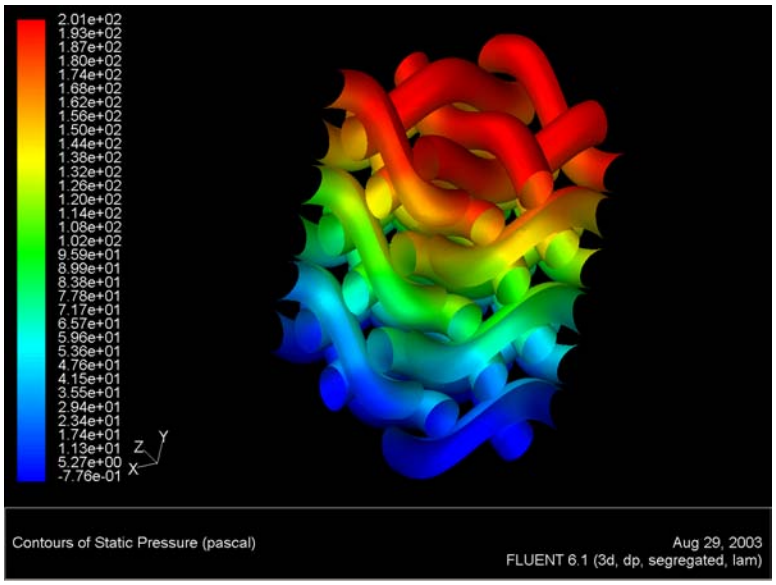

Figure 49 - Demonstration calculation for flow through wire mesh screens. Visualization of surface pressure

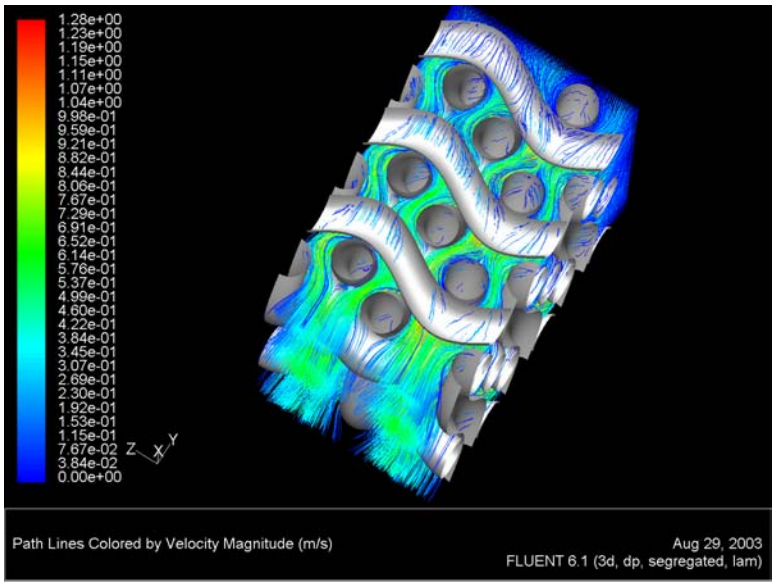

Figure 50 – Demonstration calculation for flow through wire mesh screens. Visualization of pathlines.

The surface and volume integrals representing the friction factor, heat transfer coefficient and dispersion coefficient can be evaluated knowing the pore scale flow. More importantly, oscillating flow and heat transfer can be modeled.

Admittedly, the heat transfer coefficient does depend on the flow, especially the frequency. For "significantly high" frequencies, Newton's Law of Cooling fails to hold due to significant phase shifting between the bulk temperature and the interfacial temperature. Kornhauser and Smith made this realization and adopted a complex Nusselt number to model this phenomenon. In light of the Reynold's Analogy, the friction factor may also exhibit a similar effect at some frequency limit.

The macroscopic regenerator flow is commonly assumed to be one-dimensional although several investigators have noticed definite deviations. The flow passage geometry leading into the regenerator will typically create a jet. The jet should be dispersed rapidly, but it is not possible at this point to model such a phenomenon. Small aspect ratio regenerators have lead to thermal instability problems producing, apparently, stagnation zones due to flow asymmetry. These deviations are assumed to dramatically deteriorate the regenerator performance. Proper system design should alleviate these problems, but a model capable of capturing these effects would be useful. Such a model would require, as a minimum, an additional radial coordinate. For most random media, the friction factor could be assumed, initially, to be constant in the radial direction. For such a model, the wall boundary conditions would need to be established. The radial velocity would obviously be zero at the wall, but the axial velocity does not have an obvious boundary condition at the wall (if one is required at all.) This needs to be studied carefully.

Several improvements to the test apparatus will represent a significant augmentation in ability to research more advanced concepts. Improved instrumentation

such as piezoelectric pressure transducers will greatly affect the reliability of the test results. These piezoelectric pressure transducers which do not require the repeated calibration and are less affected by temperature can be used in the cryogenic regions of the cooler allowing for direct measurement of the pressure. This is increasingly important for multistage cryocoolers. Anemometers can be designed with low helium leakage and can be operated in cryogenic regions as well providing mass flow and temperature measurements. A larger vacuum dewar will allow for calorimetric heat exchanger measurements to be made which will provide better system level understanding. It is possible to make modular components such as regenerators, pulse tubes, heat exchangers, instrumentation blocks, inertance tubes, surge volumes, etc. This gives more flexibility to investigate new concepts without redesigning the entire system. Compressor LVDTs are a necessity for continued testing. These LVDTs are used to measure the piston position as a function of time. With this information, the mechanical input PV power can be calculated. This is an important piece of data not currently available.

APPENDIX 1 – DERIVATION OF THE VOLUME-AVERAGED GOVERNING EQUATIONS

A1.1 Volume Averaging Theory

The method of volume averaging is applied to the governing equations for flow in a porous media. At the outset, the averaging theorems and principles are discussed. The generalized governing equations of mass conservation, momentum balance and energy conservation are developed for a single fluid phase flowing and interacting with a single stationary solid (matrix) phase. The only assumptions that are made initially are that the two phases do not react chemically with eachother and that the no-slip assumption at the fluid-solid interface is valid.

A1.1.1 Definitions

Within a porous media, an arbitrarily given volume, V, can contain portions of different phases of material. Consider for example, a porous media with a single fluid phase, α, and a single solid phase, β such as the system illustrated in Figure 4. Then the total volume, V(t) is given as

$$V(t) = V_\alpha(t) + V_\beta(t). \qquad \textbf{(A1-1)}$$

A property in the α-phase, ω_α, at a given position, x, in the porous media is written as a function of space and time as

$$\omega_\alpha(x_\alpha,t)=\omega_\alpha,$$
$$\omega_\alpha(x_\beta,t)=0. \qquad \textbf{(A1-2)}$$

where the subscript on the position vector indicates the phase at that position.

The *phase average* of a property is defined as the volumetric average over the total volume. Explicitly, the phase average is

$$\langle\omega_\alpha\rangle=\frac{1}{V}\int_V \omega_\alpha dV. \qquad \textbf{(A1-3)}$$

The *intrinsic phase average* is the volumetric average of a property over the phase volume, i.e.

$$\langle\omega_\alpha\rangle^\alpha=\frac{1}{V_\alpha}\int_V \omega_\alpha dV=\frac{1}{V_\alpha}\left[\int_{V_\alpha}\omega_\alpha dV+\underbrace{\int_{V_\beta}\omega_\alpha dV}_{=0}\right]=\frac{1}{V_\alpha}\int_{V_\alpha}\omega_\alpha dV. \qquad \textbf{(A1-4)}$$

By defining the volume fraction or *porosity* of the β-phase, ε_α, as

$$\varepsilon_\alpha=\frac{V_\alpha}{V}, \qquad \textbf{(A1-5)}$$

the phase average and intrinsic phase average can be related by

$$\langle\omega_\alpha\rangle=\varepsilon_\alpha\langle\omega_\alpha\rangle^\alpha. \qquad \textbf{(A1-6)}$$

To transform the governing equations of mass, momentum, and energy for the porous media, it is necessary to note a few theorems that relate averages of derivatives to derivatives of averages. These theorems are given without proof. The reader is referred to the literature for proofs of these theorems (67, 68).

A1.1.2 Transport Theorem

The volume average of a temporal derivative is related to the temporal derivative of an average by the Transport Theorem given by

$$\left\langle \frac{\partial \omega_\alpha}{\partial t} \right\rangle = \frac{\partial}{\partial t}\langle \omega_\alpha \rangle - \frac{1}{V}\int_{A_{\alpha\beta}} \omega_\alpha w_{\alpha\beta} \cdot n_\alpha dS \qquad \textbf{(A1-7)}$$

where $A_{\alpha\beta}$ is the area of the α-β interface in V, $w_{\alpha\beta}$ is the velocity of the α-β interfacial surface in V, and n_α is the unit normal vector on the α-β interface pointing into the β-phase. If the no-slip assumption is valid, then

$$v_\alpha\big|_{A_{\alpha\beta}} = v_\beta\big|_{A_{\alpha\beta}} \Rightarrow w_{\alpha\beta} = 0 \qquad \textbf{(A1-8)}$$

This result requires the surface integral in Equation (A2-7) to be zero, and this leads to a simplified transport theorem valid for a no-slip porous media given by

$$\left\langle \frac{\partial \omega_\alpha}{\partial t} \right\rangle = \frac{\partial}{\partial t}\langle \omega_\alpha \rangle. \qquad \textbf{(A1-9)}$$

A1.1.3 Spatial Averaging Theorem

The volume average of a spatial derivative is related to the spatial derivative of an average by the Spatial Averaging Theorem given by

$$\langle \nabla \omega_\alpha \rangle = \nabla \langle \omega_\alpha \rangle + \frac{1}{V}\int_{A_{\alpha\beta}} n_\alpha \omega_\alpha dS. \qquad \textbf{(A1-10)}$$

This transformation generates an additional term represented by the surface integral even for a no-slip porous media. This additional term represents a macroscopic contribution caused be the microscopic interaction of the two phases.

A1.1.4 Modified Averaging Theorem

Equation (A2-10) can be modified by application of Equation (A2-6). Note that

$$\begin{aligned}\langle \nabla \omega_\alpha \rangle &= \nabla\left(\varepsilon_\alpha \langle \omega_\alpha \rangle^\alpha\right) + \frac{1}{V}\int_{A_{\alpha\beta}} n_\alpha \omega_\alpha dS \\ &= \varepsilon_\alpha \nabla \langle \omega_\alpha \rangle^\alpha + \langle \omega_\alpha \rangle^\alpha \nabla \varepsilon_\alpha + \frac{1}{V}\int_{A_{\alpha\beta}} n_\alpha \left(\langle \omega_\alpha \rangle^\alpha + \hat{\omega}_\alpha\right) dS \\ &= \varepsilon_\alpha \nabla \langle \omega_\alpha \rangle^\alpha + \langle \omega_\alpha \rangle^\alpha \nabla \varepsilon_\alpha + \frac{1}{V}\int_{A_{\alpha\beta}} n_\alpha \langle \omega_\alpha \rangle^\alpha dS + \frac{1}{V}\int_{A_{\alpha\beta}} n_\alpha \hat{\omega}_\alpha dS\end{aligned} \tag{A1-11}$$

where $\hat{\omega}_\alpha$ is the deviation of ω_α from its intrinsic phase average defined by

$$\hat{\omega}_\alpha = \omega_\alpha - \langle \omega_\alpha \rangle^\alpha. \tag{A1-12}$$

The intrinsic average that appears in the first surface integral is essentially constant over the surface (42). As a result, the intrinsic average can be removed from the surface integral giving

$$\begin{aligned}\langle \nabla \omega_\alpha \rangle &= \varepsilon_\alpha \nabla \langle \omega_\alpha \rangle^\alpha + \langle \omega_\alpha \rangle^\alpha \nabla \varepsilon_\alpha + \langle \omega_\alpha \rangle^\alpha \underbrace{\frac{1}{V}\int_{A_{\alpha\beta}} n_\alpha dS}_{-\nabla \varepsilon_\alpha} + \frac{1}{V}\int_{A_{\alpha\beta}} n_\alpha \hat{\omega}_\alpha dS \\ &= \varepsilon_\alpha \nabla \langle \omega_\alpha \rangle^\alpha + \frac{1}{V}\int_{A_{\alpha\beta}} n_\alpha \hat{\omega}_\alpha dS\end{aligned} \tag{A1-13}$$

This leads to the Modified Averaging Theorem given by

$$\langle \nabla \omega_\alpha \rangle = \varepsilon_\alpha \nabla \langle \omega_\alpha \rangle^\alpha + \frac{1}{V}\int_{A_{\alpha\beta}} n_\alpha \hat{\omega}_\alpha dS \tag{A1-14}$$

This is referred to as the scale decomposition since the parameter is decomposed into a macroscopic and microscopic component. Note that several consequences arise from this

term. First, in the α-phase, the deviation can be non-zero, but in the β-phase, this term is identically zero by Equation (A2-2). Also note that

$$\left\langle \hat{\omega}_\alpha \right\rangle = \left\langle \hat{\omega}_\alpha \right\rangle^\alpha = 0. \tag{A1-15}$$

These principles and theorems can now be applied to the governing equations to develop a generalized set of averaged governing equations.

A1.2 Application to the Governing Equations

The preceding volume averaging theorems can now be applied to the governing equations. In doing so, the continuum flow which exists at the microscopic level is transformed into a continuum flow at the macroscopic level. The result is the production of various terms representing the microscale influence on the macroscopic flow.

A1.2.1 Volume-Averaged Conservation of Mass Equation

The phase average of Equation (2-13) is

$$\left\langle \frac{\partial \rho_\alpha}{\partial t} \right\rangle + \left\langle \nabla \cdot \left(\rho_\alpha \vec{u}_\alpha \right) \right\rangle = 0. \tag{A1-16}$$

In developing this volume-averaged equation, we will assume that the no-slip assumption is valid at the fluid solid interface. We will also neglect gradients in the porosity. Application of the Transport Theorem (A2-9) to the first term in Equation (A2-16) yields

$$\left\langle \frac{\partial \rho_\alpha}{\partial t} \right\rangle = \frac{\partial}{\partial t} \left\langle \rho_\alpha \right\rangle. \tag{A1-17}$$

Definition (A2-6) can be used to obtain

$$\left\langle \frac{\partial \rho_\alpha}{\partial t} \right\rangle = \varepsilon_\alpha \frac{\partial}{\partial t} \langle \rho_\alpha \rangle^\alpha . \qquad \textbf{(A1-18)}$$

Application of the Averaging Theorem (A2-10) to the second term in Equation (A2-16) yields

$$\langle \nabla \cdot (\rho_\alpha \vec{u}_\alpha) \rangle = \nabla \cdot \langle \rho_\alpha \vec{u}_\alpha \rangle + \frac{1}{V} \int_{A_{\alpha\beta}} n_\alpha \cdot \rho_\alpha \vec{u}_\alpha dS. \qquad \textbf{(A1-19)}$$

The surface integral in the last equation evaluates to zero due to the no slip assumption reducing the equation to

$$\langle \nabla \cdot (\rho_\alpha \vec{u}_\alpha) \rangle = \nabla \cdot \langle \rho_\alpha \vec{u}_\alpha \rangle. \qquad \textbf{(A1-20)}$$

Definitions (A2-12) and (A2-15) can be used to obtain

$$\langle \nabla \cdot (\rho_\alpha \vec{u}_\alpha) \rangle = \varepsilon_\alpha \nabla \cdot \left(\langle \rho_\alpha \rangle^\alpha \langle \vec{u}_\alpha \rangle^\alpha \right) + \nabla \cdot \langle \hat{\rho}_\alpha \hat{\vec{u}}_\alpha \rangle. \qquad \textbf{(A1-21)}$$

Thus, the volume-averaged continuity equation becomes

$$\underbrace{\frac{\partial}{\partial t} \langle \rho_\alpha \rangle^\alpha}_{accumulation} + \underbrace{\nabla \cdot \left(\langle \rho_\alpha \rangle^\alpha \langle \vec{u}_\alpha \rangle^\alpha \right)}_{convection} + \underbrace{\frac{1}{\varepsilon_\alpha} \nabla \cdot \langle \hat{\rho}_\alpha \hat{\vec{u}}_\alpha \rangle}_{mass\,dispersion} = 0. \qquad \textbf{(A1-22)}$$

This volume-averaged form of the continuity equation contains an additional term which was not in the point equations. This term represents the dispersive mass transport. This is a generalized continuity equation for 3-D flow in a porous media. The momentum equation can be averaged in the same manner.

A1.2.2 Volume-Averaged Balance of Momentum Equation

The phase average of Equation (2-14) is

$$\left\langle \frac{\partial}{\partial t}\left(\rho_\alpha \vec{u}_\alpha\right)\right\rangle + \left\langle \nabla\cdot\left(\rho_\alpha \vec{u}_\alpha \vec{u}_\alpha\right)\right\rangle + \left\langle \nabla p_\alpha \right\rangle - \left\langle \frac{1}{3}\nabla\left(\mu_\alpha \nabla\cdot\vec{u}_\alpha\right)\right\rangle - \left\langle \nabla\cdot\left(\mu_\alpha \nabla\vec{u}_\alpha\right)\right\rangle = 0. \qquad \textbf{(A1-23)}$$

As with the continuity equation, we will assume that the no-slip assumption is valid and that gradients of the porosity are negligible. Application of the Transport Theorem (A2-10) to the first term in Equation (A2-23) yields

$$\left\langle \frac{\partial}{\partial t}\left(\rho_\alpha \vec{u}_\alpha\right)\right\rangle = \frac{\partial}{\partial t}\left\langle \rho_\alpha \vec{u}_\alpha \right\rangle. \qquad \textbf{(A1-24)}$$

Definitions (A2-12) and (A2-15) can be used to obtain

$$\left\langle \rho_\alpha \vec{u}_\alpha \right\rangle = \varepsilon_\alpha \left\langle \rho_\alpha \right\rangle^\alpha \left\langle \vec{u}_\alpha \right\rangle^\alpha + \left\langle \hat{\rho}_\alpha \hat{\vec{u}}_\alpha \right\rangle. \qquad \textbf{(A1-25)}$$

Substitution of Equation (A2-25) into Equation (A2-24) yields

$$\left\langle \frac{\partial}{\partial t}\left(\rho_\alpha \vec{u}_\alpha\right)\right\rangle = \varepsilon_\alpha \frac{\partial}{\partial t}\left(\left\langle \rho_\alpha \right\rangle^\alpha \left\langle \vec{u}_\alpha \right\rangle^\alpha\right) + \frac{\partial}{\partial t}\left\langle \hat{\rho}_\alpha \hat{\vec{u}}_\alpha \right\rangle. \qquad \textbf{(A1-26)}$$

The Averaging Theorem (A2-10) can be applied to the second term in Equation (A2-23) to obtain

$$\left\langle \nabla\cdot\left(\rho_\alpha \vec{u}_\alpha \vec{u}_\alpha\right)\right\rangle = \nabla\cdot\left\langle \rho_\alpha \vec{u}_\alpha \vec{u}_\alpha \right\rangle. \qquad \textbf{(A1-27)}$$

Definitions (A2-12) and (A2-15) can be used to expand $\left\langle \rho_\alpha \vec{u}_\alpha \vec{u}_\alpha \right\rangle$ to the form

$$\begin{aligned}\left\langle \rho_\alpha \vec{u}_\alpha \vec{u}_\alpha \right\rangle = \varepsilon_\alpha \left\langle \rho_\alpha \right\rangle^\alpha \left\langle \vec{u}_\alpha \right\rangle^\alpha \left\langle \vec{u}_\alpha \right\rangle^\alpha + \left\langle \rho_\alpha \right\rangle^\alpha \left\langle \hat{\vec{u}}_\alpha \hat{\vec{u}}_\alpha \right\rangle + \left\langle \vec{u}_\alpha \right\rangle^\alpha \left\langle \hat{\rho}_\alpha \hat{\vec{u}}_\alpha \right\rangle \\ + \left\langle \hat{\rho}_\alpha \hat{\vec{u}}_\alpha \right\rangle \left\langle \vec{u}_\alpha \right\rangle^\alpha + \left\langle \hat{\rho}_\alpha \hat{\vec{u}}_\alpha \hat{\vec{u}}_\alpha \right\rangle.\end{aligned} \qquad \textbf{(A1-28)}$$

Thus Equation (A2-27) becomes

$$\left\langle \nabla \cdot \left(\rho_\alpha \vec{u}_\alpha \vec{u}_\alpha \right) \right\rangle = \varepsilon_\alpha \nabla \cdot \left(\left\langle \rho_\alpha \right\rangle^\alpha \left\langle \vec{u}_\alpha \right\rangle^\alpha \left\langle \vec{u}_\alpha \right\rangle^\alpha \right) + \nabla \cdot \left(\left\langle \rho_\alpha \right\rangle^\alpha \left\langle \hat{\vec{u}}_\alpha \hat{\vec{u}}_\alpha \right\rangle \right) + \nabla \cdot \left(\left\langle \vec{u}_\alpha \right\rangle^\alpha \left\langle \hat{\rho}_\alpha \hat{\vec{u}}_\alpha \right\rangle \right) + \nabla \cdot \left(\left\langle \hat{\rho}_\alpha \hat{\vec{u}}_\alpha \right\rangle \left\langle \vec{u}_\alpha \right\rangle^\alpha \right) + \nabla \cdot \left\langle \hat{\rho}_\alpha \hat{\vec{u}}_\alpha \hat{\vec{u}}_\alpha \right\rangle. \quad \textbf{(A1-29)}$$

The Modified Averaging Theorem (A2-14) can be applied to the third term in Equation (A2-23) to produce

$$\left\langle \nabla p_\alpha \right\rangle = \varepsilon_\alpha \nabla \left\langle p_\alpha \right\rangle^\alpha + \frac{1}{V} \int_{A_{\alpha\beta}} n_\alpha \hat{p}_\alpha dS. \quad \textbf{(A1-30)}$$

Now proceed to expand the viscous terms in Equation (A2-23). The viscosity can be considered to be constant within the averaging volume, and the last term in Equation (A2-23) can be written as

$$\left\langle \nabla \cdot \left(\mu_\alpha \nabla \vec{u}_\alpha \right) \right\rangle = \nabla \cdot \left(\mu_\alpha \left\langle \nabla \vec{u}_\alpha \right\rangle \right) + \frac{1}{V} \int_{A_{\alpha\beta}} \mu_\alpha n_\alpha \cdot \nabla \vec{u}_\alpha dS. \quad \textbf{(A1-31)}$$

Applying the modified averaging theorem again produces

$$\left\langle \nabla \cdot \left(\mu_\alpha \nabla \vec{u}_\alpha \right) \right\rangle = \nabla \cdot \left(\mu_\alpha \left[\varepsilon_\alpha \nabla \left\langle \vec{u}_\alpha \right\rangle^\alpha + \frac{1}{V} \int_{A_{\alpha\beta}} n_\alpha \hat{\vec{u}}_\alpha dS \right] \right) + \frac{1}{V} \int_{A_{\alpha\beta}} \mu_\alpha n_\alpha \cdot \nabla \vec{u}_\alpha dS. \quad \textbf{(A1-32)}$$

Again the surface integral, $\frac{1}{V} \int_{A_{\alpha\beta}} n_\alpha \hat{\vec{u}}_\alpha dS$, evaluates to zero by the no-slip assumption which simplifies the last equation to

$$\left\langle \nabla \cdot \left(\mu_\alpha \nabla \vec{u}_\alpha \right) \right\rangle = \varepsilon_\alpha \nabla \cdot \left(\mu_\alpha \nabla \left\langle \vec{u}_\alpha \right\rangle^\alpha \right) + \frac{1}{V} \int_{A_{\alpha\beta}} \mu_\alpha n_\alpha \cdot \nabla \vec{u}_\alpha dS \quad \textbf{(A1-33)}$$

which can be expanded to

$$\left\langle \nabla \cdot \left(\mu_\alpha \nabla \vec{u}_\alpha \right) \right\rangle = \varepsilon_\alpha \nabla \cdot \left(\mu_\alpha \nabla \left\langle \vec{u}_\alpha \right\rangle^\alpha \right) + \frac{1}{V} \int_{A_{\alpha\beta}} \mu_\alpha n_\alpha \cdot \nabla \left\langle \vec{u}_\alpha \right\rangle^\alpha dS + \frac{1}{V} \int_{A_{\alpha\beta}} \mu_\alpha n_\alpha \cdot \nabla \hat{\vec{u}}_\alpha dS. \tag{A1-34}$$

The first surface integral also evaluates to zero if the porosity is constant. The final form of the viscous term is

$$\left\langle \nabla \cdot \left(\mu_\alpha \nabla \vec{u}_\alpha \right) \right\rangle = \varepsilon_\alpha \nabla \cdot \left(\mu_\alpha \nabla \left\langle \vec{u}_\alpha \right\rangle^\alpha \right) + \frac{1}{V} \int_{A_{\alpha\beta}} \mu_\alpha n_\alpha \cdot \nabla \hat{\vec{u}}_\alpha dS. \tag{A1-35}$$

The compressible viscous term in Equation (A2-23) can similarly be expanded to

$$\frac{1}{3} \left\langle \nabla \left(\mu_\alpha \nabla \cdot \vec{u}_\alpha \right) \right\rangle = \frac{\varepsilon_\alpha}{3} \nabla \left(\mu_\alpha \nabla \cdot \left\langle \vec{u}_\alpha \right\rangle^\alpha \right) + \frac{1}{V} \int_{A_{\alpha\beta}} \frac{\mu_\alpha}{3} n_\alpha \nabla \cdot \hat{\vec{u}}_\alpha dS. \tag{A1-36}$$

Substitution of Equations (A2-26), (A2-29), (A2-30), (A2-36), and (A2-34) into Equation (A2-23) yields

$$\begin{aligned} &\frac{\partial}{\partial t} \left(\left\langle \rho_\alpha \right\rangle^\alpha \left\langle \vec{u}_\alpha \right\rangle^\alpha \right) + \nabla \cdot \left(\left\langle \rho_\alpha \right\rangle^\alpha \left\langle \vec{u}_\alpha \right\rangle^\alpha \left\langle \vec{u}_\alpha \right\rangle^\alpha \right) + \nabla \left\langle p_\alpha \right\rangle^\alpha - \frac{1}{3} \nabla \left(\mu_\alpha \nabla \cdot \left\langle \vec{u}_\alpha \right\rangle^\alpha \right) - \nabla \cdot \left(\mu_\alpha \nabla \left\langle \vec{u}_\alpha \right\rangle^\alpha \right) \\ &+ \frac{1}{V_\alpha} \int_{A_{\alpha\beta}} n_\alpha \cdot \left[\tilde{I} \left(\hat{p}_\alpha - \frac{\mu_\alpha}{3} \nabla \cdot \hat{\vec{u}}_\alpha \right) - \mu_\alpha \nabla \hat{\vec{u}}_\alpha \right] dS \\ &+ \frac{1}{\varepsilon_\alpha} \frac{\partial}{\partial t} \left\langle \hat{\rho}_\alpha \hat{\vec{u}}_\alpha \right\rangle + \frac{1}{\varepsilon_\alpha} \nabla \cdot \left(\left\langle \rho_\alpha \right\rangle^\alpha \left\langle \hat{\vec{u}}_\alpha \hat{\vec{u}}_\alpha \right\rangle \right) + \frac{1}{\varepsilon_\alpha} \nabla \cdot \left(\left\langle \vec{u}_\alpha \right\rangle^\alpha \left\langle \hat{\rho}_\alpha \hat{\vec{u}}_\alpha \right\rangle \right) \\ &+ \frac{1}{\varepsilon_\alpha} \nabla \cdot \left(\left\langle \hat{\rho}_\alpha \hat{\vec{u}}_\alpha \right\rangle \left\langle \vec{u}_\alpha \right\rangle^\alpha \right) + \frac{1}{\varepsilon_\alpha} \nabla \cdot \left\langle \hat{\rho}_\alpha \hat{\vec{u}}_\alpha \hat{\vec{u}}_\alpha \right\rangle = 0. \end{aligned} \tag{A1-37}$$

In the last step, three surface integrals were combined and the whole equation was divided by porosity. We can take advantage of the continuity equation (A2-22) to re-write the momentum equation in weak conservation form as

$$\begin{aligned}
&\langle\rho_\alpha\rangle^\alpha \frac{\partial}{\partial t}\langle\vec{u}_\alpha\rangle^\alpha + \langle\rho_\alpha\rangle^\alpha\langle\vec{u}_\alpha\rangle^\alpha\cdot\nabla\langle\vec{u}_\alpha\rangle^\alpha + \nabla\langle p_\alpha\rangle^\alpha - \frac{1}{3}\nabla\left(\mu_\alpha\nabla\cdot\langle\vec{u}_\alpha\rangle^\alpha\right) - \nabla\cdot\left(\mu_\alpha\nabla\langle\vec{u}_\alpha\rangle^\alpha\right)\\
&+\frac{1}{V_\alpha}\int_{A_{\alpha\beta}} n_\alpha\cdot\left[\tilde{I}\left(\hat{p}_\alpha - \frac{\mu_\alpha}{3}\nabla\cdot\hat{\vec{u}}_\alpha\right) - \mu_\alpha\nabla\hat{\vec{u}}_\alpha\right]dS\\
&+\frac{1}{\varepsilon_\alpha}\frac{\partial}{\partial t}\left\langle\hat{\rho}_\alpha\hat{\vec{u}}_\alpha\right\rangle + \frac{1}{\varepsilon_\alpha}\nabla\cdot\left(\langle\rho_\alpha\rangle^\alpha\left\langle\hat{\vec{u}}_\alpha\hat{\vec{u}}_\alpha\right\rangle\right) + \frac{1}{\varepsilon_\alpha}\nabla\cdot\left(\langle\vec{u}_\alpha\rangle^\alpha\left\langle\hat{\rho}_\alpha\hat{\vec{u}}_\alpha\right\rangle\right)\\
&+\frac{1}{\varepsilon_\alpha}\left\langle\hat{\rho}_\alpha\hat{\vec{u}}_\alpha\right\rangle\cdot\nabla\langle\vec{u}_\alpha\rangle^\alpha + \frac{1}{\varepsilon_\alpha}\nabla\cdot\left\langle\hat{\rho}_\alpha\hat{\vec{u}}_\alpha\hat{\vec{u}}_\alpha\right\rangle = 0.
\end{aligned} \tag{A1-38}$$

A1.2.3 Volume-Averaged α-Phase Conservation of Energy Equation

The phase average of Equation (2-15) is

$$\left\langle\frac{\partial(\rho_\alpha e_\alpha)}{\partial t}\right\rangle + \left\langle\nabla\cdot\left(\rho_\alpha\vec{u}_\alpha h_\alpha\right)\right\rangle - \left\langle\nabla\cdot\left(k_\alpha\nabla T_\alpha\right)\right\rangle = 0. \tag{A1-39}$$

The same assumptions for no-slip and gradients of porosity will be applied to the energy equation as well. Application of the averaging theorems to the accumulation term in Equation (A2-39) yields

$$\begin{aligned}
\left\langle\frac{\partial(\rho_\alpha e_\alpha)}{\partial t}\right\rangle &= \frac{\partial\langle\rho_\alpha e_\alpha\rangle}{\partial t}\\
&= \varepsilon_\alpha\frac{\partial\left(\langle\rho_\alpha\rangle^\alpha\langle e_\alpha\rangle^\alpha\right)}{\partial t} + \frac{\partial\langle\hat{\rho}_\alpha\hat{e}_\alpha\rangle}{\partial t}.
\end{aligned} \tag{A1-40}$$

Application of the averaging theorems to the convection term in Equation (A2-39) yields

$$\begin{aligned}
\left\langle\nabla\cdot\left(\rho_\alpha\vec{u}_\alpha h_\alpha\right)\right\rangle = \varepsilon_\alpha\nabla\cdot\left(\langle\rho_\alpha\rangle^\alpha\langle\vec{u}_\alpha\rangle^\alpha\langle h_\alpha\rangle^\alpha\right) &+ \nabla\cdot\left(\left\langle\hat{\rho}_\alpha\hat{\vec{u}}_\alpha\right\rangle\langle h_\alpha\rangle^\alpha\right) + \nabla\cdot\left(\langle\rho_\alpha\rangle^\alpha\left\langle\hat{\vec{u}}_\alpha\hat{h}_\alpha\right\rangle\right)\\
&+\nabla\cdot\left(\left\langle\hat{\rho}_\alpha\hat{\vec{u}}_\alpha\right\rangle\langle h_\alpha\rangle^\alpha\right) + \nabla\cdot\left\langle\hat{\rho}_\alpha\hat{\vec{u}}_\alpha\hat{h}_\alpha\right\rangle.
\end{aligned} \tag{A1-41}$$

Finally, the conduction term in Equation (A2-39) can be simplified to

$$-\left\langle \nabla\cdot\left(k_\alpha \nabla T_\alpha\right)\right\rangle = -\nabla\cdot\left[k_\alpha\left\langle \nabla T_\alpha\right\rangle\right] - \frac{1}{V}\int_{A_{\alpha\beta}} n_\alpha \cdot k_\alpha \nabla T_\alpha dS$$
$$= -\nabla\cdot\left[k_\alpha\left(\varepsilon_\alpha \nabla\left\langle T_\alpha\right\rangle^\alpha + \frac{1}{V}\int_{A_{\alpha\beta}} n_\alpha \hat{T}_\alpha dS\right)\right] - \frac{1}{V}\int_{A_{\alpha\beta}} n_\alpha \cdot k_\alpha \nabla T_\alpha dS. \quad \textbf{(A1-42)}$$

The last step in Equation (A2-42) involves decomposing the point temperature according to the decomposition definition. Substituting Equations (A2-40), (A2-41), and (A2-42) into Equation (A2-39) gives

$$\frac{\partial\left(\left\langle \rho_\alpha\right\rangle^\alpha\left\langle e_\alpha\right\rangle^\alpha\right)}{\partial t} + \nabla\cdot\left(\left\langle \rho_\alpha\right\rangle^\alpha\left\langle \vec{u}_\alpha\right\rangle^\alpha\left\langle h_\alpha\right\rangle^\alpha\right) - \frac{1}{\varepsilon_\alpha}\nabla\cdot\left[k_\alpha\left(\varepsilon_\alpha\nabla\left\langle T_\alpha\right\rangle^\alpha + \frac{1}{V}\int_{A_{\alpha\beta}} n_\alpha\hat{T}_\alpha dS\right)\right]$$
$$-\frac{1}{\varepsilon_\alpha}\frac{1}{V}\int_{A_{\alpha\beta}} n_\alpha\cdot k_\alpha\nabla T_\alpha dS + \frac{1}{\varepsilon_\alpha}\frac{\partial\left\langle \hat{\rho}_\alpha\hat{e}_\alpha\right\rangle}{\partial t} + \frac{1}{\varepsilon_\alpha}\nabla\cdot\left(\left\langle \hat{\rho}_\alpha\hat{\vec{u}}_\alpha\right\rangle\left\langle h_\alpha\right\rangle^\alpha\right) \quad \textbf{(A1-43)}$$
$$+\frac{1}{\varepsilon_\alpha}\nabla\cdot\left(\left\langle \rho_\alpha\right\rangle^\alpha\left\langle \hat{\vec{u}}_\alpha\hat{h}_\alpha\right\rangle\right) + \frac{1}{\varepsilon_\alpha}\nabla\cdot\left(\left\langle \hat{\rho}_\alpha\hat{\vec{u}}_\alpha\right\rangle\left\langle h_\alpha\right\rangle^\alpha\right) + \frac{1}{\varepsilon_\alpha}\nabla\cdot\left\langle \hat{\rho}_\alpha\hat{\vec{u}}_\alpha\hat{h}_\alpha\right\rangle = 0.$$

A1.2.4 Volume-Averaged β-Phase Conservation of Energy Equation

The phase average of Equation (2-16) is

$$\left(\rho c_v\right)_\beta\left\langle\frac{\partial T_\beta}{\partial t}\right\rangle - \left\langle\nabla\cdot\left(k_\beta\nabla T_\beta\right)\right\rangle = 0 \quad \textbf{(A1-44)}$$

which can be readily simplified to

$$\left(\rho c_v\right)_\beta\frac{\partial\left\langle T_\beta\right\rangle^\beta}{\partial t} - \nabla\cdot\left[k_\beta\left(\nabla\left\langle T_\beta\right\rangle^\beta + \frac{1}{V_\beta}\int_{A_{\alpha\beta}} n_\beta\hat{T}_\beta dS\right)\right]$$
$$-\frac{1}{V_\beta}\int_{A_{\alpha\beta}} n_\beta\cdot k_\beta\nabla T_\beta dS = 0. \quad \textbf{(A1-45)}$$

A1.2.5 Volume-Averaged α-Phase Entropy Generation Equation

The phase average of Equation (2-17) is

$$\left\langle s'''_{gen,\alpha} \right\rangle = \left\langle \frac{\partial(\rho_\alpha s_\alpha)}{\partial t} \right\rangle + \left\langle \nabla \cdot (\rho_\alpha s_\alpha \vec{u}_\alpha) \right\rangle + \left\langle \nabla \cdot \left(\frac{\vec{q}_\alpha}{T_\alpha} \right) \right\rangle \geq 0. \tag{A1-46}$$

The first term on the right in Equation (A2-46) representing the time rate of change of entropy can be expanded to obtain

$$\begin{aligned} \left\langle \frac{\partial(\rho_\alpha s_\alpha)}{\partial t} \right\rangle &= \frac{\partial \langle \rho_\alpha s_\alpha \rangle}{\partial t} \\ &= \varepsilon_\alpha \frac{\partial \left(\langle \rho_\alpha \rangle^\alpha \langle s_\alpha \rangle^\alpha \right)}{\partial t} + \frac{\partial \langle \hat{\rho}_\alpha \hat{s}_\alpha \rangle}{\partial t}. \end{aligned} \tag{A1-47}$$

In developing this volume-averaged equation, the no-slip assumption is valid at the fluid solid interface. Gradients in the porosity will also be neglected. Now applying the averaging theorems to the second term on the right of Equation (A2-46) representing the convection of entropy gives

$$\begin{aligned} \langle \nabla \cdot (\rho_\alpha s_\alpha \vec{u}_\alpha) \rangle = \varepsilon_\alpha \nabla \cdot \left(\langle \rho_\alpha \rangle^\alpha \langle s_\alpha \rangle^\alpha \langle \vec{u}_\alpha \rangle^\alpha \right) + \nabla \cdot \left(\langle \hat{\rho}_\alpha \hat{s}_\alpha \rangle \langle \vec{u}_\alpha \rangle^\alpha \right) + \nabla \cdot \left(\langle \rho_\alpha \rangle^\alpha \left\langle \hat{s}_\alpha \hat{\vec{u}}_\alpha \right\rangle \right) \\ + \nabla \cdot \left(\left\langle \hat{\rho}_\alpha \hat{\vec{u}}_\alpha \right\rangle \langle s_\alpha \rangle^\alpha \right) + \nabla \cdot \left\langle \hat{\rho}_\alpha \hat{s}_\alpha \hat{\vec{u}}_\alpha \right\rangle. \end{aligned} \tag{A1-48}$$

Using Fourier's Law, the third term on the right of Equation (A2-46) can be expanded to

$$-\left\langle \nabla \cdot \left(\frac{k_\alpha \nabla T_\alpha}{T_\alpha} \right) \right\rangle = -\nabla \cdot \left[k_\alpha \left\langle \frac{\nabla T_\alpha}{T_\alpha} \right\rangle \right] - \frac{1}{V} \int_{A_{\alpha\beta}} n_\alpha \cdot \frac{k_\alpha \nabla T_\alpha}{T_\alpha} dS \tag{A1-49}$$

Substituting Equation (A2-47) through Equation (A2-49) into Equation (A2-46) produces

$$\left\langle s'''_{\alpha,gen}\right\rangle^{\alpha} = \frac{\partial\left(\left\langle\rho_\alpha\right\rangle^{\alpha}\left\langle s_\alpha\right\rangle^{\alpha}\right)}{\partial t} + \frac{1}{\varepsilon_\alpha}\frac{\partial\left\langle\hat{\rho}_\alpha\hat{s}_\alpha\right\rangle}{\partial t}$$
$$+\nabla\cdot\left(\left\langle\rho_\alpha\right\rangle^{\alpha}\left\langle s_\alpha\right\rangle^{\alpha}\left\langle\vec{u}_\alpha\right\rangle^{\alpha}\right)+\frac{1}{\varepsilon_\alpha}\nabla\cdot\left(\left\langle\hat{\rho}_\alpha\hat{s}_\alpha\right\rangle\left\langle\vec{u}_\alpha\right\rangle^{\alpha}\right)+\frac{1}{\varepsilon_\alpha}\nabla\cdot\left(\left\langle\rho_\alpha\right\rangle^{\alpha}\left\langle\hat{s}_\alpha\hat{\vec{u}}_\alpha\right\rangle\right)$$
$$+\frac{1}{\varepsilon_\alpha}\nabla\cdot\left(\left\langle\hat{\rho}_\alpha\hat{\vec{u}}_\alpha\right\rangle\left\langle s_\alpha\right\rangle^{\alpha}\right)+\frac{1}{\varepsilon_\alpha}\nabla\cdot\left\langle\hat{\rho}_\alpha\hat{s}_\alpha\hat{\vec{u}}_\alpha\right\rangle \qquad \textbf{(A1-50)}$$
$$-\frac{1}{\varepsilon_\alpha}\nabla\cdot\left[k_\alpha\left\langle\frac{\nabla T_\alpha}{T_\alpha}\right\rangle\right]-\frac{1}{V_\alpha}\int_{A_{\alpha\beta}} n_\alpha\cdot\frac{k_\alpha\nabla T_\alpha}{T_\alpha}\,dS$$

A1.2.6 Volume-Averaged β-Phase Entropy Generation Equation

The phase average of Equation (2-18) is

$$\left\langle s'''_{\beta,gen}\right\rangle = \left\langle\frac{\partial\left(\rho_\beta s_\beta\right)}{\partial t}\right\rangle + \left\langle\nabla\cdot\left(\frac{\vec{q}_\beta}{T_\beta}\right)\right\rangle \geq 0 \qquad \textbf{(A1-51)}$$

which can be readily expanded to

$$\left\langle s'''_{\beta,gen}\right\rangle^{\beta} = \rho_\beta\frac{\partial\left\langle s_\beta\right\rangle^{\beta}}{\partial t} - \frac{1}{\varepsilon_\beta}\nabla\cdot\left[k_\beta\left\langle\frac{\nabla T_\beta}{T_\beta}\right\rangle\right]-\frac{1}{V_\beta}\int_{A_{\alpha\beta}} n_\beta\cdot\frac{k_\beta\nabla T_\beta}{T_\beta}\,dS \qquad \textbf{(A1-52)}$$

The volume averaged equations have been developed in sufficiently generalized form. In the present form, the equations do not present a tractable problem. Eventually, these equations will be represented entirely in terms of volume averaged quantities. The details of this simplification are the subject of Chapter 2.

APPENDIX 2 – DERIVATION OF DIFFERENTIATION OPERATORS USING MATLAB

Spatial differentiation can be expressed as a linear operator using a variety of discrete differentiation schemes. In general, the i^{th} derivative of a quantity, a, can be calculated as

$$\left(\frac{\partial a}{\partial x}\right)_i \cong D_{ij} a_j \qquad \textbf{(A2-1)}$$

where D_{ij} is the linear differentiation operator. Higher order differentiation can be performed using either a higher order operator or via recursive operations, i.e

$$\left(\frac{\partial^2 a}{\partial x^2}\right)_i \cong D_{ij}\left(D_{jk} a_k\right) \qquad \textbf{(A2-2)}$$

These operators can be of variable order or method. In this research, it was found that central finite difference operators performed well due to the diffusive nature of the continuity equation. Second order central and fourth order central differences were employed. It was noticed that the second order central operators were more stable than fourth order, but the fourth order provided more accuracy. It is possible to construct upwind or biased difference operators. These gave little success for this problem.

Any finite difference operator can be constructed by forming a Taylor series expansion:

$$u_{i-n} = u_i + \frac{(-n\Delta x)^1}{1!}u_i^{(1)} + \frac{(-n\Delta x)^2}{2!}u_i^{(2)} + \frac{(-n\Delta x)^3}{3!}u_i^{(3)} + \frac{(-n\Delta x)^4}{4!}u_i^{(4)} + \ldots$$

$$\vdots$$

$$u_{i-2} = u_i + \frac{(-2\Delta x)^1}{1!}u_i^{(1)} + \frac{(-2\Delta x)^2}{2!}u_i^{(2)} + \frac{(-2\Delta x)^3}{3!}u_i^{(3)} + \frac{(-2\Delta x)^4}{4!}u_i^{(4)} + \ldots$$

$$u_{i-1} = u_i + \frac{(-1\Delta x)^1}{1!}u_i^{(1)} + \frac{(-1\Delta x)^2}{2!}u_i^{(2)} + \frac{(-1\Delta x)^3}{3!}u_i^{(3)} + \frac{(-1\Delta x)^4}{4!}u_i^{(4)} + \ldots$$

$$u_{i+1} = u_i + \frac{(+1\Delta x)^1}{1!}u_i^{(1)} + \frac{(+1\Delta x)^2}{2!}u_i^{(2)} + \frac{(+1\Delta x)^3}{3!}u_i^{(3)} + \frac{(+1\Delta x)^4}{4!}u_i^{(4)} + \ldots$$

$$u_{i+2} = u_i + \frac{(+2\Delta x)^1}{1!}u_i^{(1)} + \frac{(+2\Delta x)^2}{2!}u_i^{(2)} + \frac{(+2\Delta x)^3}{3!}u_i^{(3)} + \frac{(+2\Delta x)^4}{4!}u_i^{(4)} + \ldots$$

$$\vdots$$

$$u_{i+n} = u_i + \frac{(+n\Delta x)^1}{1!}u_i^{(1)} + \frac{(+n\Delta x)^2}{2!}u_i^{(2)} + \frac{(+n\Delta x)^3}{3!}u_i^{(3)} + \frac{(+n\Delta x)^4}{4!}u_i^{(4)} + \ldots \quad \textbf{(A2-3)}$$

By forming a truncated linear series, the desired operator can be created. For example, the three point central differences for the first and second derivative are formed by taking a linear series of the i+1 and i-1 points:

$$au_{i-1} = au_i + a\frac{(-1\Delta x)^1}{1!}u_i^{(1)} + a\frac{(-1\Delta x)^2}{2!}u_i^{(2)} + O\left(\Delta x^3\right) \quad \textbf{(A2-4)}$$

$$bu_{i+1} = bu_i + b\frac{(+1\Delta x)^1}{1!}u_i^{(1)} + b\frac{(+1\Delta x)^2}{2!}u_i^{(2)} + O\left(\Delta x^3\right) \quad \textbf{(A2-5)}$$

Summing the three-point approximation equations gives

$$au_{i-1} - (a+b)u_i + bu_{i+1}$$
$$= \left[(-1)^1 a + (1)^1 b\right]\frac{\Delta x^1}{1!}u_i^{(1)} + \left[(-1)^2 a + (1)^2 b\right]\frac{\Delta x^2}{2!}u_i^{(2)} + O\left(\Delta x^3\right) \quad \textbf{(A2-6)}$$

which can be solved for the first and second derivatives,

$$u_i^{(1)} = \frac{au_{i-1} - (a+b)u_i + bu_{i+1}}{\left[(-1)^1 a + (1)^1 b\right]\frac{\Delta x^1}{1!}} + O(\Delta x^2), \begin{bmatrix}(-1)^1 & (1)^1\\ (-1)^2 & (1)^2\end{bmatrix}\begin{bmatrix}a\\ b\end{bmatrix} = \begin{bmatrix}1\\ 0\end{bmatrix} \quad \textbf{(A2-7)}$$

$$u_i^{(2)} = \frac{au_{i-1} - (a+b)u_i + bu_{i+1}}{\left[(-1)^2 a + (1)^2 b\right]\frac{\Delta x^2}{2!}} + O(\Delta x^1), \begin{bmatrix}(-1)^1 & (1)^1\\ (-1)^2 & (1)^2\end{bmatrix}\begin{bmatrix}a\\ b\end{bmatrix} = \begin{bmatrix}0\\ 1\end{bmatrix}. \quad \textbf{(A2-8)}$$

The matrix equations are chosen such that the unwanted derivatives are eliminated. The end node approximations are calculated using biased formulae. For i=1

$$u_2 = u_1 + \frac{(+1\Delta x)^1}{1!}u_1^{(1)} + \frac{(+1\Delta x)^2}{2!}u_1^{(2)} + O\left(\Delta x^3\right) \quad \textbf{(A2-9)}$$

$$u_3 = u_1 + \frac{(+2\Delta x)^1}{1!}u_1^{(1)} + \frac{(+2\Delta x)^2}{2!}u_1^{(2)} + O\left(\Delta x^3\right) \quad \textbf{(A2-10)}$$

summing

$$-(a+b)u_1 + au_2 + bu_3 =$$
$$\left[a(+1)^1 + b(+2)^1\right]\frac{(\Delta x)^1}{1!}u_1^{(1)} + \left[a(+1)^2 + b(+2)^2\right]\frac{(\Delta x)^2}{2!}u_1^{(2)} + O\left(\Delta x^3\right) \quad \textbf{(A2-11)}$$

which can be solved for both the first and second order approximations as

$$u_1^{(1)} = \frac{-(a+b)u_1 + au_2 + bu_3}{\left[a(+1)^1 + b(+2)^1\right]\frac{(\Delta x)^1}{1!}} + O(\Delta x^2), \begin{bmatrix} (1)^1 & (2)^1 \\ (1)^2 & (2)^2 \end{bmatrix}\begin{bmatrix} a \\ b \end{bmatrix} = \begin{bmatrix} 1 \\ 0 \end{bmatrix} \quad \textbf{(A2-12)}$$

$$u_1^{(2)} = \frac{-(a+b)u_1 + au_2 + bu_3}{\left[a(+1)^2 + b(+2)^2\right]\frac{(\Delta x)^2}{2!}} + O(\Delta x^1), \begin{bmatrix} (1)^1 & (2)^1 \\ (1)^2 & (2)^2 \end{bmatrix}\begin{bmatrix} a \\ b \end{bmatrix} = \begin{bmatrix} 0 \\ 1 \end{bmatrix}. \quad \textbf{(A2-13)}$$

Similarly, the formulae for i=n are

$$u_n^{(1)} = \frac{-(a+b)u_n + au_{n-1} + bu_{n-2}}{\left[a(-1)^1 + b(-2)^1\right]\frac{(\Delta x)^1}{1!}} + O(\Delta x^2), \begin{bmatrix} (-1)^1 & (-2)^1 \\ (-1)^2 & (-2)^2 \end{bmatrix}\begin{bmatrix} a \\ b \end{bmatrix} = \begin{bmatrix} 1 \\ 0 \end{bmatrix} \quad \textbf{(A2-14)}$$

$$u_n^{(2)} = \frac{-(a+b)u_n + au_{n-1} + bu_{n-2}}{\left[a(-1)^2 + b(-2)^2\right]\frac{(\Delta x)^2}{2!}} + O(\Delta x^1), \begin{bmatrix} (-1)^1 & (-2)^1 \\ (-1)^2 & (-2)^2 \end{bmatrix}\begin{bmatrix} a \\ b \end{bmatrix} = \begin{bmatrix} 0 \\ 1 \end{bmatrix}. \quad \textbf{(A2-15)}$$

For a system with three spatial nodes, the operators are

$$D_2^{(1)} = \frac{1}{2\Delta x}\begin{bmatrix} -3 & 4 & -1 \\ -1 & 0 & 1 \\ 1 & -4 & 3 \end{bmatrix} \quad \textbf{(A2-16)}$$

and

$$D_2^{(2)} = \frac{1}{\Delta x^2}\begin{bmatrix} 1 & -2 & 1 \\ 1 & -2 & 1 \\ 1 & -2 & 1 \end{bmatrix}. \quad \textbf{(A2-17)}$$

These operators are both $O(\Delta x^2)$ accuracy. Applying this same technique for a five point stencil results in operators which are $O(\Delta x^4)$ accuracy. These are given as

$$D_4^{(1)} = \frac{1}{12\Delta x}\begin{bmatrix} -25 & 48 & -36 & 16 & -3 \\ -3 & -10 & 18 & -6 & 1 \\ 1 & -8 & 0 & 8 & -1 \\ -1 & 6 & -18 & 10 & 3 \\ 3 & -16 & 36 & -48 & 25 \end{bmatrix} \qquad \textbf{(A2-18)}$$

and

$$D_4^{(2)} = \frac{1}{12\Delta x^2}\begin{bmatrix} 35 & -104 & 114 & -56 & 11 \\ 11 & -20 & 6 & 4 & -1 \\ -1 & 16 & -30 & 16 & -1 \\ -1 & 4 & 6 & -20 & 11 \\ 11 & -56 & 114 & -104 & 35 \end{bmatrix}. \qquad \textbf{(A2-19)}$$

APPENDIX 3 – COMPRESSOR ELECTRO-MECHANICAL MODELING

The compressor piston position, and the resulting PV power due to this motion, can be predicted by measuring the voltage and current waveforms delivered to the compressor. The compressor electrical power input and PV power output are not equivalent due to losses which occur in the compressor. The largest loss is due to resistive power dissipation, which is simple to measure. Some smaller losses are due to eddy currents and friction. These losses require a complete model to allow the prediction of piston motion.

A3.1 The electromechanical system

The compressor model consists of a mechanical model for the piston moving mass which is coupled to an electrical model for the voice coil circuit. The coupling occurs through the electromotive force in the mechanical model and the back emf voltage in the electrical model. Experimental measurement of the voice coil current and voltage in addition to the compression space pressure then allows the piston position to be predicted. Several unknown mechanical and electrical design parameters must be determined before this is possible. The experimental measurement of these design parameters, and the basis for this model are developed by Leach who has modeled a loudspeaker electromechanical system (69).

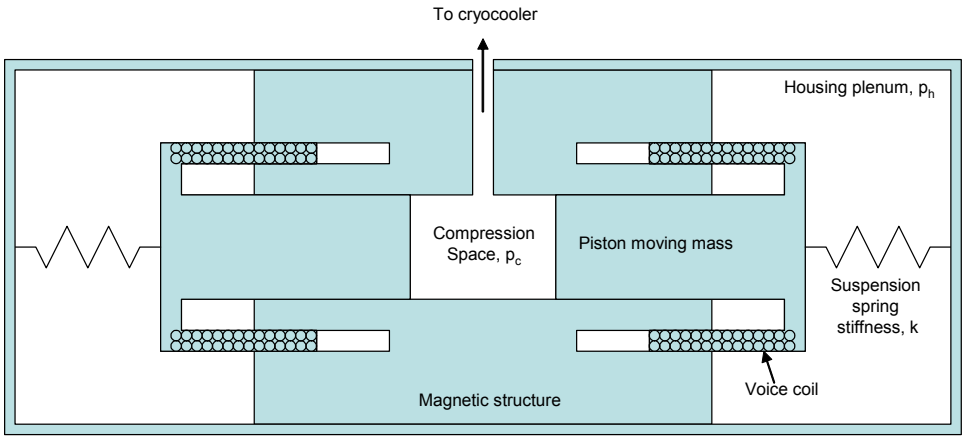

Figure 51 – Voice coil compressor schematic

The compressor schematic illustrated in Figure 51 is representative of the compressors commonly used to drive Oxford class cryocoolers including Stirling and Pulse Tube Cryocoolers. This type of compressor utilizes a "voice-coil" to create an electromotive force to drive the piston motion. The term "voice-coil" comes from audio load speakers which operate very similarly to reciprocating compressors. The compressor is essentially a loudspeaker designed to operate at a very high sound pressure level (SPL). Most compressors use a suspension spring of some sort. Flexures allow the piston to be centered in the cylinder which reduces frictional drag. Other pistons are designed to have a sliding contact seal between the piston and cylinder.

A3.2 The Mechanical System

The compressor model can be constructed by considering a free-body diagram of the compressor piston, similar to Figure 52. In this free-body diagram, the reaction forces due to pressure, friction, electromotive force, spring stiffness, and inertia are

shown. The electromotive force constant, Bl, is the product of the magnetic flux in the air gap, B, and the effective length of wire that cuts the flux, l. It is assumed that Bl is a nonlinear function of the piston position and possibly other parameters such as frequency or current. The pressure in the compression space on the positive x face of the piston is p_c and the pressure in the housing plenum space is p_h. These pressures act on the piston cross sectional area, A_{piston}. The suspension spring stiffness, k, resists the piston movement. In general, k is a function of the piston position. The moving piston experiences a frictional force due to sliding contact between the piston and cylinder or due to viscous shearing of the gas in the piston-cylinder clearance gap in the case of flexure-mounted pistons. In either case, the frictional force can be approximated by the friction coefficient, b, times the velocity of the piston.

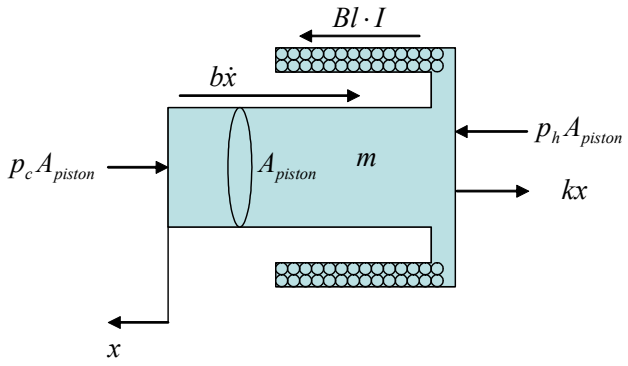

Figure 52 – Compressor piston free-body diagram (FBD)

Considering all of the forces acting on the piston, Newton's Law can be written for the piston moving mass, m, as

$$m\ddot{x} + b\dot{x} + kx = Bl \cdot I + (p_h - p_c)A_{piston} \quad \textbf{(A3-1)}$$

Equation (A4-1) is a differential equation which defines the piston position. This equation can be solved if the pressures, p_h and p_c, and current, I, are known as functions of time. Additionally, the coefficients, m, b, k, Bl, and A_{piston} must be known. The compression space pressure, p_c, can be measured experimentally. The pressure in the housing plenum, p_h, can be modeled using a simple adiabatic compression process for the plenum volume. This results in an expression for the housing pressure as a function of the piston position,

$$p_h = p_b\left(1 - x\frac{A_{piston}}{V_{housing}}\right) \quad \textbf{(A3-2)}$$

where p_b is the mean, or baseline, pressure. When this relation for the housing pressure is substituted into Equation (A4-1), the mechanical equation becomes

$$m\ddot{x} + b\dot{x} + \left(k + \frac{p_b A_{piston}^{\ 2}}{V_{housing}}\right)x = Bl \cdot I - \tilde{p}_c A_{piston} \quad \textbf{(A3-3)}$$

where the compression space pressure has been decomposed into a mean pressure and the fluctuating component,

$$p_c = p_b + \tilde{p}_c \,. \quad \textbf{(A3-4)}$$

The adiabatic assumption for the housing volume pressure reduces the information needed. More accurate modeling of the housing pressure is possible. Heat transfer

between the gas and the housing and piston clearance seal flow will affect the housing pressure. The adiabatic model should be sufficient for a first estimate. The AC component of the compression space pressure, $\tilde{p}_c$, still remains, and this is measured experimentally. At this point, the current can be measured experimentally, and the piston position can be calculated, provided the parameters are known.

A3.3 The Electrical System

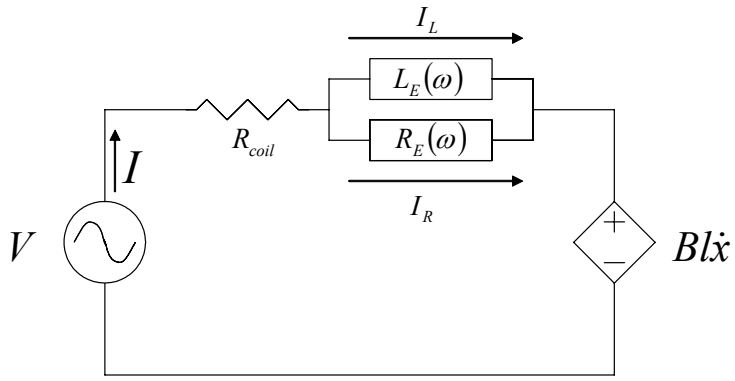

Figure 53 – Leach's lossy inductor voice coil model

The experimentally observed voice-coil current presents large harmonic content with a pure sinusoidal voltage drive. The first and second harmonics are typically 10% of the fundamental. This indicates that there are significant nonlinearities in the electromechanical system. An electrical model can be considered such that the source of the nonlinearities can be studied. This is important for the current objective of determining the piston motion. If the nonlinearity is occurring entirely within the electrical system, then the piston motion is unaffected. However, if the nonlinearity is related to a nonlinear Bl, then the piston motion is affected. Leach (69) has proposed a

possible circuit model for the voice-coil which is illustrated in Figure 53. This circuit is driven by a sinusoidal voltage, V. Current, I, flows through a constant resistance, R_{coil}, which is the coil DC resistance. The current then flows through a parallel circuit representing the lossy inductor created by the voice coil. Losses occur due to eddy currents in the magnetic pole structure. The lossy inductance, L_E, and the eddy current resistance, R_E, are empirically determined and functions of frequency. Leach proposes a method for measuring these two parameters using a small drive voltage at a frequency significantly above the resonance frequency (69). This ensures that there is negligible piston motion. The circuit also contains an additional voltage source, known as the back emf. This voltage source is created by the voice coil traveling through the magnetic field. This voltage is proportional to the electromotive constant, Bl, and the voice coil velocity.

The circuit diagram can be written mathematically as

$$V = I \cdot R_{coil} + \frac{d}{dt}\left(L_E I_L\right) + Bl\dot{x}. \qquad \textbf{(A3-5)}$$

The node current law gives

$$I = I_L + I_R. \qquad \textbf{(A3-6)}$$

The loop voltage law around the parallel inductor and resistor can be written as

$$R_E I_R = \frac{d}{dt}\left(L_E I_L\right). \qquad \textbf{(A3-7)}$$

Finally, the current flowing through the inductor is defined by the nonlinear differential equation

$$\frac{d}{dt}\left(L_E I_L\right) = \left(I - I_L\right)R_E \,. \tag{A3-8}$$

The drive current can now be written as

$$I = \frac{V - Bl\dot{x} + I_L R_E}{R_{coil} + R_E} \tag{A3-9}$$

and the inductor current equation can be written as

$$L_E \frac{dI_L}{dt} - I_L\left(\frac{{R_E}^2}{R_{coil} + R_E} - R_E - \frac{dL_E}{dt}\right) = \frac{R_E}{R_{coil} + R_E}\left(V - Bl\dot{x}\right). \tag{A3-10}$$

The inductor current must be solved for simultaneously with the piston motion which can now be written as

$$m\ddot{x} + \left(b + \frac{Bl^2}{R_{coil} + R_E}\right)\dot{x} + \left(k + \frac{p_b {A_{piston}}^2}{V_{housing}}\right)x = Bl \cdot \frac{V + I_L R_E}{R_{coil} + R_E} - \tilde{p}_c A_{piston} \tag{A3-11}$$

An effective spring stiffness and friction coefficient can be defined as

$$k_{eff} = k + \frac{p_b {A_{piston}}^2}{V_{housing}} \tag{A3-12}$$

and

$$b_{eff} = b + \frac{Bl^2}{R_{coil} + R_E} \tag{A3-13}$$

respectively. It is clear that the housing gas acts as a spring which increases with the square of the piston area. The gas spring stiffness also depends on the baseline pressure and the housing volume as expected. The effective friction coefficient now contains a term which depends on the electromotive force constant squared. This term represents the apparent dissipative force due to coil and eddy current losses.

The compressor electromechanical model can be used for a variety of purposes. First, it can be used as a design tool to predict compressor performance based on a choice of design parameters. Secondly, it can be used to determine unknown parameters based on experimentally measured voltage, current, pressure, and position. In the case of a few unknown parameters, this should be tractable. However, if there are many unknown coefficients, then this presents a difficult problem. For nonlinear parameters, a correlation function needs to be chosen which increases the number of unknown parameters. The model can be tested using a compressor with piston position sensors. In this case, the current, voltage, pressure, and position can be measured. The coil resistance can easily be measured. Using the methodology described by Leach, the lossy inductance and resistance can be measured. From the mechanical design, the piston area and housing volume can be calculated. The suspension stiffness can be relatively easily measured or calculated based on the design. The moving mass can also be measured easily. This leaves the electromotive force constant, Bl , as the remaining unknown.

Once the model parameters have been determined, the compressor piston position, and the resulting PV power due to this motion, can be predicted by measuring the voltage and current waveforms delivered to the compressor and the compression space pressure. This is an attractive development for compressors which are not or cannot be equipped with piston position sensors. The accuracy of the model remains to be determined, but the ability to monitor the compressor piston position without a dedicated sensor which can leak provides significant motivation.

BIBLIOGRAPHY

1. Walker, G. 1983. *Cryocoolers*. Plenum Press, New York and London.

2. Gifford, W. and Longsworth, R. 1965. Pulse tube refrigeration progress. *Advances in Cryogenic Engineering*, Vol. 10, Plenum Press, New York, 69.

3. Longsworth, R. 1967. An experimental investigation of pulse tube refrigeration heat pumping rates. *Advances in Cryogenic Engineering*, Vol. 12, Plenum Press, New York, 608.

4. Mikulin, E., Tarasov, A., and Shkrebyonock, M. 1984. Low-temperature expansion pulse tubes. *Advances in Cryogenic Engineering*, Vol. 29, 629.

5. Olsen, J. and Swift, G. 1997. Acoustic streaming in pulse tube refrigerators: tapered pulse tubes. *Cryogenics*, Vol. 37, No. 12, 769.

6. Radebaugh, R., Lewis, M., Luo, E., Pfotenhauer, M., Nellis, G., and Schunk, L. 2004. Inertance tube optimization for pulse tube refrigerators. *Advances in Cryogenic Engineering*, Vol. 49, submitted for publication.

7. Pecharsky, V., Gschneidner, K., McCallum, R., and Dennis, K. 1997. Influence of alloying on the behavior and properties of Er_3Ni. *Cryocoolers 9*, Plenum Press, New York and London, 663.

8. Gshneidner, K., Pecharsky, V., Osborne, M., Moormen, J., Anderson, I., Pasker, D., and Eastwood, M. 1997. Processing and testing of the low-temperature stage Er_6Ni_2Sn cryogenic regenerator alloy. *Cryocoolers 9*, Plenum Press, New York and London, 669.

9. Bradshaw, T., Orlowska, A., Jewell, C., Jones, B., and Scull, S. 1997. Improvements to the cooling power of a space qualified two-stage Stirling cycle cooler. *Cryocoolers 9*, Plenum Press, New York and London, 79.

10. Takashi, I., Masashi, N., Kouki, N., and Hideto, Y. 1997. Development of a 2W class 4-K Gifford-McMahon cycle cryocooler. *Cryocoolers 9*, Plenum Press, New York and London, 617.

11. Chafe, J., Green, G., and Hendrix, J. 1997. A neodymium plate regenerator for low-temperature Gifford-McMahon refrigerators. *Cryocoolers 9,* Plenum Press, New York and London, 653.

12. Kuehl, H., Schulz S., Walther, C. 1998. Theoretical models and correlations for the flow friction and heat transfer characteristics of random wire regenerator materials. *Proceedings of the 33rd Intersociety Engineering Conference on Energy Conversion,* American Institute of Chemical Engineers, New York, 207.

13. Chafe, J. and Green, G. 1998. Neodymium-ribbon-regenerator cooling performance in a two-stage Gifford-McMahon refrigerator. *Advances In Cryogenic Engineering*, Vol. 43, Plenum Press, New York, 1589.

14. Shull, C., Ravikumar, K., and Frederking, T. 1994. Hydrodynamic characterization of perforated plate flow passages. *Advances In Cryogenic Engineering*, Vol. 39, Plenum Press, New York, 1615.

15. Kays, W. and London, A. 1964. *Compact Heat Exchangers*. McGraw-Hill, Inc. New York.

16. Organ, A. 1992. *Thermodynamics and Gas Dynamics of the Stirling Cycle Machine*. Cambridge University Press, Cambridge 76-78.

17. Jiang, Y., Ju, Y., and Zhou, Y. 1998. A study of oscillating flow characteristics of the regenerators in high frequency pulse tube refrigerators. *Advances In Cryogenic Engineering*, Vol. 43, Plenum Press, New York, 1635.

18. Yuan, Z. and Dybbs, A. 1992. Oscillating flow and heat transfer in a Stirling engine regenerator. *Fundamentals of Heat Transfer in Porous Media*, Vol. 193, ASME, New York, 73.

19. Gedeon, D. and Wood, J. 1997. *Oscillatory-flow regenerator test rig: hardware and theory with derived correlations for screens and felts*. NASA Contractor Report 198442.

20. Helvensteijn, B., Kashani, A., Spivak, A., Roach, P., Lee, J. and Kittel, P. 1998. Pressure drop over regenerators in oscillatory flow. *Advances In Cryogenic Engineering*, Vol. 43, Plenum Press, New York, 1619.

21. Zhao, T. and Cheng, P. 1996. Oscillatory pressure drops through a woven-screen packed column subjected to cyclic flow. *Cryogenics*, Vol. 36, 333.

22. Organ, A. 1997. *The Regenerator and the Stirling Engine*. Mechanical Engineering Publications Limited, London and Bury St Edmunds.

23. Roberts, T. and Desai, P. 2003. Periodic porous media flows in regenerators. *Cryocoolers 12*, Kluwer Academic, New York, 555-561.

24. Watson, E. 1983. Diffusion in oscillatory pipe flow. *Journal of Fluid Mechanics*, Vol. 133, 233-244.

25. Siegel, R. 1987. Influence of oscillation-induced diffusion on heat transfer in a uniformly heated channel. *Transactions of the ASME*, Vol. 109, 244-247.

26. Siegel, R. 1987. Effect of flow oscillations on axial energy transport in a porous media. *Transactions of the ASME*, Vol. 109, 242-244.

27. Kaviany, M. 1990. Performance of a heat exchanger based on enhanced heat diffusion in fluids by oscillation: analysis. *Journal of Heat Transfer*, Vol. 112, 49-55.

28. Kaviany, M. and Reckker, M. 1990. Performance of a heat exchanger based on enhanced heat diffusion in fluids by oscillation: experiment. *Journal of Heat Transfer*, Vol. 112, 56-63.

29. Wu, P. Zhang, L., Qian, L., and Zhang, L. 1994. Numerical modeling of orifice pulse tube by using the method of characteristics. *Advances In Cryogenic Engineering*, Vol. 39, Plenum Press, New York, 1417.

30. Kornhauser, A. and Smith, J. 1989. Heat transfer with oscillating pressure and oscillating flow. *Proceedings of the 24th Intersociety Energy Conversion Engineering Conference IECEC-89*. Vol. 5, 2347.

31. Bauwens, L. 1995. Two-dimensional nearly isothermal pulse-tube and regenerator model. *Proceedings of the 10th Intersociety Cryogenic Symposium*. American Institute of Chemical Engineers, New York, NY, 119.

32. Roach, P., Kashani, A., and Lee, J. 1996. Theoretical analysis of a pulse tube regenerator. *Advances in Cryogenic Engineering,* Vol. 41. Plenum Press, New York, 1357.

33. Kashani, A. and Roach, P. 1998. An optimization program for modeling pulse tube coolers. *Advances in Cryogenic Engineering,* Vol. 43. Plenum Press, New York, 1903.

34. Gary, J. and O'Gallagher, A. 2000. *REGEN3.2 User Manual*, National Institute of Standards and Technology.

35. Lewis, M., Kuriyama, T., Xiao, J., and Radebaugh, R. 1998. Effect of regenerator geometry on pulse tube refrigerator performance. *Advances in Cryogenic Engineering,* Vol. 43. Plenum Press, New York, 1999.

36. Gedeon, D. 1999. *Sage Pulse Tube Model-Class Reference Guide*, Gedeon Associates.

37. Harvey, J., Desai, P., and Kirkconnell, C. 2003. A comparative evaluation of numerical models for cryocooler regenerators. *Cryocoolers 12*, Kluwer Academic, New York, 547-554.

38. Yuan, Z. and Dybbs, A. 1992. High frequency temperature measurement in porous metals. *Fundamentals of Heat Transfer in Porous Media*, Vol. 193, ASME, New York, 67.

39. Rawlins, W. 1992. *The measurement and modeling of regenerator performance in an orifice pulse tube refrigerator*. Ph.D. thesis, University of Colorado, Boulder, CO.

40. Rawlins, W., Radebaugh, R., Bradley, P., and Timmerhaus, C. 1994. Energy flows in an orifice pulse tube refrigerator. *Advances in Cryogenic Engineering,* Vol. 39, Plenum Press, New York, 1449.

41. Hassanizadeh, S. and Gray, W. 1979. General conservation equations for multi-phase systems: 2. Mass, momenta, energy, and entropy equations. *Advances in Water Resources*. Vol. 2, 191.

42. Whitaker, S. 1999. *The method of volume averaging*. Kluwer Academic Publishers. Netherlands.

43. Quintard, M. and Whitaker, S. 1996. Transport in chemically and mechanically heterogeneous porous media. I: Theoretical development of region-averaged equations for slightly compressible flow. *Advances in Water Resources*, Vol. 19, No. 1, 29-47.

44. Gray, W. and O'Neill, K. 1976. On the general equations for flow in porous media and their reduction to Darcy's law. *Water Resources Research*, Vol. 12, No. 2, American Geophysical Union, 148-154.

45. Whitaker, S. 1996. The Forchheimer equation: a theoretical development. *Transport in Porous Media*, Vol. 25, Kluwer Academic Publishers, Netherlands, 27-61.

46. Ochoa-Tapia, J. and Whitaker, S. 1995. Momentum transfer at the boundary between a porous medium and a homogeneous fluid - I. theoretical development. *International Journal of Heat and Mass Transfer*, Vol. 38, No. 14, 2635-2646.

47. Ochoa-Tapia, J. and Whitaker, S. 1995. Momentum transfer at the boundary between a porous medium and a homogeneous fluid - II. comparison with experiment, *International Journal of Heat and Mass Transfer*, Vol. 38, No. 14, 2647-2655.

48. Ochoa-Tapia, J. and Whitaker, S. 1997. Heat transfer at the boundary between a porous medium and a homogeneous fluid. *International Journal of Heat and Mass Transfer*, Vol. 40, No. 11, 2691-2707.

49. Bejan, A. 1997. *Advanced Engineering Thermodynamics, Second Edition*. John Wiley & Sons, Inc, Chapter 11.

50. Schiesser, W. 1991. *The numerical method of lines : integration of partial differential equations*. Academic Press, San Diego.

51. Hicks, J. and Wei, J. 1967. Numerical solution of parabolic partial differential equations with two-point boundary conditions by use of the method of lines. *Journal of the Association for Computing Machinery*, Vol. 14, No. 3, 549-562.

52. Sincovec, R. and Madsen, N. 1975. Software for nonlinear partial differential equations. *ACM Transactions on Mathematical Software*, Vol. 1, No. 3, Association for Computing Machinery, Inc., 232-260.

53. Madsen, N. and Sincovec, R. 1979. ALGORITHM 540 PDECOL, general collocation software for partial differential equations. *ACM Transactions on Mathematical Software*, Vol. 5, No. 3, Association for Computing Machinery, Inc., 326-351.

54. Shampine, L. and Reichelt, M. 1997. The MATLAB ODE Suite. *SIAM Journal on Scientific Computing*, Vol. 18, 1-22.

55. Pareschi, L. 2001. Central differencing based numerical schemes for hyperbolic conservation laws with relaxation terms. *SIAM Journal of Numerical Analysis*, Vol. 39, No. 4, 1395-1417.

56. Naldi, G. and Pareschi, L. 2000. *Numerical schemes for hyperbolic systems of conservation laws with stiff diffusive relaxation*. SIAM Journal of Numerical Analysis, Vol. 37, No. 4, 1246-1270.

57. Morton, K. 2001. Discretization of unsteady hyperbolic conservation laws. *SIAM Journal of Numerical Analysis*, Vol. 39, No. 5, 1556-1597.

58. Roach, R. and Yanping, S. 1998. Unconditional stability, monotonicity and accuracy of the linear exponential interpolation function for the Burgers Equation. *Computers and Fluids*, Vol. 27, No. 8, Elsevier Science, Ltd., 963-983.

59. Weideman, J. and Reddy, S. 2000. A MATLAB differentiation suite. *ACM Transactions on Mathematical Software*, Vol. 26, No. 4, ACM, 465-519.

60. Kirkconnell, C. 1995. *Numerical analysis of the mass flow and thermal behavior in high-frequency pulse tubes*. Ph.D. thesis, Georgia Institute of Technology, Atlanta, GA.

61. Kirkconnell, C., Soloski, S., and Price, K. 1997. Experiments on the effects of pulse tube geometry on PTR performance. *Cryocoolers 9*, Plenum Press, New York and London, 285.

62. Gilmore, D. 1994. *Satellite thermal control handbook*. The Aerospace Corporation Press, El Segundo, CA.

63. Harvey, J. 1999. *Parametric study of cryocooler regenerator performance*. Master's Thesis, Georgia Institute of Technology, Atlanta, GA.

64. Harvey, J., Kirkconnell, C., and Desai, P. 2000. Regenerator performance evaluation in a pulse tube cryocooler. *Advances in Cryogenic Engineering*, Vol. 45, Kluwer Academic, New York and London, 373-382.

65. Hendrix, J. 1996. A new method for producing perforated plate recuperators. *Advances in Cryogenic Engineering*, Vol. 41, Plenum Press, New York, 1329.

66. Knackstedt, M., Sahimi, M., and Chan, D. 1993. Cellular-automata calculation of frequency-dependent permeability of porous media. *Physical Review E*, Vol. 47, No. 4, The American Physical Society, 2593.

67. Whitaker, S. 1967. Diffusion and dispersion in porous media. *AIChE Journal*, VOl. 13, No. 3, 420.

68. Whitaker, S. 1973. The transport equations for multi-phase systems. *Chemical Engineering Science*, Vol. 28, 139.

69. Leach, M. 2002. Loudspeaker voice-coil inductance losses: circuit models, parameter estimation, and effect on frequency response. *Journal of the Audio Engineering Society*, Vol. 50, No. 6, 442.